

PROGRESSIVE DAMAGE TO A SHIP'S
STRUCTURE DUE TO ICE LOADING

BRUCE W.T. QUINTON



PROGRESSIVE DAMAGE TO A SHIP'S

STRUCTURE DUE TO ICE LOADING

by

© Bruce W. T. Quinton, B. Eng.

A thesis submitted to the School of Graduate Studies
in partial fulfilment of the requirements for the degree of
Master of Engineering

Faculty of Engineering and Applied Science
Memorial University of Newfoundland

January 2008

St. John's

Newfoundland

Canada

Abstract

This thesis investigates the structural response of an “IACS polar class” large grillage structure to progressive damage loads from ice. The “IACS polar class” design scenario is a static “glancing” load. It was desired to know if the structure responded differently to dynamic progressive loads, than it did to static loads. An explicit nonlinear numerical model was created. This numerical model was validated against full-scale experiments involving an “IACS polar class” large grillage structure. Eight progressive damage load scenarios were tested using the numerical model. In addition, strategically placed static loads were tested in order to provide a basis for comparison between the dynamic and static structural responses. It was found that the large grillage’s structural capacity to withstand dynamic progressive damage loads was generally less than its capacity to withstand static loads. Further, the structural mechanisms behind this decrease in structural capacity were identified.

Acknowledgments

This research was made possible only through the help and support of a few great people and organizations. I would like to express my sincerest thanks and appreciation to the following:

Dr. Claude Daley, Professor – my graduate supervisor, for his excellent direction, financial support, enthusiasm, and confidence – without it I would not be as fortunate as I am today.

Dr. Robert Gagnon, Senior Researcher at NRC-IOT – my thesis co-supervisor, for his extensive expertise and for providing access to the IOT *Beowulf Cluster*; without which the numerical model presented herein (and hence this research) would be virtually impossible.

Mr. Andrew Kendrick and Mr. Gareth Igloliorte of BMT Fleet Technology Ltd., for their outstanding help and support.

Mr. Gilbert Wong, Computer System Administrator at NRC-IOT, for his remarkable help, knowledge, and patience concerning my use of the *Beowulf Cluster*.

Ms. Trish Leblanc and Ms. Jennifer Mersereau of NRC-CISTI, for their wonderful help and patience.

Mr. Matt Curtis and Mr. Steve Steele, technologists at MUN, for their wonderful help and expertise during the physical experiments.

The National Sciences and Engineering Research Council of Canada (NSERC), for their financial support through their IPS 1 program.

BMT Fleet Technology Ltd., for their financial support through their BOSARP program, and for providing office space and resources throughout my research.

Institute for Ocean Technology (NRC-IOT), for their provision of office space, resources, and access to their laboratory facilities.

National Research Council of Canada (NRC), for their financial support through their GSSSP program.

I would also like to acknowledge Jacob Abraham, a fellow graduate student who was a great friend and colleague during my research.

Lastly, I would like to thank my wife, Melissa, for her unending patience and support. This thesis is dedicated to you.

Table of Contents

Abstract	ii
Acknowledgments.....	iii
Table of Contents.....	iv
List of Tables	ix
List of Figures	x
Nomenclature and Abbreviations	xviii
1 Introduction.....	1
1.1 Scope and Objectives	2
1.2 Literature Review.....	5
1.3 Overview of Ice Classes for various Classification Societies	6
1.3.1 History of ice classifications	6
1.3.2 Unified polar rules	7
1.4 Progressive Damage Physics.....	9
1.4.1 Comparison with grounding/raking incidents.....	11
1.4.2 Collision physics	12
1.4.3 Methods for analysis/prediction of internal mechanics	13
1.5 Steel Grillage Load-Displacement Behaviour.....	14
1.6 The Finite Element Method.....	16
1.6.1 Classes of finite element codes	16
1.6.2 Finite elements	18
1.6.3 LSTC – explicit nonlinear finite element codes	22

2 Large Grillage Experiments	27
2.1 Introduction	27
2.2 Large Grillage Model	28
2.3 Boundary Conditions.....	31
2.4 Instrumentation.....	32
2.5 Loading Scenario.....	32
2.6 Experimental Procedure	34
2.7 Results	35
2.7.1 Load patch 1	36
2.7.2 Load patch 2.....	37
2.7.3 Load patch 3.....	38
2.8 Material Tensile Tests	40
2.8.1 Test specimen specifications.....	41
2.8.2 Instrumentation and apparatus	42
2.8.3 Results.....	43
3 Numerical Model	51
3.2 Geometric Structural Model.....	52
3.3 The Finite Element Mesh	56
3.3.1 Element choices	56
3.3.2 Element formulations.....	59
3.3.3 Other shell parameters	60
3.3.4 Meshing.....	62
3.3.5 Model decomposition.....	62

3.3.6	Mesh Conversion Study	63
3.4	Material Model	71
3.4.1	Mat_24	72
3.4.2	Mat_20	73
3.4.3	Utilizing uniaxial tensile test data in numerical models	74
3.4.4	Material Instability	76
3.4.5	Stress-strain curve definition	77
3.4.6	Material model for each component	79
3.4.7	Final material models.....	81
3.5	Boundary Conditions.....	81
3.6	Part Definition	83
3.7	Contact	84
3.7.1	Penalty method.....	85
3.7.2	Shell element thickness.....	86
3.8	Loading.....	87
3.9	Damping	87
3.10	Solution Controls.....	88
3.11	Results Declaration	89
3.12	Modifications from Trial-and-Error	90
3.12.1	Hourgassing	90
3.13	Model Validation	91
3.13.1	Load	91
3.13.2	Results.....	92

3.14	Numerical Model Summary	94
3.14.1	Finite element mesh	94
3.14.2	Material model	94
3.14.3	Boundary conditions	95
3.14.4	Part definition.....	95
3.14.5	Contact definition.....	95
3.14.6	Load definition.....	96
3.14.7	Damping definition	96
3.14.8	Solution control parameters	96
3.14.9	Results declaration	96
4	Progressive Damage Tests and Results.....	98
4.1	Notes on Loading, Analysis, and Results.....	98
4.2	Progressive Damage between Transverse Frames	103
4.2.1	Load scenario 1: progressive damage between longitudinals.....	103
4.2.2	Load scenario 2: progressive damage along a longitudinal	122
4.2.3	Load scenario 3: progressive damage diagonally across longitudinals	139
4.3	Progressive Damage across Transverses	149
4.3.1	Load scenario 4: progressive damage between longitudinals and across transverses	149
4.3.2	Load scenario 5: progressive damage along the central longitudinal and across transverses	159
4.3.3	Load scenario 6: progressive damage diagonally across longitudinals and transverses	166

4.4	Progressive Damage Parallel with Transverses	172
4.4.1	Load scenario 7: progressive damage between transverse stiffeners.....	172
4.4.2	Load scenario 8: progressive damage along a transverse stiffener	176
4.5	Summary of Progressive Damage Load Scenario Results	182
5	Conclusions and Recommendations	189
5.1	Conclusions	189
5.2	Recommendations	190
6	References.....	193
	Appendix A: Beowulf Cluster Specifications	199
	Appendix B: Large Grillage Data Collection Equipment and Specifications	200
	Appendix C: Material Instability Test	203

List of Tables

Table 1-1: IACS Polar Class Descriptions (IACS 2007 P. II-2).....	9
Table 2-1: Material properties for uniaxial tensile test specimen 1.....	45
Table 2-2: Material properties for uniaxial tensile test specimen 2.....	46
Table 2-3: Material properties for uniaxial tensile test specimen 3.....	47
Table 2-4: Material properties for uniaxial tensile test specimen 4.....	48
Table 2-5: Material properties for uniaxial tensile test specimen 5.....	50
Table 2-6: Summary of material properties for the uniaxial tensile test specimens.....	50
Table 3-1: Gaussian quadrature through-thickness integration point coordinates.....	61
Table 3-2: Mesh details for mesh conversion study.....	64
Table 3-3: Material model (Paik's Method) parameters for five components.....	80
Table 3-4: Large Grillage material model parameters.....	81
Table 3-5: Large Grillage material model parameters.....	94
Table 4-1: Progressive damage load scenarios.....	101
Table 4-2: Structural capacities for load scenario 5.....	165
Table 4-3: Structural capacities for load scenario 6.....	171
Table 4-4: Structural capacities for load scenario 7.....	176
Table 4-5: Structural capacities for load scenario 8.....	181
Table 4-6: Dynamic decrease in structural capacity results.....	183

List of Figures

Figure 1-1: Map of IMO definition of “arctic ice-covered waters” (IMO 2002).	8
Figure 1-2: Load-displacement curve for a steel stiffened panel.....	15
Figure 1-3: Load-displacement curve for a steel uniaxial tensile test specimen.	15
Figure 1-4: Illustration of buckled and folded stiffeners and hull plating.	21
Figure 1-5: Hourgassing in a finite element mesh.	22
Figure 2-1: Large grillage model – isometric view.....	29
Figure 2-2: Large grillage model primary and secondary stiffening arrangement.	29
Figure 2-3: Large grillage end boundary condition.	31
Figure 2-4: Large grillage model – top view with load patches.	33
Figure 2-5: 500 kip Enerpac® industrial grade hydraulic ram.	34
Figure 2-6: Large grillage experimental setup.....	35
Figure 2-7: Load-displacement plot for loads applied to the three load patches.	36
Figure 2-8: Fractured hull plating for load patch 2.....	38
Figure 2-9: Photos showing approximate point of buckling for load patch 3.	39
Figure 2-10: Preliminary numerical model - effective (von Mises) residual stress.....	41
Figure 2-11: Tensile test specimen dimensions.	41
Figure 2-12: Tensile test specimens.....	42
Figure 2-13: Instron 5585 H.	43
Figure 2-14: Stress-strain plot for uniaxial tensile test specimen 1.	44
Figure 2-15: Stress-strain plot for uniaxial tensile test specimen 2.	46
Figure 2-16: Stress-strain plot for uniaxial tensile test specimen 3.	47

Figure 2-17: Stress-strain plot for uniaxial tensile test specimen 4	48
Figure 2-18: Stress-strain plot for uniaxial tensile test specimen 5.....	49
Figure 3-1: Large grillage geometric model showing lines.....	54
Figure 3-2: Large grillage geometric model showing areas.....	54
Figure 3-3: Plot of shell element normals for large grillage numerical model.....	55
Figure 3-4: Shell element geometry (ANSYS Inc. 2007a).....	57
Figure 3-5: Solid element geometry (ANSYS Inc. 2007a).....	58
Figure 3-6: Plot of decomposed sections of a numerical model using the RCB method.	63
Figure 3-7: Mesh conversion study – mesh 1.....	65
Figure 3-8: Mesh conversion study – mesh 2.....	66
Figure 3-9: Mesh conversion study – mesh 3.....	66
Figure 3-10: Mesh conversion study – mesh 4.....	67
Figure 3-11: Mesh conversion study – comparison of Mesh 1 and Mesh 2 results.....	68
Figure 3-12: Mesh conversion study – comparison of Mesh 1 and Mesh 3 results.....	69
Figure 3-13: Mesh conversion study – comparison of Mesh 1 and Mesh 4 results.....	69
Figure 3-14: Mesh conversion study – comparison of Mesh 2 and Mesh 3 results.....	70
Figure 3-15: Mesh conversion study – comparison of Mesh 2 and Mesh 4 results.....	70
Figure 3-16: Bilinear stress-strain curve.....	73
Figure 3-17: 27 point stress-strain curve with strain softening.....	77
Figure 3-18: Stress-strain curves of varying complexity.....	78
Figure 3-19: Load-displacement curve results for various material model inputs.	79
Figure 3-20: Load-displacement curve results for multiple and single material models..	80
Figure 3-21: Fixed nodes (shown in black) used to model bolted boundary conditions. .	82

Figure 3-22: Large grillage model “parts”.....	83
Figure 3-23: Rigid indenter “part”.....	84
Figure 3-24: Plot of deformed structure overlaid with von Mises stress fringe plot.	90
Figure 3-25: Refinement of central longitudinal stiffener flange.	91
Figure 3-26: Comparison of experimental and numerical model results.....	93
Figure 4-1: Example load history curve showing static (green “S”) and dynamic (red “D”) loads.	100
Figure 4-2: Load scenario 1: progressive damage between longitudinals and transverses.	
.....	104
Figure 4-3: Load scenario 1: load-displacement curves for 0.2 and 0.5 cm load cases.	105
Figure 4-4: Load scenario 1: Residual plastic strain for 0.2 cm load case.	106
Figure 4-5: Load scenario 1: Residual plastic strain for 0.5 cm load case.	107
Figure 4-6: Load scenario 1: load-displacement curves for all five load cases.	108
Figure 4-7: Load scenario 1: z-force time-history plot for all load cases.	110
Figure 4-8: Load scenario 1: residual plastic strain for load case 1: 2 cm indentation.	112
Figure 4-9: Load scenario 1: residual plastic strain for load case 1: 5 cm indentation.	112
Figure 4-10: Load scenario 1: residual plastic strain for load case 1: 10 cm indentation.	
.....	113
Figure 4-11: Load scenario 1: static load z-displacement (indenter not shown): 2 cm load case.....	114
Figure 4-12: Load scenario 1: static load M_{xy} moment distribution: 2 cm load case...114	
Figure 4-13: Load scenario 1: static load in-plane maximum stress (indenter shown, transverses not shown): 2 cm load case.....	115

Figure 4-14: Load scenario 1: dynamic load z-deformation: 2 cm load case.....	116
Figure 4-15: Load scenario 1: dynamic load M_{xy} bending moment distribution: 2 cm load case.....	117
Figure 4-16: Load scenario 1: M_{xy} plot for static (top) and dynamic (bottom) loads: 0.2 cm load case.....	118
Figure 4-17: Load scenario 1: dynamic load in-plane maximum stress distribution: 2 cm load case.....	119
Figure 4-18: N_{xy} plot with highest maximum in-plane stressed elements outlined in pink.	120
Figure 4-19: Load scenario 1: Q_x through-plane shear force for static load (top) and dynamic load (bottom): 2 cm load case.....	121
Figure 4-20: Load scenario 1: Q_y through-plane shear force for static load (top) and dynamic load (bottom): 2 cm load case.....	121
Figure 4-21: Load scenario 2: progressive damage along longitudinal and between transverses.....	122
Figure 4-22: Load scenario 2: load-displacement curves for 0.2 and 0.5 cm load cases.	123
Figure 4-23: Load scenario 2: dynamic load M_{xy} plot for load scenarios 1 (top) and 2 (bottom): 0.2 cm load case.....	124
Figure 4-24: Load scenario 2: plastic strain for load case 0.2 cm.	125
Figure 4-25: Load scenario 2: rigid body z-displacement of the longitudinal stiffener web: 0.2 cm load case.....	126
Figure 4-26: Static load capacity curve for location 2.....	127

Figure 4-27: Static load capacity curve for location 3.....	128
Figure 4-28: Load scenario 2: plastic strain for the 0.5cm load case.	129
Figure 4-29: Load scenario 2: dynamic load M_{xy} plot for the 0.5 cm load case.....	129
Figure 4-30: Load scenario 2: load-displacement curves for all load cases.	130
Figure 4-31: y-displacement plot for 10 cm static load at location 3.	132
Figure 4-32: Load scenario 2: initial central stiffener buckling (top), M_{xy} moment (mid), and max in-plane stress (bottom): 2 cm load case.....	134
Figure 4-33: Load scenario 2: subsequent central stiffener buckling (top), M_{xy} moment (mid), and max in-plane stress (bottom): 2 cm load case.	135
Figure 4-34: Load scenario 2: initial central stiffener buckling (top), M_{xy} moment (mid), and max in-plane stress (bottom): 5 cm load case.....	137
Figure 4-35: Load scenario 2: subsequent central stiffener buckling (top), M_{xy} moment (mid), and max in-plane stress (bottom): 5 cm load case.	138
Figure 4-36: Load scenario 3: progressive damage across longitudinals and between transverses.....	139
Figure 4-37: Load scenario 3: load-displacement curves for 0.2 and 0.5 cm load cases.	140
Figure 4-38: Load scenario 3: load-displacement curves for 0.2 to 5 cm load cases. ...	142
Figure 4-39: Load scenario 3: maximum in-plane stresses: 2 cm load case.....	145
Figure 4-40: Load scenario 3: indenter lateral motion and effective width (plate not shown).....	146
Figure 4-41: Load scenario 3: M_{xy} bending moment distribution: 2 cm load case.....	147
Figure 4-42: Load scenario 3: residual y-direction displacements: 2 cm load case.	148

Figure 4-43: Load scenario 4: progressive damage between longitudinals and across transverses.....	150
Figure 4-44: Load scenario 4: collision between the indenter and the transverse stiffener: 5 cm load case.....	151
Figure 4-45: Load scenario 4: load-displacement curves for 0.2 and 0.5 cm load cases.	152
Figure 4-46: Load scenario 4: load-displacement curves for 0.2 and 0.5 cm load cases (zoomed).....	152
Figure 4-47: Load scenario 4: plastic damage at first transverse frame encounter: 0.2 (top) and 0.5 cm (bottom) load cases.....	153
Figure 4-48: Location 6 static structural capacity curve.....	156
Figure 4-49: Load scenario 4: load-displacement curve: 2 cm load case.	157
Figure 4-50: Load Scenario 4: transverse frame buckling (dynamic loading): 2 cm load case.	158
Figure 4-51: Static loading of transverse stiffener at “between longitudinals” location: z-displacement fringes shown.....	158
Figure 4-52: Load scenario 5: progressive damage along central longitudinal and across transverses.....	159
Figure 4-53: Load scenario 5: load-displacement curves for 0.2, 0.5, and 2 cm load cases.....	160
Figure 4-54: Load scenario 5: load-displacement curves for 0.2, 0.5, and 2 cm load cases (zoomed).	161
Figure 4-55: Load scenario 5: plastic damage extent for static load: 2 cm load case...163	

Figure 4-56: Load scenario 5: longitudinal stiffener buckling extent before transverse frame encounter: 2 cm load case.....	163
Figure 4-57: Load scenario 5: wireframe plot of cut-out and indenter-transverse frame interaction: 2 cm load case.....	164
Figure 4-58: Location 8 static structural capacity curve.....	166
Figure 4-59: Load scenario 6: progressive damage diagonally across longitudinals and transverses.....	167
Figure 4-60: Load scenario 6: load-displacement curves for 0.2, 0.5, and 2 cm load cases.....	168
Figure 4-61: Load scenario 6: wireframe plot of cut-out and 1 st indenter-transverse frame interaction: 2 cm load case.....	169
Figure 4-62: Load scenario 6: wireframe plot of cut-out and 2 nd indenter-transverse frame interaction: 2 cm load case.....	171
Figure 4-63: Load scenario 7: progressive damage between transverse stiffeners.....	173
Figure 4-64: Load scenario 7: load-displacement curves for 0.2, 0.5, and 2 cm load cases.....	174
Figure 4-65: Load scenario 8: progressive damage along a transverse stiffener.....	177
Figure 4-66: Load scenario 8: wireframe plot of indenter-cut-out collision: 5 cm load case.....	177
Figure 4-67: Load scenario 8: load-displacement curves for 0.2, 0.5, and 2 cm load cases.....	178
Figure 4-68: Load scenario 8: extent of plastic damage for the 0.2 cm load case.....	179

Figure 4-69: Load scenario 8: plot of normal force reaction to static load (top) and dynamic load (bottom).....	181
Figure C-0-1: Unstable Material Model.	203
Figure C-0-2: Mesh showing loaded shell element.	204
Figure C-0-3: Near centre nodal displacement plot.	204
Figure C-0-4: Shell rebound deformation just before infinite expansion.	205

Nomenclature and Abbreviations

1D	One dimensional
2D	Two dimensional
3D	Three dimensional
ABS	American Bureau of Shipping classification society
ASPPR	Arctic Shipping Pollution Prevention Regulations
Beowulf cluster	A class of <i>computer clusters</i> utilizing personal computers
CAC	Canadian arctic class
Computer cluster	A collection of networked computers that act like a single computer
DOF	Degree of freedom
DNV	Det Norske Veritas classification society
Dyna	Refers to either LS-Dyna or MPP-Dyna interchangeably
FE	Finite element
FEM	Finite element model
GL	Germanischer Lloyd classification society
IACS	International Association of Classification Societies
IMO	International Maritime Organization
Head node	The node that controls all others on the <i>computer cluster</i>
LSTC	Livermore Software Technology Corporation
LR	Lloyds Register classification society
Microscribe	A 3D digitizing device used to capture the geometric properties of a real object in 3D space

NIPS	Number of through-thickness integration points input for shell element formulations
Node	A basic <i>finite element</i> or a slave computer on the <i>computer cluster</i>
Parts	Collections of elements in <i>Dyna</i> having identical assigned properties
Run time	Length of time required for the solver to run the numerical model
SHRF	Shear factor input for shell element formulations
Simulation time	Length of time explicitly simulated within the numerical model
Yoyo-pot	A linear potentiometer that uses a spring loaded spool of twine as its actuator

1 INTRODUCTION

The Arctic is believed to hold vast quantities of the world's undiscovered natural resources. The polar ice cap is melting (Dixon 2007), suggesting that exploitation of these resources will become viable in the near future. The summer of 2007 in particular showed the largest decrease in Arctic ice in recorded history (European Space Agency 2007; Revkin 2007), prompting expectations that the "Canadian Internal Waters" (formerly known as the "Northwest Passage") may soon become a viable summer shipping route.

This increase in Arctic activity will require far more ice-strengthened ships than are currently available worldwide. It will also require innovations in policy making, vessel management, and ship design. One of the main difficulties associated with shipping in ice-infested waters is the decrease in transit speed required to avoid hull damage from impacts with ice. A fleet of arctic-going ships would necessarily be much larger than an equivalent fleet of standard ships in order to transport the same amount of cargo in the same amount of time. It is apparent then, that an optimization between vessel transit speed through ice and structural design against repeated ice impacts is necessary to increase the overall efficiency of future arctic going vessels. To address these concerns, ship classification societies are moving away from traditional yield-stress limit state designs and have begun to consider ultimate (i.e. plastic) limit states (Hughes 1988; Paik and Thayamballi 2003) for their ship structural design rules. An example of this trend is the new unified polar class rules (IACS 2007). These rules require that ship structures be

optimized for plastic failure rather than elastic failure, resulting in a lighter and often-stronger ship design. However, the plastic behaviour of ship structures is still not fully understood. Questions remain concerning the capacity of ships to withstand progressive damage from ice loads.

This thesis is divided into five main chapters. This, the introductory chapter, defines the scope and objectives of this thesis; describes the literature review for this thesis; outlines the classification of ice-strengthened ships; discusses progressive damage; and presents the finite element code employed in this research. Chapter 2 outlines the large grillage structural experiments that were used to validate the numerical model developed in Chapter 3. Chapter 3 outlines the progressive damage numerical model and its validation. Chapter 4 discusses the progressive damage loading scenarios applied to the numerical model and presents their results. Chapter 5 presents the conclusions of this thesis and recommendations for further research.

1.1 Scope and Objectives

Briefly, progressive damage from ice is damage that occurs to a ship's structure during and after an impact with ice; and can be viewed as plastic structural damage due to the impact and subsequent scoring/raking action of ice as it scrapes along the hull.

This thesis investigates the structural capacity of an “IACS polar class” ship structure regarding its response to large plastic deformations resulting from progressive damage

from ice loading. The IACS polar rules design scenario is a *glancing* collision of the ship structure with an ice edge (IACS 2007). Further, this glancing load is applied statically¹ to the ship's structure. It is therefore of interest to determine the reaction of an IACS classed ship's structure to progressive damage from ice – which is a “continual” ice load rather than a glancing collision. This is done through the creation of an explicit nonlinear numerical model that is validated against full-scale experiments involving a large steel grillage structure that has been designed to satisfy the “IACS polar class” rules. After validation, eight progressive damage scenarios were imposed on the numerical model. These eight load scenarios attempt to address questions that may arise during ice-strengthened ship design scenarios; namely: Is this structure capable of withstanding progressive damage due to an ice load? What are the structural failure mechanisms associated with progressive damage from ice? What are the design loads associated with progressive damage from ice?

The eight progressive damage scenarios investigated may be divided into three categories: progressive damage between two transverse frames, progressive damage spanning two transverse frames, and progressive damage parallel to the transverse frames.

The progressive damage scenarios broken down by category are:

- Category 1: Progressive damage between transverse frames:
 1. progressive damage along the central longitudinal stiffener,
 2. progressive damage between longitudinal stiffeners, and
 3. progressive damage diagonally crossing several longitudinal stiffeners.

¹ I.e. the load is not moving, and does not account for relative motion between the ship and the ice.

- Category 2: Progressive damage across transverse frames:
 4. progressive damage along the central longitudinal stiffener and across two transverse frames,
 5. progressive damage between longitudinal stiffeners and across two transverse frames, and
 6. progressive damage diagonally crossing several longitudinal stiffeners and two transverse frames.
- Category 3: Progressive damage parallel with transverse frames:
 7. progressive damage across several longitudinal stiffeners, and
 8. progressive damage along a transverse frame.

While progressive damage scenarios are inherently dynamic (i.e. they are largely affected by phenomena that depend on time), these eight progressive damage scenarios were modeled without material strain-rate effects, velocity dependent friction, or rigid body ship motions. It was not possible to validate the numerical model against these time-dependent effects at this time.

The results of these progressive damage loading scenarios are presented in the form of structural reaction force curves, structural failure mechanisms, and effect on structural capacity.

In short, the objectives of this thesis are: to create a numerical model capable of predicting localized progressive damage to a ship's structure; to validate the numerical model against results of physical experiments on a full scale IACS ship structure; to

investigate the structural capacity of an “IACS polar class” ship structure to progressive damage from ice loads using the numerical model; to identify the local structural failure mechanisms associated with progressive damage from ice; and to provide a basis for the numerical modeling of future large scale experiments where arctic ice will be dropped on ship structures.

1.2 Literature Review

Much literature was reviewed in preparation for, and throughout this research. However, the author was not able to find any publicly available literature pertaining directly to progressive damage to a ship’s structure from ice loading. The National Research Council’s CISTI library, Transport Canada’s library, and Memorial University of Newfoundland’s library were all searched. Further, an extensive internet search was conducted that included several online journal and book publishers including Elsevier², SpringerLink³, IngentaConnect⁴, ScienceDirect⁵, and Wiley InterScience⁶. Therefore, literature pertaining to the design of ship structures, collision/grounding research, finite element structural modeling, and classification society rules was reviewed and adapted as required. Relevant literature from this review is cited and summarized throughout this thesis where appropriate, including the state-of-the-art for finite element simulation of collisions with ship structures.

² http://www.elsevier.com/wps/find/homepage.cws_home

³ <http://www.springerlink.com/home/main.mpx>

⁴ <http://www.ingentaconnect.com/>

⁵ <http://www.sciencedirect.com/>

⁶ <http://www3.interscience.wiley.com/aboutus/journals.html>

1.3 Overview of Ice Classes for various Classification Societies

Ice classifications of ships are offered by many of the various classification societies: Lloyds Register (LR), Germanischer Lloyd (GL), American Bureau of Shipping (ABS), and Det Norske Veritas (DNV), to name a few. Ice classifications of ships are generally be broken into two main divisions: icebreaking vessels and ice-strengthened vessels. Icebreaking ships have greater hull strengthening than ice-strengthened ships, and are used primarily as support ships. Icebreakers (depending on their ice class) are capable of managing and manoeuvring in up to all types of ice regimes⁷. Ice-strengthened ships are generally shipping vessels (e.g. tankers, supply ships, cargo ships, etc...) whose hulls have been strengthened for possible contact with ice. Various levels of ice-class may be assigned to ice-strengthened ships, allowing them to operate in ice regimes of various ice thickness and concentration; but their capabilities for breaking ice, managing ice, or manoeuvring in difficult ice conditions (e.g. multi-year ice) are highly limited or non-existent. This thesis is primarily concerned with ice-strengthened shipping vessels, as these types of vessels would be those classed by the new IACS unified polar rules.

1.3.1 History of ice classifications

Ice classifications are a result of laws enacted by various countries to protect their arctic waters and interests. Canada, Russia, Finland, and Sweden are a notable few of these

⁷ An ice regime is composed of any mix or combination of ice types, including open water. An ice regime occurs as a region in navigable waters covered with generally consistent ice conditions; i.e. the distribution of ice types and concentrations does not change very much from point to point in this region. Definition taken from Transport Canada (Transport Canada 1998).

countries. Each of these countries has developed its own rules and regulations concerning the strengthening of ships for transit through its arctic waters. They are the:

- Canadian ASPPR/CAC Classes,
- Russian LU Classes, and the
- Finnish/Swedish “Baltic” Classes.

Of these, Finland and Sweden have developed a set of rules called the “Finnish-Swedish Ice Class Rules” (FMA-SMA 2008) which apply to shipping vessels entering the Baltic Sea. Ice classifications based on these rules are typically referred to as “Baltic classes”. The Finnish-Swedish ice class rules also form the basis for equivalent ice classifications granted by most of the major ship classification societies (e.g. ABS, LR and DNV) for arctic shipping vessels (rather than icebreakers).

1.3.2 Unified polar rules

The IACS unified polar rules (IACS 2007) were created by an international committee composed of both IACS members and non-members in response to a global interest in “harmonising” existing safety and pollution standards for marine operations in polar waters (IACS 2006). These rules are intended to be used in conjunction with the International Maritime Organization’s (IMO) “Guidelines for ships operating in arctic ice-covered waters” (IMO 2002). The IMO document provides a framework for the design and operation of ice-strengthened ships and the IACS document provides specific structural and machinery requirements. These documents apply primarily to ships

operating in the “arctic ice-covered waters” explicitly defined in the IMO guidelines. A map of the geographical part of the definition is shown in Figure 1-1.

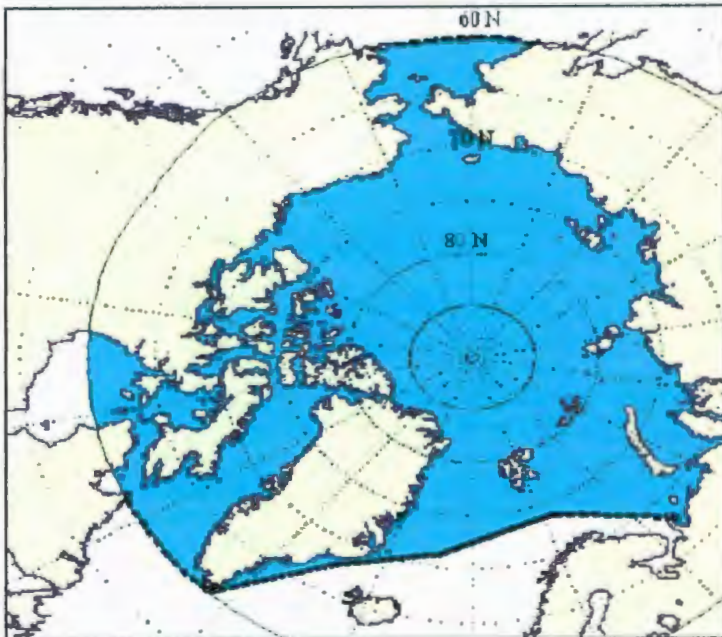


Figure 1-1: Map of IMO definition of “arctic ice-covered waters” (IMO 2002).

The IACS polar rules are based on rational ship design. The design scenario for determining the scantlings required to resist ice loads is a glancing collision between the structure and an ice edge. An ice edge may be the edge of an ice-channel or the edge of an ice floe. This glancing collision may occur at the bow, mid, or aft of the ship in both assisted and unassisted operation. The design ice load is characterized by an average pressure (P_{avg}) uniformly distributed over a rectangular load patch of height (b) and width (w). This design load is applied statically and therefore does not account for the

possible dynamic load effects. A complete derivation of the design scenario and load may be found in Daley (2001).

The two lowest IACS polar classes, “PC-6” and “PC-7”, are nominally equivalent to the two highest Baltic classes, “1A Super” and “1A”, respectively (IMO 2002). Descriptions of all seven IACS polar classes are given in Table 1-1.

Table 1-1: IACS Polar Class Descriptions (IACS 2007).

Polar Class	Ice Description (based on WMO Sea Ice Nomenclature)
PC 1	Year-round operation in all polar waters
PC 2	Year-round operation in moderate multi-year ice conditions
PC 3	Year-round operation in second-year ice which may include multi-year ice inclusions
PC 4	Year-round operation in thick first-year ice which may include old ice inclusions
PC 5	Year-round operation in medium first-year ice which may include old ice inclusions
PC 6	Summer/autumn operation in medium first-year ice which may include old ice inclusions
PC 7	Summer/autumn operation in thin first-year ice which may include old ice inclusions

1.4 Progressive Damage Physics

Progressive damage occurs after the initial ice impact and can be viewed as plastic structural damage due to the scoring/raking action of ice as it scrapes along the hull. This type of structural interaction can happen at the waterline or below. Waterline damage may result from collision with pack ice, glacial ice of various size (from growler to

iceberg), or level-ice during ice-channel navigation (assisted or unassisted). Damage below the waterline may occur from collision with glacial ice, or if a ship strikes a submerged ice ridge (e.g. *anchor ice*⁸).

Progressive damage is similar to *raking damage*⁹; however, the tearing and subsequent curling of the hull steel (see (Zhang 2002)) is not treated because ice-strengthened ships are expected to survive such impacts (within their operational capacity) without tearing of the hull plating. Progressive damage occurs when the relative speed between ship and ice is large enough to extend the damage past the point of collision; provided that the geometry of the impacted area allows for the sliding of the ice along the hull.

As noted above, publicly available literature specifically dealing with progressive damage to ship structures from ice could not be found. There is, however, much research on the related topics of ship grounding and raking damage from submerged rocks. This literature was reviewed and the methods applied therein were adapted to this research. The cited literature focuses on the physics of ship collisions and grounding incidents and the methods used to research these events using finite element numerical models.

⁸ *Anchor ice* is defined as "submerged ice attached or anchored to the bottom, irrespective of the nature of its formation" (WMO/IOC 2004).

⁹ *Raking damage* is commonly understood to refer to the damage resulting from a grounding incident when a ship traveling at a non-trivial speed strikes a rock, resulting in damage in the form of torn and curled hull steel.

1.4.1 Comparison with grounding/raking incidents

Much research has been done to predict the outcome of ship collisions/groundings; particularly regarding oil tankers and oil outflow since the Exxon Valdez oil spill in Alaska in March 23, 1989 resulting in the U.S. Oil Pollution Act (1990) and the subsequent International Maritime Organization (IMO) regulations. Paik (1995; 2003; 2007b), Pedersen (1995; 2000), Simonsen (1997a; 1997b; 2000), Kitamura (1997; 2002), Brown (2002b; 2002a), Sajdak (2004), and Zhang (2002) have all recently contributed to the current state-of-the-art of the mechanics and modeling of collision and grounding.

Grounding incidents can be differentiated into grounding on a sloping sea floor and grounding on protruding rocks. While the former is analogous to an icebreaker sliding up onto level-ice (i.e. the normal mode of icebreaking), this type of interaction is not within the scope of this research. The later type of grounding, however, is analogous to progressive damage from ice. The major concerns for grounding on rocks are damage to the hull, oil outflow (for oil tankers), and hull girder strength (Wang, Spencer, and Chen 2002). Damage resulting from grounding can have a detrimental effect on the capability of the ship to carry its design load. This has been the subject of much research, and provisions for damaged structural capacity are included in the ship structural rules from all major ship classification societies.

1.4.2 Collision physics

Impacts/collisions are common occurrences for all types of ships worldwide. Damage to a ship's hull can result from collisions with other ships or other floating objects (e.g. sea ice); collisions with stationary objects (e.g. piers, bridge supports, and level ice); and collision with submerged objects (e.g. rocks and anchor ice).

Analysis of the physics of ship impact/collision is usually divided into two parts: external mechanics and internal mechanics (Pedersen 1995). External mechanics deal with the rigid body motion of the ship during impact as well as the hydrodynamic pressures over its wetted surface. Internal mechanics encompass the ship's structural response during an impact/collision and subsequent deformation. External and internal collision mechanics can be treated separately or coupled, depending on the analysis. The research presented in this thesis entirely neglects external mechanics and concentrates wholly on the ship's structural response (internal mechanics) to progressive damage. The reasons for this are twofold: the numerical model developed herein was created in order to study progressive damage at a basic structural level (i.e. internal mechanics) and to identify the associated failure mechanisms; and the numerical model was validated against experiments that also neglected the external mechanics.

Internal collision mechanics usually describe the structural response of the ship in terms of shell membrane tension; shell rupture; web frame bending; shear and compression loads; yield strength; failure-strain; friction; and crushing and tearing of decks, bottoms.

and stringers. Literature suggests that when modeling collisions, plastic bending of the shell plating is considered negligible, and that it is safe to assume that plastic membrane tension is the primary mechanism of shell energy absorption and is the first mechanism that takes place in a collision (i.e. before bending/buckling of transverse web stiffeners) (Brown 2002a). Plastic shell membrane tension actually accounts for the greatest percent of all structural energy absorption during a collision (Kitamura 1997).

1.4.3 Methods for analysis/prediction of internal mechanics

To date, four main methods are used to analyse internal mechanics (Wang et al. 2006); they are: simple formulae, simple analytical models, simplified finite element models (FEM), and nonlinear FEM. Simple formulae involve few hand calculations and are used to estimate the initial energy absorption. Simple analytical models utilize more complex hand calculations, but offer more accurate energy and load predictions. Simplified FEM provide relatively fast energy and load predictions and are applicable in situations where computing power is limited, or where the problem is extremely large (e.g. simulation of a ship-ship collision where both ships are entirely modeled, and they are both deformable). Nonlinear FEM are the norm for collision analyses (Wang et al. 2006); they represent the most accurate methods of predicting collision energy, loads, and stresses. They also have the ability to model structural and material failure.

1.5 Steel Grillage Load-Displacement Behaviour

On a basic level, steel ship structures are composed of stiffened steel panels with stiffening provided by primary and secondary structures. Primary stiffeners may be transverse frames in a transversely framed ship or longitudinal frames in a longitudinally framed ship. They are usually constructed from thick steel plate. Secondary stiffeners may be the vertical or horizontal stiffening attached to the hull plating. These stiffeners are commonly constructed from thinner steel plate and serve to transfer hull loads to the primary stiffeners while maintaining the shape of the hull plating.

The load-displacement behaviour of a stiffened steel plate (Figure 1-2) exhibits many of the same phenomena as that of a steel uniaxial tensile test specimen (Figure 1-3) – including a linear elastic region, a yield point, an ultimate strength, and a failure-strain. The main difference between the two lies in their post-yield behaviour. Post-yield behaviour of a uniaxial tensile test specimen generally exhibits a smooth incline from the yield plateau¹⁰ to the ultimate strength; generally known as strain-hardening. The post-yield response of a structure may be similar, or it may exhibit other post-yield phenomena before it reaches its ultimate strength (e.g. stiffener buckling, weld failure, etc...) depending on the type of stiffening utilized within the structure (see Abraham (2008) for a discussion on load-displacement responses of various stiffener configurations).

¹⁰ The yield plateau is the section of the stress-strain curve for a steel uniaxial tensile test specimen where the level of stress remains relatively constant as the strain increases. This section immediately follows the elastic portion of the curve and represents the onset of permanent (plastic) structural deformation.

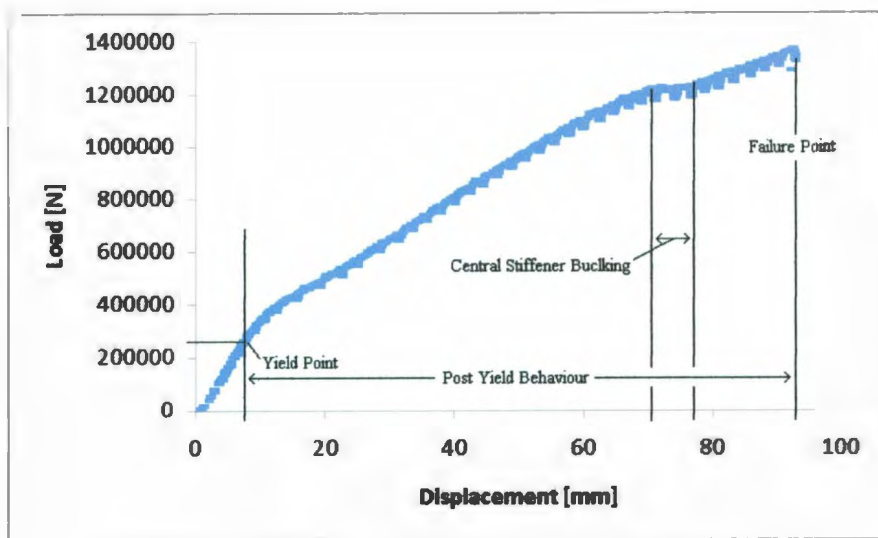


Figure 1-2: Load-displacement curve for a steel stiffened panel.

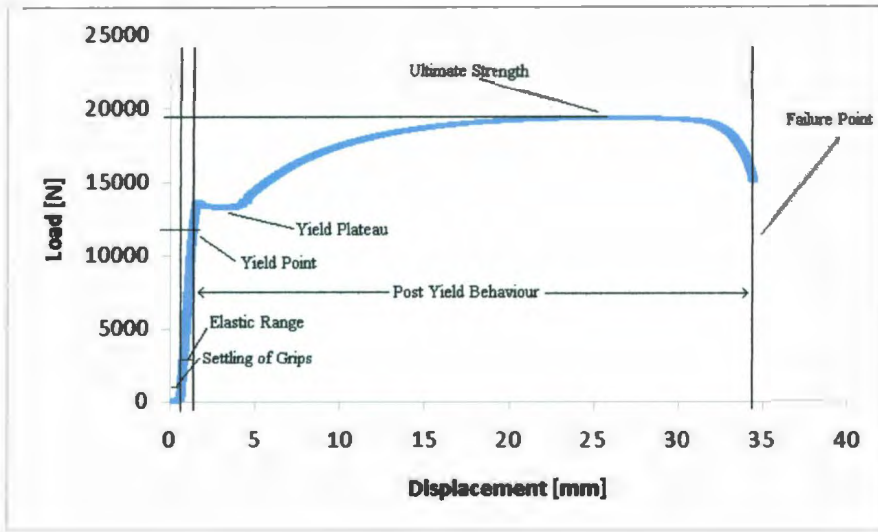


Figure 1-3: Load-displacement curve for a steel uniaxial tensile test specimen.

The numerical model developed in this thesis is validated by comparing the load-displacement curves obtained from it with those of the large grillage experiments outlined in Chapter 2.

1.6 The Finite Element Method

The finite element method is the industry standard numerical modeling method with which to model ship structures (Paik et al. 2003; Kitamura 2002; Sajdak and Brown 2004; Paik and Pedersen 1996).

1.6.1 Classes of finite element codes

Finite element codes may essentially be classed according to two categories: time and linearity. Codes that solve equations that explicitly include time are called *explicit codes*, while codes that do not are called *implicit codes*. Codes that solve equations with nonlinearities are called *nonlinear codes*, while codes that do not are called *linear codes*. Any finite element code must be classed from both of these categories simultaneously; for example, a code that includes time, but solves only linear equations would be an *explicit linear code*, and a code that excludes time but includes nonlinearities would be an *implicit nonlinear code*.

1.6.1.1 Implicit and explicit time integration

Unlike implicit analyses, in order to perform an explicit analysis, a time vector must be defined and the initial inertial properties (velocity, translational mass, and moments of inertia) of all bodies must be defined at time zero.

An implicit code basically solves the following equation for $\{x\}$ by inverting the stiffness matrix $[K]$:

$$[K]\{x\} = \{F\} \quad [1]$$

where: $[K]$ is the stiffness matrix
 $\{x\}$ is the displacement vector
 $\{F\}$ is the force vector

An explicit code basically solves:

$$[M]\{a\} + [C]\{v\} + [K]\{x\} = \{F\} \quad [2]$$

where: $[M]$ is a diagonal lumped mass matrix
 $\{a\}$ is the acceleration vector
 $[C]$ is the damping matrix
 $\{v\}$ is the velocity vector
 $[K]$ is the stiffness matrix
 $\{x\}$ is the displacement vector
 $\{F\}$ is the force vector

While this appears to be a more complicated equation than equation [1], it is solved for $\{a\}$ instead of $\{x\}$; implying that the stiffness matrix does not have to be inverted, which is a computationally expensive operation. Inversion of the mass matrix $[M]$ is trivial because it is a diagonal matrix as all masses are assumed to be lumped masses (Imaoka 2001). This tends to make solving an explicit finite element problem more efficient than an implicit one.

1.6.1.2 Sources of finite element nonlinearities

Nonlinearities may result from many of the inputs that define a numerical model including geometric, material, and boundary conditions. Geometric nonlinearities arise when structural deformations go beyond what is considered small¹¹. Material nonlinearities occur when the stress-strain curve for a material is nonlinear or when the stress-strain curve is a function of time (i.e. strain-rate effects); an example of a material for which the stress-strain curve is nonlinear and depends on time is steel (see Figure 1-3 for a nonlinear load-displacement curve). Boundary condition nonlinearities arise from boundary conditions that change with time, deformation or some other user-defined parameter. Examples of boundary condition nonlinearities are tied nodes¹², spring boundary conditions, contact between two or more bodies, and sliding friction.

1.6.2 Finite elements

There are generally four main classes of finite elements: point elements, line (or 1D) elements, surface (or 2D) elements, and solid (or 3D) elements. These classifications refer to the geometry of the element rather than the element's degrees of freedom. For further clarification, 1D and 2D elements may be oriented arbitrarily in 3D space. Within each class of finite elements there are different types of elements. For example, truss and beam elements are two types of line (1D) elements. A truss element connects two nodes and its nodes that may be generally displaced, but rotation about the node is not possible.

¹¹ Small deformations are generally those for which $\sin \theta \approx \theta$; where θ is the angle between the deformed and non-deformed geometries.

¹² Tied nodes are two or more nodes that occupy the same space at the same time and are considered as a single node until some user-defined parameter is met, at which point they split apart and are treated separately.

A beam element is like a truss element, but it may be rotated about its nodes and thus it has a finite bending stiffness. Beam elements also accept cross-sectional parameters as input (rather than defining them using a strict geometric definition in terms of nodes) thus simplifying the simulation of any beam cross-sectional shape (e.g. I-beam or bulb cross-sections). Similar analogies for surface (2D) elements exist; a plate element connects at least three nodes and generally does not support rotation about its nodes. It also has zero through-plane thickness (i.e. the plate is infinitely thin). A shell element supports rotation about its nodes and has a through-plane thickness (the thickness not defined geometrically but instead as a property of the shell element). Rotation for point elements and solid elements about their nodes is not generally supported.

The elements normally used for ship structural analyses depend on whether the analyses require small or large deformations (i.e. linear or nonlinear analyses). Linear analyses often utilize shell elements to model a ship's hull plating (Paik et al. 2003; Sajdak and Brown 2004; Servis and Samuelides 1999), and beam elements to model its primary (e.g. main transverse/longitudinal frames) and secondary stiffening (e.g. intermediate transverse/longitudinal frames) (Sajdak and Brown 2004; Servis and Samuelides 1999). Ship hulls are constructed from steel plate, which is much thinner than it is wide and long (or in terms of coordinate axes, the z-direction dimension is much smaller than the x- and y-direction dimensions). As mentioned above, thickness is a property of a shell element rather than part of its geometric definition; thus, shell elements are designed to model structures that have one dimension much smaller than the other two. Shell elements are also capable of modeling the bending reaction of hull plating to imposed loads. Solid

elements may be used instead of shell elements to model steel plate, but shell elements require far fewer nodes and provide similar results. Shell elements, therefore, drastically reduce the computational cost of a numerical model compared to solid elements for modeling ships' hull plating. For these reasons shell elements are the norm for linear numerical analyses of hull plating. Beam elements are used to model primary and secondary stiffening because they have bending stiffness (which depends on the beam's cross-section area properties as inputs) and they require only two nodes per element. Again, solid elements could be used to model the primary and secondary stiffening, but the computational costs would be enormous in comparison.

For nonlinear numerical analyses of ships' structures, it is common to use shell elements to model both the hull plating and the primary and secondary stiffening. Beam elements are not used for large structural deformations because they do not generally model membrane stresses or capture the through-thickness thinning¹³ of the beam's webs and flanges. As an illustration, once a stiffener buckles and folds over onto the nearby hull plating (see Figure 1-4), its bending stiffness is small in comparison with the membrane forces acting along its length. Shell elements can model both membrane and bending stresses.

¹³ Due to Poisson's effect.

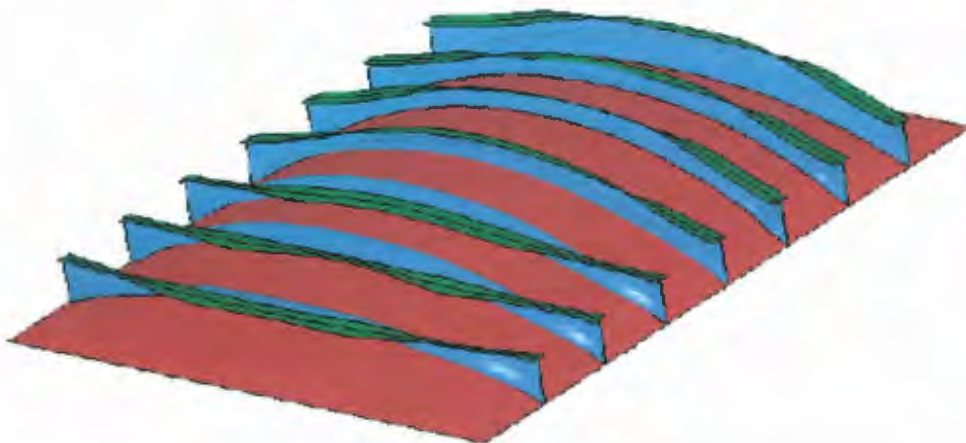


Figure 1-4: Illustration of buckled and folded stiffeners and hull plating.

1.6.2.1 Element formulation

A finite element generally requires an *element formulation* to be defined. An element formulation defines the physics modeled by an element, and how those physics are implemented by the element. Many different element formulations may be applicable to any given type of element. For example, a shell element may be used in a numerical heat transfer study instead of a structural study; or to continue the structural example from above – a linear analysis of a ship’s hull would not require that membrane stresses be considered in the element formulation but a nonlinear analysis might; therefore a different element formulation would be used for each situation.

1.6.2.2 Hourgassing

Hourgassing is the term given to the high-frequency, zero-energy vibration modes of finite elements. These modes do not exist in the real world, and generally result from

using an element formulation that attempts to eliminate shear locking by employing a reduced integration scheme. Please refer to section 3.3.2 for a discussion of shear locking and reduced integration. Hourgassing causes abnormal deformations in a finite element mesh and is distinguishable by its zigzag appearance (Figure 1-5).

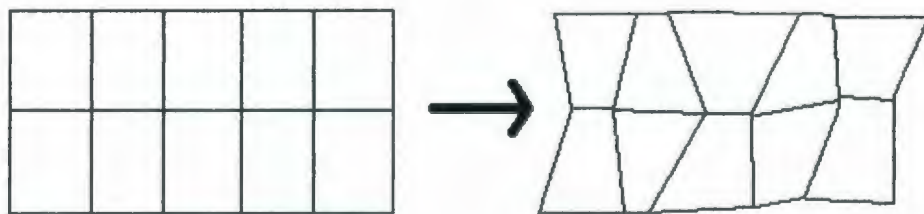


Figure 1-5: Hourgassing in a finite element mesh.

Hourgassing may be controlled within an element formulation by the introduction of artificial stiffness or viscosity (Olovsson, Simonsson, and Unosson 2006). Hourgassing may be prevented by utilizing a uniform mesh, avoiding concentrated loads at a single point, and refining coarse meshes (ANSYS Inc. 2007a). It may be prevented entirely by utilizing fully integrated elements, but at a substantially increased computational cost, and requiring some other form of shear locking control.

1.6.3 LSTC – explicit nonlinear finite element codes

Livermore Software Technology Corporation (LSTC) provides several commercial distributions of the widely used *dyna2D* and *dyna3D* explicit numerical modeling codes.

The first *Dyna* code was created by John Hallquist at Lawrence Livermore Laboratories, and was publicly released in 1976 (Belytschko, Liu, and Moran 2000).

LSTC's most notable software distribution is a nonlinear explicit finite element code called "LS-Dyna" which is mainly intended to run on a single computer (although it may be run in parallel on several processors). LSTC also produces a version of LS-Dyna that is ported to run on many computers simultaneously (i.e. multiple individual computers with one or more processors per computer that are all linked by a network) called "MPP-Dyna". MPP-Dyna has most of the capabilities of LS-Dyna; however, its ability to run on a computer cluster¹⁴ allows it to solve large numerical problems much more quickly than LS-Dyna. When run on a computer cluster, MPP-Dyna has far greater computing power than any stand-alone personal computer running LS-Dyna. Depending on the problem, higher accuracy can be achieved by utilizing: a more complicated model geometry (e.g. well defined curves and curved surfaces); a finer finite-element mesh; a highly detailed material model (or models); more complex sliding friction and contact models; and a longer *simulation-time*¹⁵ allowing a more accurate development of phenomena that occur before and after the point of direct interest (e.g. waves in a simulation involving fluid-structure interaction). Generally, a numerical model that involves all of the above improvements would be considered a large model. Of course LS-Dyna is capable of solving any large model, but increasing model complexity will drastically increase *run-*

¹⁴ A computer cluster is a group of separate computers that are linked via a high-speed connection and which interact in a manner that resembles a single computer, thus providing supercomputer-like computing power.

¹⁵ Meaning the amount of time simulated, not the length of time required by the computer(s) to solve the problem.

*times*¹⁶. MPP-Dyna allows complex models to be solved within a time frame that is comparable to a simpler model solved using LS-Dyna, thus providing more realistic results.

As a point of note, because both LS-Dyna and MPP-Dyna are nearly identical in the results they are capable of producing (regardless of how the results are achieved), the term “Dyna” will be used henceforth when referring to the numerical simulation software utilized for this thesis. The terms MPP-Dyna and LS-Dyna will only be explicitly written when a statement does not apply to both versions of the software.

Dyna is an extremely robust nonlinear finite element code. It solves equations which explicitly include time. This implies that a reaction to an applied load requires time to propagate throughout the structure (i.e. a stress wave travels from the point of application of the load throughout the structure with time), unlike implicit finite element codes in which reactions are experienced instantaneously throughout the whole structure (because implicit codes solve equations that do not involve time). Explicitly including time in a simulation allows the dynamic response of a structure to be modeled; specifically, velocity and acceleration effects such as damping and inertia are explicitly included in the simulation along with material rate effects and other time-dependent phenomena.

A progressive damage scenario is inherently dynamic – it involves a collision followed by a dragged indentation in a ship’s hull. This makes an explicit nonlinear finite element

¹⁶ Meaning the amount of time required by the computer(s) to solve the problem.

code the ideal choice with which to model progressive damage. Further, the inherent efficiency of an explicit code over an implicit code in actually performing the calculations to solve a numerical model allows for a larger number of numerical simulations to be conducted in the same timeframe. For these reasons, the MPP-Dyna code was used exclusively to carry out the research presented in this thesis.

1.6.3.1 MPP-Dyna and model decomposition

MPP-Dyna Version 9.71 Release 3.1 for LAM Version 6.5.9 was used exclusively throughout this work and was run on both of IOT's *Beowulf clusters*; the details of which are given in Appendix A: Beowulf Cluster Specifications.

MPP-Dyna solves a numerical simulation by distributing the problem over many computers. It accomplishes this by breaking the problem up into as many parts as there are separate computing entities available on which to run the simulation. A computing entity is a single computer processor. For example: each computer on one of IOT's Beowulf clusters has two processors (and therefore two processing entities); the cluster is composed of 15 computers, thus providing a total of 30 processing entities that MPP-Dyna can utilize.

A numerical model is broken into parts by dividing the finite element model into sections and solving each section on a separate computer processor. The term *decomposition* is used to describe the process of dividing the model into sections. Decomposition is

accomplished via one of three methods: the automatic method “GREEDY”, the automatic method “Recursive Coordinate Bisection (RCB)”, or manually by the user. The GREEDY method is a simple neighbourhood expansion algorithm (LSTC 2007a). The RCB method recursively divides the model in half by slicing the section on which it is working along its longest axis; this method tends to generate cube shaped sections aligned along coordinate axes (LSTC 2007a). The manual method allows the user to decompose the model. If manual decomposition is not required by the model’s geometry, the RCB method generally gives the best performance (LSTC 2007a).

2 LARGE GRILLAGE EXPERIMENTS

The large grillage experiments presented in this section were designed and carried out by Daley and Hermanski (2008a; 2008b). The author was present for, and participated in these experiments. They are the latest in a series of experiments that are part of an ongoing comprehensive study of the ultimate strength of ships' frames. These studies are jointly funded by Transport Canada, the United States Coast Guard, and the US-Canada Ship Structures Committee. The research presented in this thesis is an extension of these experiments, and hence they form the basis for the validation of the numerical model presented in Chapter 3.

2.1 Introduction

The large grillage experiments were carried out to examine the behaviour of a ship's basic structure (i.e. a stiffened panel) to excessive plastic damage at multiple locations along its length. It was postulated that a ship structure has substantial plastic reserve capacity beyond its yield point (i.e. its elastic capacity).

During the experiments, two near-identical full-scale models of a stiffened ship's side-panel (meeting IACS (IACS 2007) ice-class requirements) were quasi-statically loaded with a hydraulic ram at three points along their lengths. Analysis of the test data suggests that the large grillage structure (not necessarily the whole ship) became stiffer (i.e. had progressively higher resistance to further plastic damage) with each additional damaging load along its length. These results are interesting and support the theory that ships have

enormous plastic reserve when they are designed for a yield-stress limit state (i.e. they are possibly well over-designed).

This process of loading and unloading the large grillage structure repeatedly along its length discretely simulates progressive damage to a ship's hull. This is because the response of each newly loaded area is affected by the residual stresses locked in the structure by the plastic damage from previous loads.

2.2 Large Grillage Model

The large grillage model shown in the upper part of Figure 2-1 is a full-scale representation of a section of a ship's outer hull that is built to "IACS polar class" (IACS 2007). It is a stiffened plate structure that is 6.756 m long and 1.5 m wide and is constructed entirely of 350MPa (nominal) steel. If one assumes that this model is from a transversely framed ship, then the primary stiffening is provided by two 325 x 18 / 120 x 18 FF transverse frames and the secondary stiffening is provided by three 200 x 8 / 75 x 10 FF longitudinal stiffeners (see Figure 2-2). The transverse frame spacing is 2000 mm.

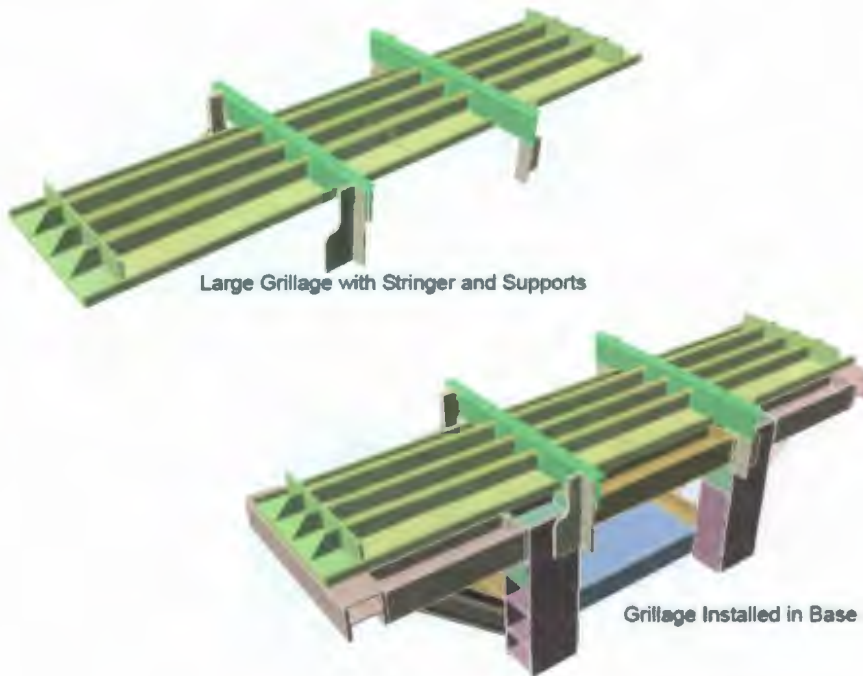


Figure 2-1: Large grillage model – isometric view.

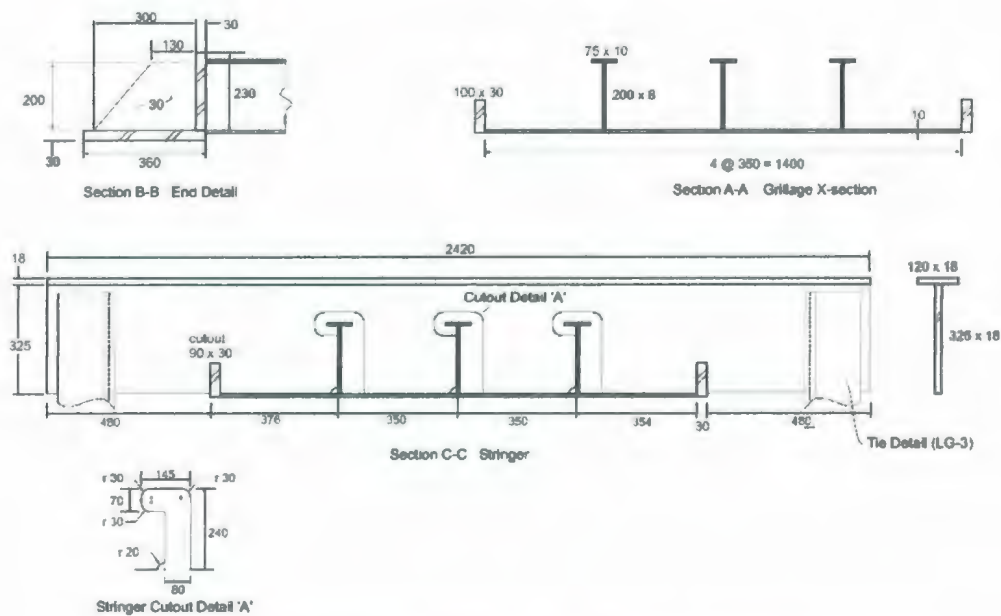


Figure 2-2: Large grillage model primary and secondary stiffening arrangement.

2.2.1 Structural components

The large grillage structure may be broken up into five distinct components: the hull plating; the transverse frames; the longitudinal frame webs; the longitudinal frame flanges; and the boundary structure. The longitudinal frame webs and flanges are broken into separate components because they are constructed from steel of a different nominal thickness, that was cut from different types of stock (as outlined below).

The “hull plating” was constructed from 10 mm (nominal) steel plate and was meant to represent the outside hull plating of an ice-strengthened ship. The hull plating was the portion of the large grillage structure to which the loads were directly applied. The transverse frames were constructed from 18 mm (nominal) steel plate and were meant to represent the primary stiffening. The longitudinal stiffener webs were constructed from 8 mm (nominal) steel plate and were meant to represent part of the secondary stiffening. The longitudinal stiffener flanges were constructed from 10 mm (nominal) steel flatbar of width 75 mm, and were meant to represent the other part of the secondary stiffening. The boundary structure does not correspond directly to any part of a ship’s structure; however, it was designed to provide boundary conditions for the large grillage structure, consistent with the boundary conditions that would exist if the model was infinitely surrounded by other identical grillage structure (Daley and Hermanski 2008b). The boundary structure was constructed from 30 mm (nominal) steel plate.

2.3 Boundary Conditions

The large grillage model was attached to an extremely robust steel test frame (the large grillage is shown mounted to the test frame in the lower part of Figure 2-1). It was expected that no plastic deformation of the test frame took place during the experiments, and because the plastic deformations of the large grillage model were so large, any elastic deformation of the test frame is considered negligible. The large grillage structure was bolted to the test frame at its longitudinal ends (see Figure 2-3), and at ends of the transverse frames using the attached brackets shown in Figure 2-1. The bolt pattern was such that the model was restrained in all six degrees of freedom (DOF) (i.e. surge, sway, heave, roll, pitch, and yaw).



Figure 2-3: Large grillage end boundary condition.

2.4 Instrumentation

The hydraulic ram was outfitted with a pressure transducer and a *yoyo-pot*¹⁷. The pressure transducer was calibrated to report the reaction force of the large grillage in pound-force (lbf) and the *yoyo-pot* was used to measure the hydraulic ram's extension in millimetres (i.e. the depth of ram's indentation into the large grillage structure). The large grillage structure was instrumented with 80 strain gauges placed throughout the structure. Finally, a *microscribe*TM¹⁸ was used to measure the total deflection of the central stiffener (i.e. vertical and buckled displacements) throughout the experiment at eleven points on the stiffener above the load patch: eight points on the stiffener web and three points on the T-flange.

Data was collected using the hardware outlined in Appendix B: Large Grillage Data Collection Equipment and Specifications, coupled with National Instruments "Measurement and Automation" software.

2.5 Loading Scenario

This large grillage model was loaded on the "outer" side of its hull plating (i.e. what would be the outside of the ship's hull) between the transverse frames and along the central longitudinal stiffener. Figure 2-4 shows the location of the three load patches. A 500 kip Enerpac® industrial grade hydraulic ram (shown in Figure 2-5) was used to apply

¹⁷ A *yoyo-pot* is a linear potentiometer that uses a spring loaded spool of twine as its actuator.

¹⁸ A *microscribe*TM is a 3D digitizing device used to capture the geometric properties of a real object in 3D digital space (<http://www.3d-microscribe.com/>).

the load. A 130 mm x 130 mm thick steel block (i.e. the indenter) with a rounded top was placed between the ram and the large grillage plate. This was done to control the area of the application of the load. The rounded top tended to “soften” stress concentrations that would arise if the indenter had sharp edges. Loads were applied at the load patches by the hydraulic cylinder in small discrete steps using a trigger activated hydraulic fluid pump. Initial loading (from the elastic to moderately plastic range) was applied in increments of 10 kip up to 150 kip. Loads subsequent to this were applied in displacement increments of 2 mm; up to either a resulting load of 350 kip (approximately 1.56 MN) or plate failure.

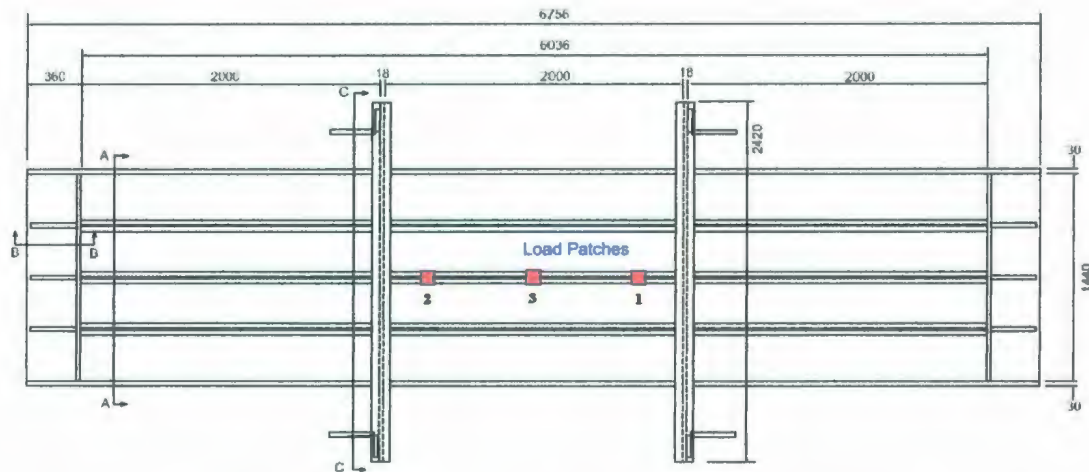


Figure 2-4: Large grillage model – top view with load patches.



Figure 2-5: 500 kip Enerpac® industrial grade hydraulic ram.

2.6 Experimental Procedure

The 300 kip hydraulic ram was positioned and secured below “load patch 1,” the centre of which was 450 mm away from the transverse frame (shown in Figure 2-4). The ram was then actuated in a quasi-static nature (i.e. slow, small incremental loads) until either a 350 kip force was achieved, it was apparent that structural failure was imminent, or sudden structural failure occurred. The ram was then lowered to its start position and moved to load patch 2 (450 mm away from other transverse frame) and the procedure was repeated, and similarly again for load patch 3 (centre of large grillage structure). The entire test setup is shown in Figure 2-6.



Figure 2-6: Large grillage experimental setup.

2.7 Results

Applied load, structural deformation, and structural strain were recorded throughout the experiments. The strain data is not used or reported in this thesis for reasons explained in Chapter 3 concerning the relationship between finite element strain and finite element size. The load-displacement curves for the loads applied to each of the three load patches are given in Figure 2-7. The discrete load increments can be observed in this plot by the slight dips in each load-displacement curve. These slight dips correspond to a slight reduction in load after each increase in load was applied. These slight reductions were attributed to a “bleeding off” of hydraulic fluid pressure through the system used to serve the hydraulic ram and are of little consequence to the overall results.

While intrinsically obvious, it should be noted here that the deflection values reported for loads applied on load patches 2 and 3 have their zero position corresponding to the *deformed* hull plate position, rather than the original (undeformed) position of the hull plating. If the zero point for deflections were based on the undeformed hull plate position, load would not increase from zero for the second and third load-displacement curves shown in Figure 2-7 until contact between the hydraulic ram and the hull plate was established.

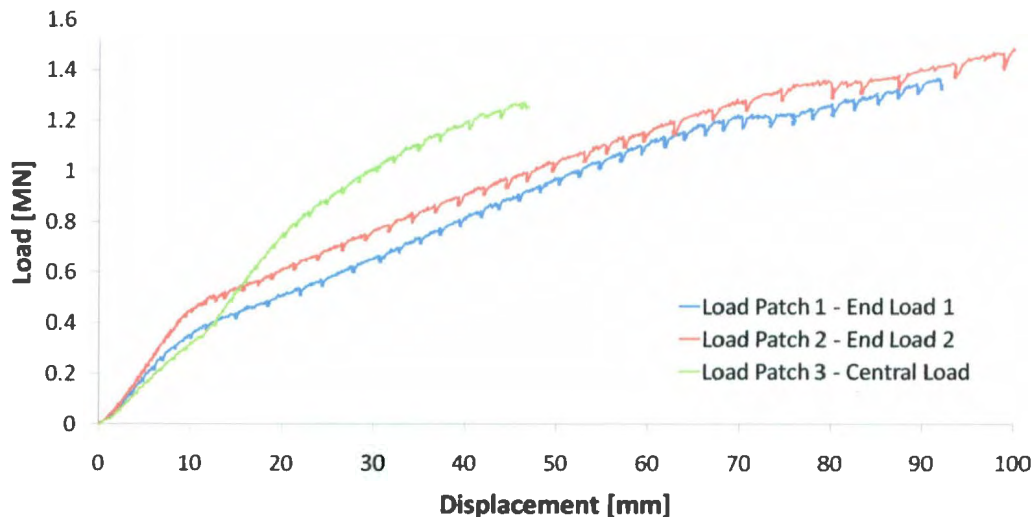


Figure 2-7: Load-displacement plot for loads applied to the three load patches.

2.7.1 Load patch 1

The overall load applied to load patch 1 reached approximately 1.37 MN at a deflection of 92 mm. The central longitudinal stiffener plastically buckled starting at a deflection of approximately 70 mm. The load-displacement curve for load patch 1 is shown in blue in

Figure 2-7; the structural reaction associated with the plastic stiffener buckling can be observed in the load-displacement curve as a flattening of the line starting at approximately 70 mm deflection.

2.7.2 Load patch 2

The load-displacement curve for load patch 2 is shown in red in Figure 2-7. Note that the position of load patch 2 is symmetric with load patch 1 about the transverse centreline of the large grillage structure. The overall load applied to load patch 2 reached approximately 1.49 MN at a deflection of 100 mm; the steel block indenter mentioned above punched through the steel plate along one edge at this load and deflection (shown in Figure 2-8). This time the central longitudinal stiffener did not plastically buckle until a deflection of approximately 80 mm was reached, indicating that the residual damage from loads applied to load patch 1 caused the longitudinal stiffener to have a greater resistance to plastic buckling (10 mm extra in this case). Further evidence exists to support this statement: notice that the modulus of the elastic portion of the second curve is larger than the first and, as well, more energy per unit deflection is absorbed for the second curve, than for the first (indicated by the area under each curve at any given deflection).

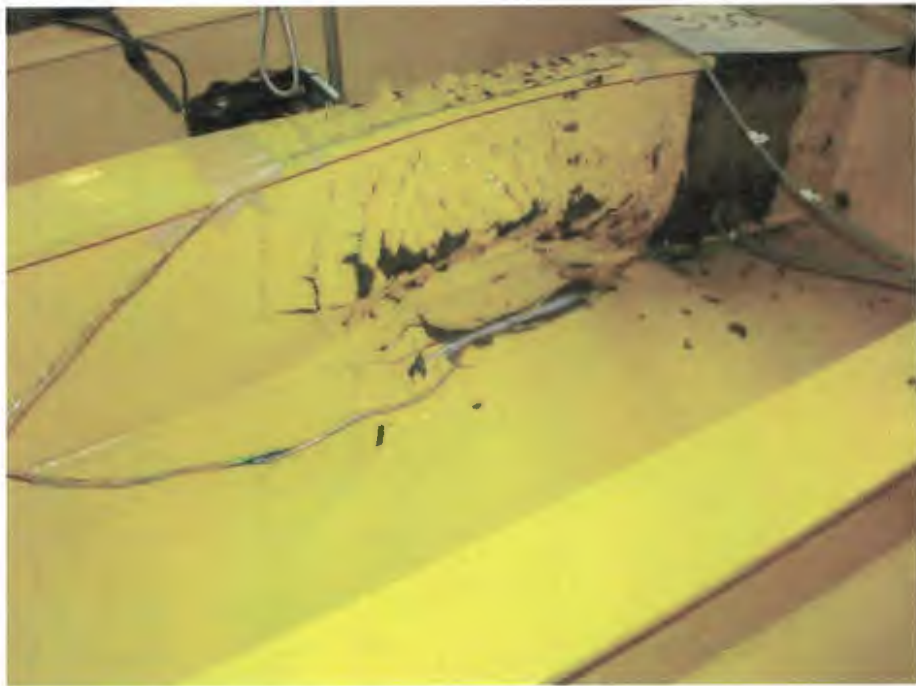


Figure 2-8: Fractured hull plating for load patch 2.

2.7.3 Load patch 3

The results for the third load patch also indicate an increasing overall stiffness of the central stiffener, however, these results are affected by the 150 mm (approximately) crack in the hull plating at load patch 2. The load-displacement curve for load patch 3 is shown in green in Figure 2-7. The point of plastic buckling is not evident from inspection of this curve, and compared with the first and second load patches, comparatively little plastic buckling occurred. From visual inspection of the structure, it appears that buckling occurred between 249 kip and 259 kip (see Figure 2-9). The overall load applied to load patch 3 reached approximately 1.27 MN at a deflection of 46 mm. The indenter punched through the steel plate along one edge at this load.



Figure 2-9: Photos showing approximate point of buckling for load patch 3.

2.8 Material Tensile Tests

Uniaxial material tensile tests were also performed. This was done to verify the material properties of the steel used in the fabrication of the large grillage structure. Where possible, scrap steel left over from the construction of the large grillage was used to create some of the tensile test coupons. Using scrap steel ensured that residual stresses from the experimental loadings were not present in the test coupons. However, scrap steel for the 8 and 10 mm steel plates were not available and therefore had to be cut from the second large grillage, subsequent to the experiments. In order to ensure that this steel was cut from a section of the large grillage in which no residual stresses were present (i.e. no strain-hardening), a numerical model (an early version of that outlined in Chapter 3) was created and loaded using nominal material properties. In an attempt to ensure that no permanent residual stresses would be present in the samples cut from the large grillage, they were cut only from areas of the structure that the numerical model showed to contain less than 250 MPa residual effective stress (von Mises criterion). Figure 2-10 shows all residual stress greater than 225 MPa as a light blue colour. This provided a nominal 100 MPa of safety margin as the steel was supposed to have a nominal yield stress of 350 MPa.

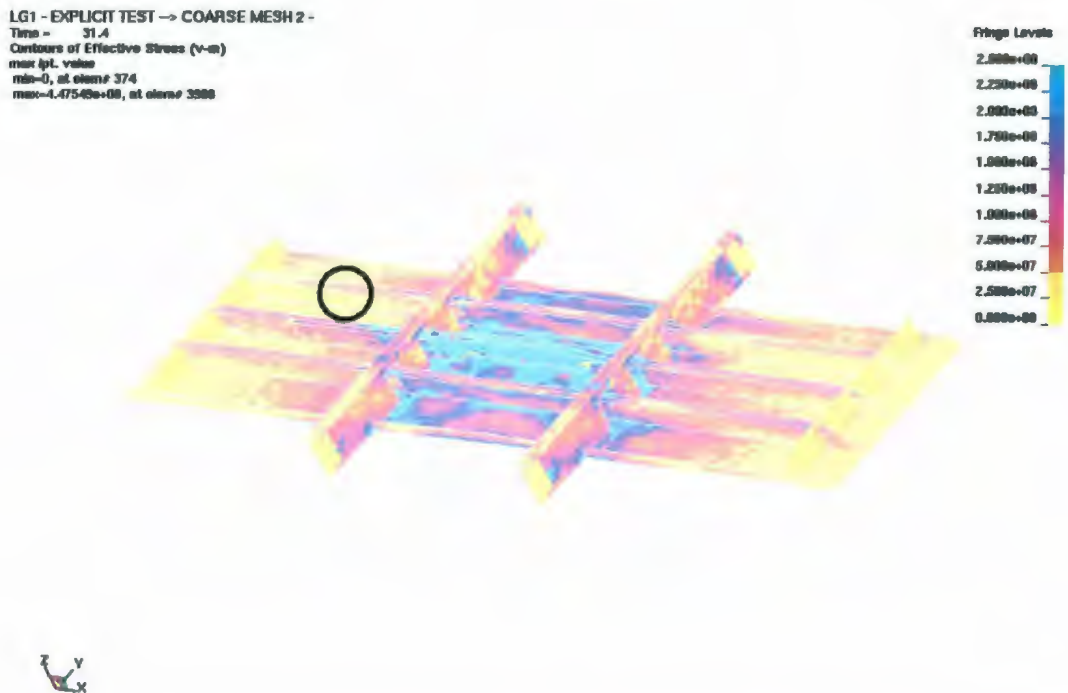


Figure 2-10: Preliminary numerical model - effective (von Mises) residual stress.

2.8.1 Test specimen specifications

In total five specimens were machined to the specifications shown in Figure 2-11 (where all dimensions are in mm). Figure 2-12 shows all five specimens.

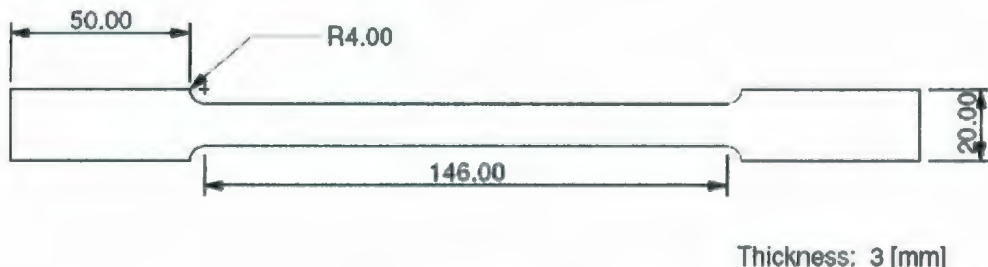


Figure 2-11: Tensile test specimen dimensions.



Figure 2-12: Tensile test specimens.

2.8.2 Instrumentation and apparatus

Tensile tests were carried out using an Instron 5585 H series tensile test apparatus (shown in Figure 2-13), the specifications of which are:

- 250kN (56,250 lbf) capacity,
- 0.001-500 mm/min (0.00004 – 20 in/min) speed range, and
- 1256 mm x 575 mm (49.4 in x 22.6 in) test area.



Figure 2-13: Instron 5585 H.

The apparatus was controlled via a computer running Instron's "Bluehill 2" software, which was also used to collect the data from the tensile tests. Load, displacement, and strain data were collected using instrumentation inherent in the apparatus.

2.8.3 Results

Results of each uniaxial tensile test are given below.

2.8.3.1 Specimen 1

Test specimen 1 was cut from 18 mm thick scrap steel that was used to construct the transverse frames of the large grillage structure. The engineering stress-strain plot for this specimen is shown in Figure 2-14. These results are flawed at an approximate strain of 0.085 mm/mm as shown by the sudden decrease in engineering stress corresponding to a slightly decreasing strain (circled section). While the ultimate strength data is missing, the yield stress and Young's modulus for this specimen are available and are presented in Table 2-1.

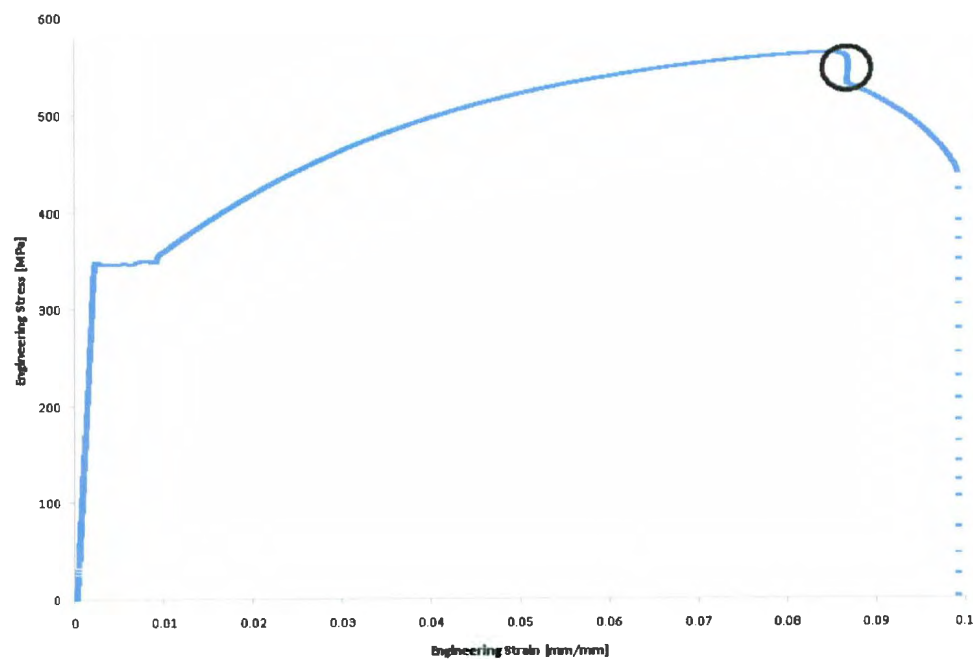


Figure 2-14: Stress-strain plot for uniaxial tensile test specimen 1.

Table 2-1: Material properties for uniaxial tensile test specimen 1.

Engineering Yield Stress MPa	Young's Modulus GPa	Engineering Ultimate Tensile Stress MPa	Engineering Failure Strain mm/mm
350	183	n/a	n/a

2.8.3.2 Specimen 2

Specimen 2 was cut from scrap 10 mm steel plate that was used to make the “hull plating” of the large grillage structure. The engineering stress-strain plot for this specimen is presented in Figure 2-15. It was apparent from analysis of the data that the test specimen slipped in the grips of the test apparatus at the start of the test. This slippage was only present for a small portion of the elastic range of the specimen; therefore, this bad data was removed and the zero point (i.e. the point that would have been the start point of the test had the specimen not slipped in the grips) was extrapolated using the remaining linear elastic portion of the curve. The material properties for specimen 2 are given in Table 2-2.

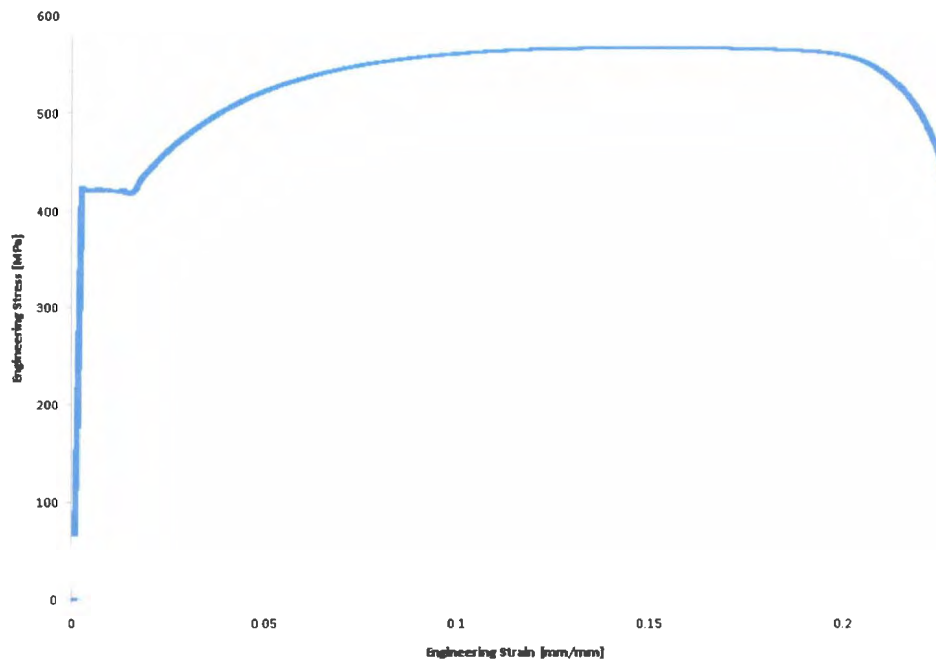


Figure 2-15: Stress-strain plot for uniaxial tensile test specimen 2.

Table 2-2: Material properties for uniaxial tensile test specimen 2.

Engineering Yield Stress MPa	Young's Modulus GPa	Engineering Ultimate Tensile Stress MPa	Engineering Failure Strain mm/mm
420	215	566	0.225

2.8.3.3 Specimen 3

Specimen 3 was one of two specimens cut from the large grillage structure as there was no scrap steel available from which to machine test specimens. The steel for these test specimens was removed from a longitudinal stiffener near one of the corners of the large grillage where the residual stress was shown to be quite low (the circled area of Figure 2-10). Specimen 3 was cut from a longitudinal stiffener web, which was constructed from steel plate that was nominally 8 mm thick. The engineering stress-strain plot for this

specimen is presented in Figure 2-16. Like specimen 2, there was minor slippage of the specimen in the grips of the tensile test apparatus. Again, this was limited to a small part at the start of the elastic region and the data was modified by hand to obtain the proper zero point. The material properties for specimen 3 are given in Table 2-3.

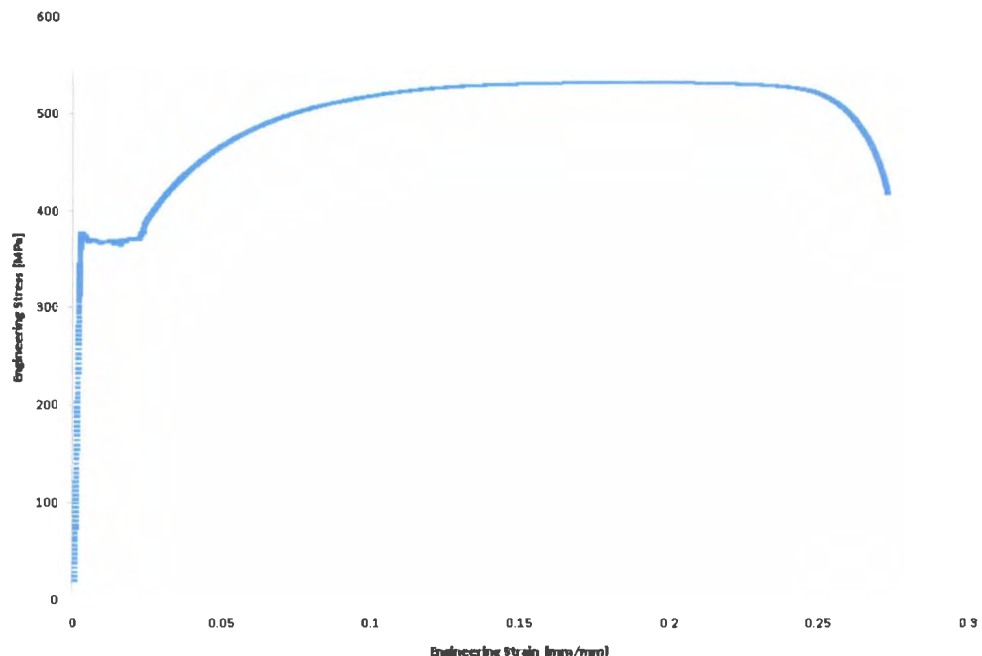


Figure 2-16: Stress-strain plot for uniaxial tensile test specimen 3.

Table 2-3: Material properties for uniaxial tensile test specimen 3.

Engineering Yield Stress MPa	Young's Modulus GPa	Engineering Ultimate Tensile Stress MPa	Engineering Failure Strain mm/mm
370	219	532	0.271

2.8.3.4 Specimen 4

Specimen 4 was cut from scrap 30 mm steel plate that was used to make the boundary structure of the large grillage structure. The engineering stress-strain plot for this specimen is presented in Figure 2-17. As with specimen 2 and 3, there was minor slippage of the test specimen in the grips of the tensile test apparatus. The data was modified similarly. The material properties for specimen 4 are given in Table 2-4.

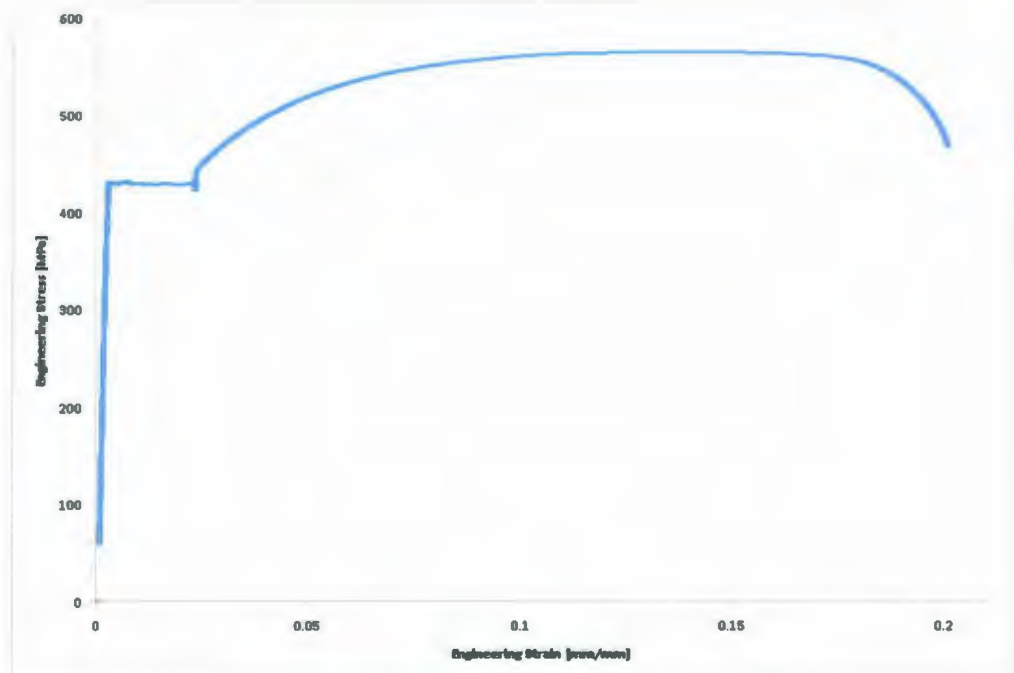


Figure 2-17: Stress-strain plot for uniaxial tensile test specimen 4.

Table 2-4: Material properties for uniaxial tensile test specimen 4.

Engineering Yield Stress MPa	Young's Modulus GPa	Engineering Ultimate Tensile Stress MPa	Engineering Failure Strain mm/mm
425	230	564	0.200

2.8.3.5 Specimen 5

Specimen 5 was the other specimen cut from the large grillage structure (cut from circled section of Figure 2-10). The steel for the test specimen was removed from a longitudinal stiffener “Tee”. The longitudinal stiffener “Tee” flanges were constructed from 75 mm wide steel flat bar stock that was nominally 10 mm thick. The engineering stress-strain plot for this specimen is presented in Figure 2-18. It was apparent from analysis of the data that test specimen slipped in the grips of the test apparatus at the start of the test. This slippage was only present for a small portion of the elastic range of the specimen; therefore, this bad data was removed and the zero point (i.e. the point that would have been the start point of the test had the specimen not slipped in the grips) was extrapolated using the remaining linear elastic portion of the curve. The material properties for specimen 5 are given in Table 2-5.

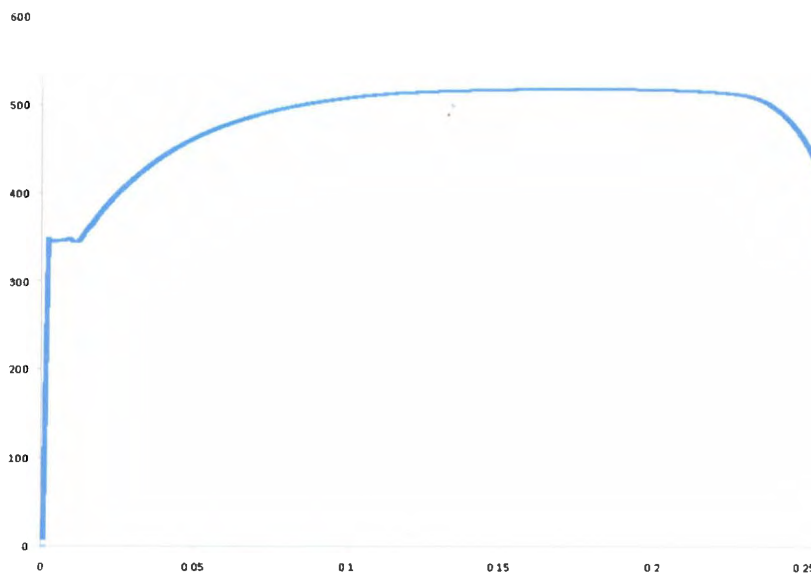


Figure 2-18: Stress-strain plot for uniaxial tensile test specimen 5.

Table 2-5: Material properties for uniaxial tensile test specimen 5.

Engineering Yield Stress MPa	Young's Modulus GPa	Engineering Ultimate Tensile Stress MPa	Engineering Failure Strain mm/mm
350	230	520	0.254

2.8.3.6 Summary of material properties for tensile test specimens

The material properties of the uniaxial tensile test specimens taken from each of the five major components of the large grillage structure are summarized in Table 2-6. These results suggest that the large grillage structure appears to be constructed from two types of steel, 350 MPa and 425 MPa steel; however, further testing is required to confirm this.

Table 2-6: Summary of material properties for the uniaxial tensile test specimens.

Specimen	Engineering Yield Stress [MPa]	Young's Modulus [GPa]	Engineering Ultimate Tensile Stress [MPa]	Engineering Failure Strain [mm/mm]
1	350	183	n/a	n/a
2	420	215	566	0.225
3	370	219	532	0.271
4	425	230	564	0.200
5	350	230	520	0.254
Average	383	215.4	545.5	0.2375

3 NUMERICAL MODEL

The numerical model developed in this chapter is the basis for the dynamic structural response predictions presented in Chapter 4. The numerical model was developed based on input from the large grillage experiments, literature, advice from experts, past experience, and trial-and-error.

3.1 Methodology

As mentioned above, an explicit nonlinear FEM is the natural choice with which to model a progressive damage scenario. Modeling large structural deformation requires nonlinear geometric and nonlinear material modeling capabilities. Modeling collisions, which are also intrinsic phenomena of progressive damage, requires contact detection and explicit time integration. MPP-Dyna is an explicit nonlinear finite element code that has all the capabilities required to model progressive damage to a ship's structure. It is used exclusively throughout this research.

The following inputs were required to define the numerical model:

- Geometric structural model
- Finite element mesh
 - Element types
 - Element parameters
 - Mesh conversion study
- Material model
- Boundary conditions
- Part definition

- Contact definition
- Load definition
- Damping definition
- Solution control parameters
- Results declaration
- Trial runs and modifications from trial-and-error (i.e. design spiral)

The development of a numerical model is very much a design spiral; for example, the geometric structural model depends on the finite element mesh because 2D elements must overlay 2D geometric surfaces. A solid geometry, like a solid sphere or a solid box, cannot be meshed with beam (1D) or shell (2D) elements. Other aspects of a numerical model that are particularly influenced by the design spiral are element parameters, material models, contact definitions, load definitions, damping definitions, and solution controls. A complex explicit nonlinear numerical model is often a delicate balance of these numerical modeling inputs. This numerical model in particular could not have reached this delicate balance without validation against real physical experiments. The aspects discussed below are presented in their final state and reflect many revolutions of the design spiral.

3.2 Geometric Structural Model

The large grillage numerical model was created using the ANSYS® pre-processor¹⁹, PREP7 (ANSYS Inc. 2007b). As with most pre-processing software, two coincident 3D

¹⁹ Note that three different pieces of software are usually used when conducting research with numerical models; they are a pre-processor, a solver, and a post-processor. The pre-processor is used to create an

spaces exist that are both used in the creation of a numerical model – these are the geometric space and the finite element space. The geometric space contains points, lines, areas, and volumes. The finite element space contains nodes and elements. A numerical model may be created without using the geometric space, but this becomes increasingly difficult as the complexity of the model's geometry increases. Generally, a model is created by first defining its geometry with points, lines, areas, and volumes (if necessary). The geometric model is then *meshed* – a process which overlays the geometry with applicable finite elements. The result is a collection of nodes and elements of a user-defined density with the same overall dimensions and geometric characteristics as the geometric model. Two methods are generally used to create a geometric model: the bottom-up approach and the top-down approach (ANSYS Inc. 2007b). The bottom-up approach involves starting with simple geometric entities (e.g. points or lines) and using them to define more complex entities like areas and volumes. The top-down approach involves defining gross areas or volumes and refining those using Boolean operations. Of course, the simpler geometric entities required to define the complex ones are created automatically in the top-down approach.

The bottom-up approach was used to create the geometric model of the large grillage structure; that is, points were defined, then lines were created connecting the points (Figure 3-1), then areas were created using the lines (Figure 3-2).

input file that contains all the information about the numerical model (i.e. geometry, material model, boundary conditions, loads, etc...). The solver then processes this input file and outputs the results to several other types of files (e.g. geometry files, files containing stresses and strains and other data, etc...). A post-processor is then generally used to view the contents of the results files.

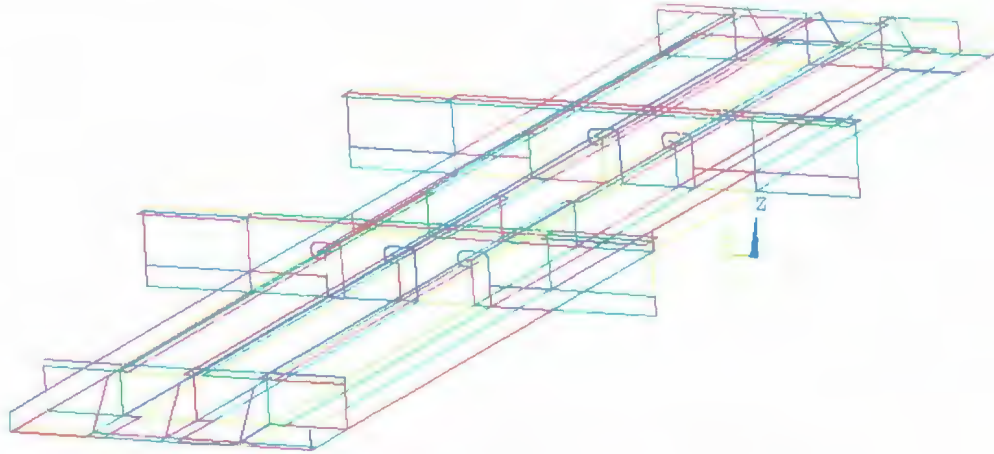


Figure 3-1: Large grillage geometric model showing lines.

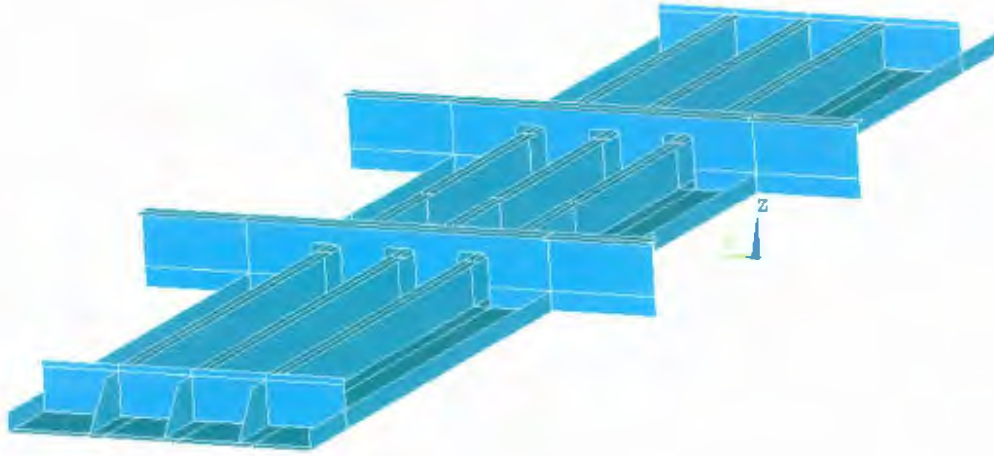


Figure 3-2: Large grillage geometric model showing areas.

As the complexity of a geometric entity increases, so too does the care required to define it. For example, a line connects two points, but the order in which the points are chosen to create the line defines the direction of that line. Elements overlaid on this line will inherit its direction, which may or may not be important depending on the problem. Areas have a normal direction. An analogy would be a top and a bottom. Again, surface

elements overlaid on an area inherit its normal direction. An element's normal direction is very important if the numerical model is to involve contact between various elements.

Care was taken to ensure that the area normals were appropriate throughout the geometric model of the large grillage structure. This was particularly important for the case of the hull plating, as this is the part that would be in contact with the indenter. All area normals were chosen to be pointing toward the “outside” of the hull plating, which is the outside of the ship. Figure 3-3 shows the direction of the shell element normals for the large grillage numerical model.

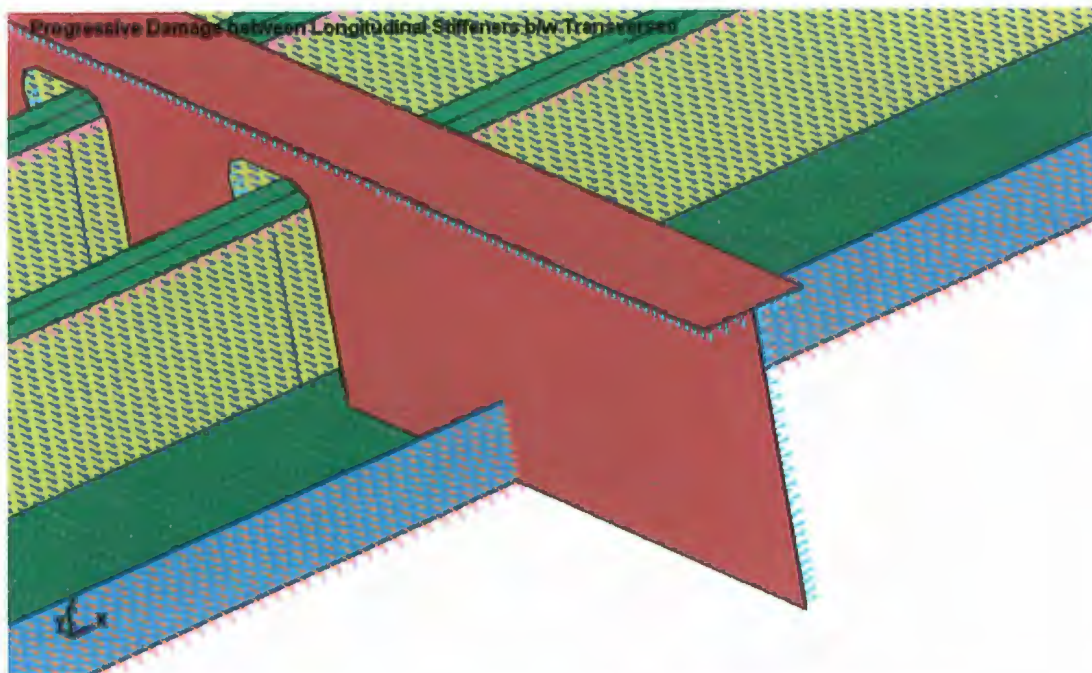


Figure 3-3: Plot of shell element normals for large grillage numerical model.

3.3 The Finite Element Mesh

After the geometric structural model has been created, it must then be meshed. Several steps are required to create a finite element mesh; they are, choice of finite element(s), choice of finite element parameters, and mesh density.

3.3.1 Element choices

All parts of the large grillage structure were constructed from steel plate and flat bar stock. Steel plate and flatbar stock have a thickness much less than their length and width. Shell elements can model plate structures efficiently. The general shell element in Dyna is a 4-node planar surface (2D) element that has bending and membrane capabilities. Each node has six degrees of freedom –translations and rotations in the x-, y- and z-directions. A shell element may be loaded in-plane and normal to its surface. They can model through plane thickness if the thickness is small compared with the length and width (see Figure 3-4). Shell thickness is input as a property of the shell element rather than with a strict geometrically definition using nodes. This gives shell elements a huge computational advantage over solid elements, which require up to 8 nodes per element to model the same physics.

Shell elements were used to model all five components of the large grillage structure defined in 2.2.1.

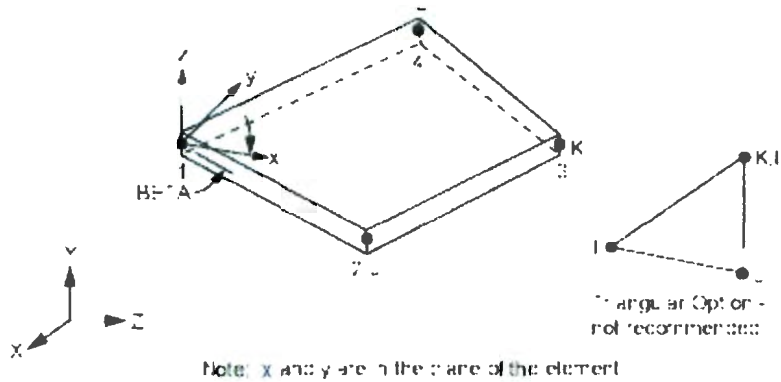


Figure 3-4: Shell element geometry (ANSYS Inc. 2007a).

The indenter (i.e. the 130 mm x 130 mm steel block between the ram and the hull plating of the large grillage structure) was modeled using 8-node solid elements (see Figure 3-5). The general solid element in Dyna is an 8-node brick (3D) element. Each node has three degrees of freedom: translations in the x-, y-, and z-directions. A solid element may be loaded at each node and on each face normal to its surface. Solid elements were used for several reasons: the first is that the indenter is thick compared to its length and width, thereby ruling out the use of shell elements; the second is more complicated and outlined below.

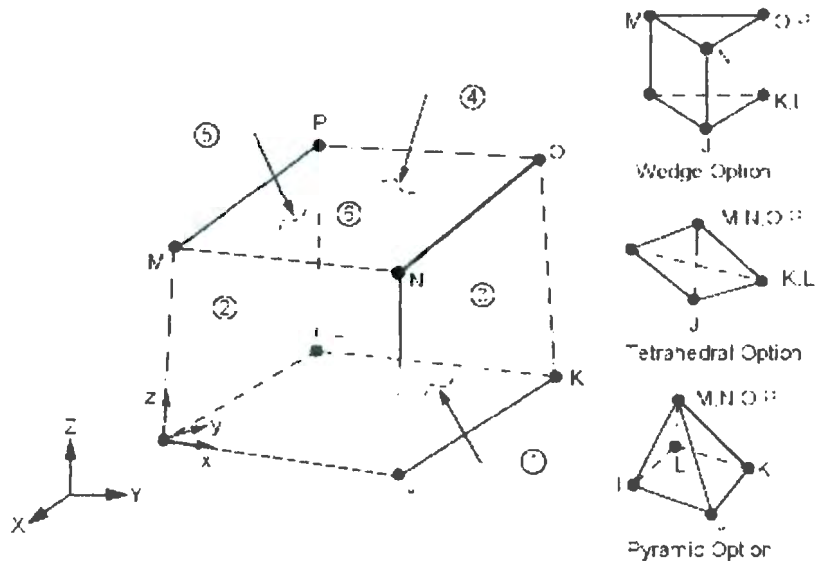


Figure 3-5: Solid element geometry (ANSYS Inc. 2007a).

The indenter used in the large grillage experiments was of sufficient size and thickness that it was not expected to suffer any plastic deformation. The magnitude of the plastic damage to the large grillage structure is very large compared to the indenter's elastic deformation, therefore this elastic deformation is considered negligible. For this reason, the indenter was modeled as a rigid body. From an ideal standpoint, it should not matter whether the indenter was modeled using shell or solid elements because the indenter is rigid. In practice, a difference arises because of the algorithm used to identify contact between elements during the application of load. This contact algorithm is more prone to error for rigid shell elements than for rigid solid elements (ANSYS Inc. 2007a).

3.3.2 Element formulations

For the large grillage structure, an element formulation capable of predicting large structural deformations, plate bending, membrane effects, and shell thinning was required. Thirty-nine shell element formulations are available in Dyna for a broad range of analyses, but the default shell element formulation, the Belytschko-Tsay formulation, was most appropriate for this numerical model. The Belytschko-Tsay formulation implements the required structural phenomena: bending, membrane, and shell thickness changes; it employs reduced integration which means that the number of points for numerical integration of a shell element is less than that necessary for exact integration (ANSYS Inc. 2007a); it includes transverse shear; it has built in hourglass control; and it is the fastest of the explicit dynamics shell element formulations (ANSYS Inc. 2007a). The Belytschko-Tsay formulation is the recommended choice for most structural applications (LSTC 2007a).

Reduced integration is desirable for two reasons: it increases the speed of finite element calculations, and it alleviates *shear locking* which is a phenomenon common with 4-node (i.e. lower order) shell element meshes. Shear locking is an increase in structural stiffness (hence *locking*) that increases as finite element mesh size decreases. Reduced integration is a technique employed to eliminate shear locking, however, it has the drawback that it allows hourgassing to occur.

For the indenter model, the choice of element formulation is arbitrary. This is because the indenter was modeled as a rigid body. Elements are defined as rigid by their material model, not by their element formulation. Because the indenter elements are rigid, the element formulation has no effect on the numerical results and is therefore arbitrary. The default element formulation for solid elements is the “constant stress solid element” formulation – this element formulation was used.

3.3.3 Other shell parameters

Several other parameters besides the element formulation were required to properly define the shell elements. They are: the number of through-thickness integration points (NIPS); through thickness integration rule; the shear factor (SHRF); and element thickness.

3.3.3.1 Through thickness integration parameters

Through-thickness integration allows calculation of bending moments and in-plane forces in shell elements. Usually, at least two through-thickness integration points are required for elastic behaviour, and three or more for plastic behaviour (ANSYS Inc. 2007a). The strain distribution is always linear, but the stress distribution is more complicated as it depends on the material model.

Three options are available for through-thickness integration rules: trapezoidal, Gaussian quadrature, and a user-defined rule. The trapezoidal rule is not recommended for

accuracy reasons (LSTC 2007a). Gaussian quadrature is the default rule and it is possible for the user to choose the number of through-thickness integration points (NIPS) for the quadrature rule. The Gaussian quadrature rule was used for these numerical simulations.

Shell stress results are calculated for the outermost integration points, not at the element surface. This can lead to misinterpretation of the results. For elastic materials, the actual surface values can be extrapolated from the integration points because superposition holds. For nonlinear materials, the recommended procedure is to use four or five through-thickness integration points so that the difference in stress between the outermost integration point and the element surface is small (ANSYS Inc. 2007a). In this case, any discrepancies are ignored. For this study, five through-thickness integration points were used. The locations of the outermost integration points of Gaussian quadrature are given in Table 3-1.

Table 3-1: Gaussian quadrature through-thickness integration point coordinates.

Mid Plane	1 point	0
	2 points	± 0.5774
Outermost Point	3 points	± 0.7746
	4 points	± 0.8611
	5 points	± 0.9062
	Outer Surface	± 1.0000

3.3.4 Meshing

The geometric model was meshed entirely with quadrilateral (4-node) shell elements using the ANSYS® meshing tool. As mentioned in chapter 1.6.2, shell elements are generally the best choice with which to model structures constructed from steel. Quadrilateral shell elements were used in order to avoid the “locking” effect that triangular (3-node) elements can experience if the entire mesh is composed of 3-node elements (ANSYS Inc. 2007a). Further, triangular elements are simply degenerate quadrilateral elements where two of the four nodes composing the quadrilateral element are coincident, forming a triangular element. It is generally recommended that degenerate elements be avoided for nonlinear structural analyses because they are much less accurate and should not be used in regions of high stress gradient (ANSYS Inc. 2007b).

The geometric model was initially meshed with quadrilateral shell elements of an average size of 5 cm x 5 cm.

3.3.5 Model decomposition

A study was performed to determine the optimal decomposition of the finite element mesh. The parameters of the study were the “goodness” of the decomposition and the efficiency of running that decomposed model on the computer cluster. The goodness of the decomposition refers to the quality of the sections created during the decomposition. Factors influencing the goodness of the decomposition for this finite element mesh are the relative sizes of the sections and the sectioning of the contact surfaces.

The automatic RCB method was used to decompose the large grillage finite element mesh. An exhaustive examination of decompositions ranging from one to thirty sections was made. The decomposition was only good for 7, 13, and 25 sections, and the cluster ran most efficiently when using 25 processors. Therefore, the large grillage finite element mesh was decomposed into 25 sections. The results of the final decomposition using are shown in Figure 3-6.

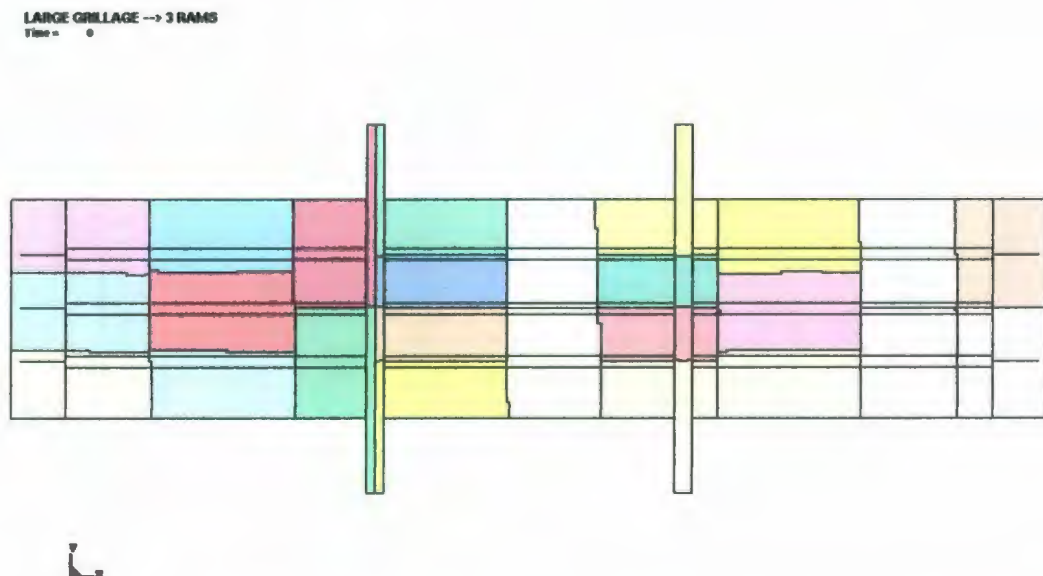


Figure 3-6: Plot of decomposed sections of a numerical model using the RCB method.

3.3.6 Mesh Conversion Study

As mentioned above, the geometric model was initially meshed with quadrilateral shell elements of an average size of 5 cm x 5 cm. However, simply meshing the geometry with an arbitrary mesh density is generally not adequate or appropriate when creating

numerical models. A mesh that has too few elements of too large a size (i.e. a coarse mesh) will not provide accurate results. A mesh that is too dense with elements that are too small (a very fine mesh) is not efficient. A mesh conversion study is required in order to determine an appropriate level of mesh density. A mesh conversion study involves solving a numerical model multiple times for ever-increasing mesh densities (a process known as refining the mesh). When plotted versus mesh density, the results of the numerical model should asymptote to a point where they do not change with increasing mesh density.

Four meshes of varying density were created for the large grillage numerical model – their details are given in Table 3-2.

Table 3-2: Mesh details for mesh conversion study.

Mesh	Number of Shell Elements	Number of Solid Elements	Mesh density [element/m ²]
1	8,986	384	475
2	80,874	3,840	4,279
3	727,866	19,440	38,511
4	30,902	3,840	1,635

Mesh 1 (Figure 3-7) represents the initial guess at an appropriate mesh density. Mesh 2 (Figure 3-8) has approximately 10 times the mesh density as mesh 1, and mesh 3 (Figure 3-9) has approximately 10 times the density of mesh 2 (or 100 times the density of mesh 1). Mesh 4 (Figure 3-10) is a hybrid of mesh 1 and mesh 2 with the greater mesh density concentrated between the transverse frames (i.e. the area in which the loading of the large

grillage structure took place). The indenter mesh density (i.e. solid element count) varies with shell element mesh density because the relative size of elements on both contact surfaces is important (Hallquist 2006). The master surface (i.e. the large grillage) mesh density should be less than the slave surface (i.e. the indenter) mesh density; otherwise the contact algorithm may allow some master nodes to penetrate the slave surface, unrestricted.

Mesh Conversion Study - Mesh 1

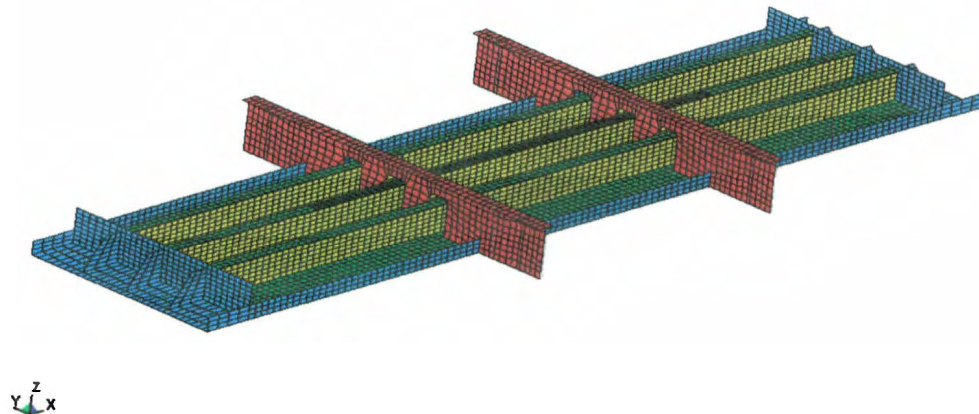


Figure 3-7: Mesh conversion study – mesh 1.

Mesh Conversion Study - Mesh 2

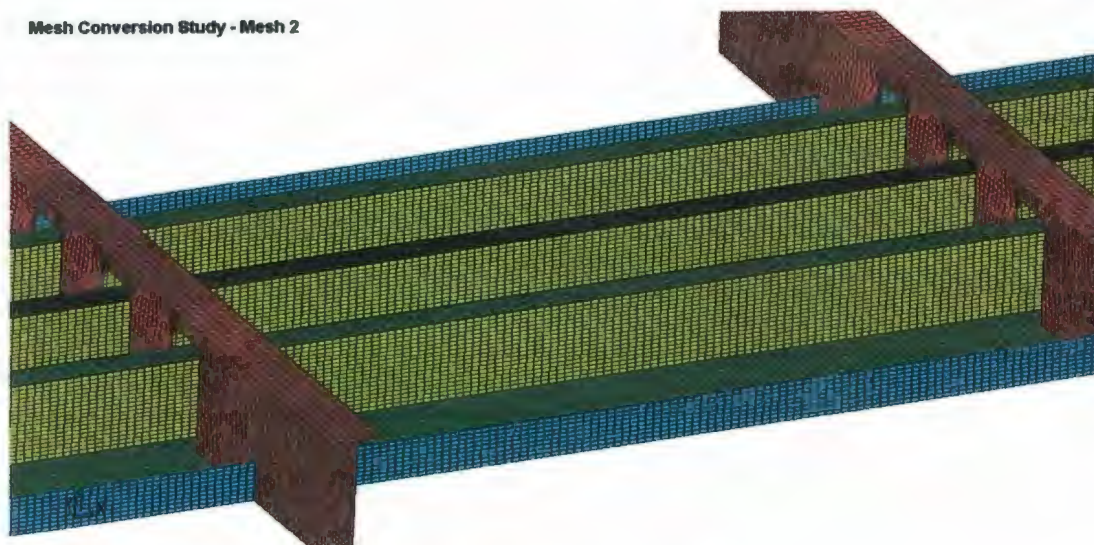


Figure 3-8: Mesh conversion study – mesh 2.



Figure 3-9: Mesh conversion study – mesh 3.

Mesh Conversion Study - Mesh 4

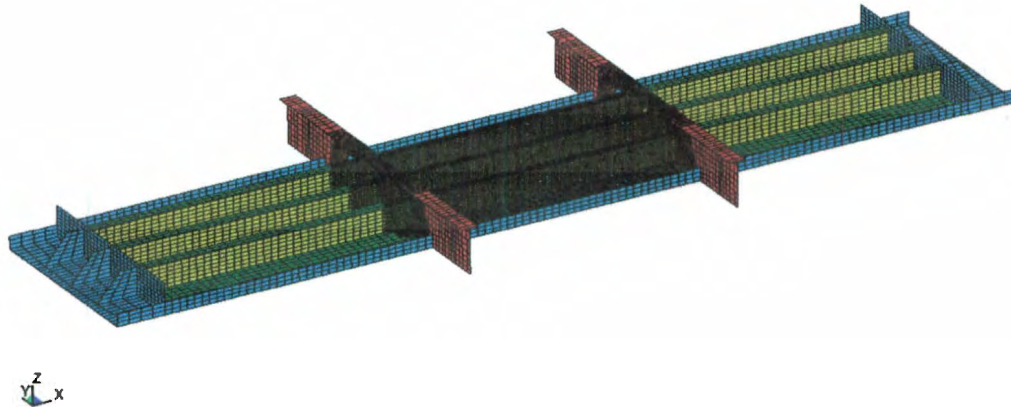


Figure 3-10: Mesh conversion study – mesh 4.

3.3.6.1 Load scenario

The same load scenario was applied to each of the four meshes at load patch 1 (load patch location shown in Figure 2-4). The load applied is similar to the loads discussed in section 3.13. Boundary conditions and contact definition were also similar to those presented below. Note: this study was performed as part of the design spiral of creating this numerical model, and hence its results should not be compared with the results of the final numerical model presented below.

3.3.6.2 Mesh comparisons

Structural response results for each mesh were compared on a one-to-one basis via plots. The structural response plotted is vertical load on the indenter. These plots are given

below in Figure 3-11 through Figure 3-15. It is obvious from Figure 3-14 that the mesh density for this numerical model converges for mesh 2. This is because the relationship between the results of mesh 2 and mesh 3 are almost perfectly one-to-one (i.e. nearly identical). After this discovery, an attempt to combine mesh 1 and mesh 2 was made in the hopes that a one-to-one relationship with mesh 2 results would be achieved. This was not the case as is shown in Figure 3-15. Mesh 2 was used throughout the rest of the research presented in this thesis.

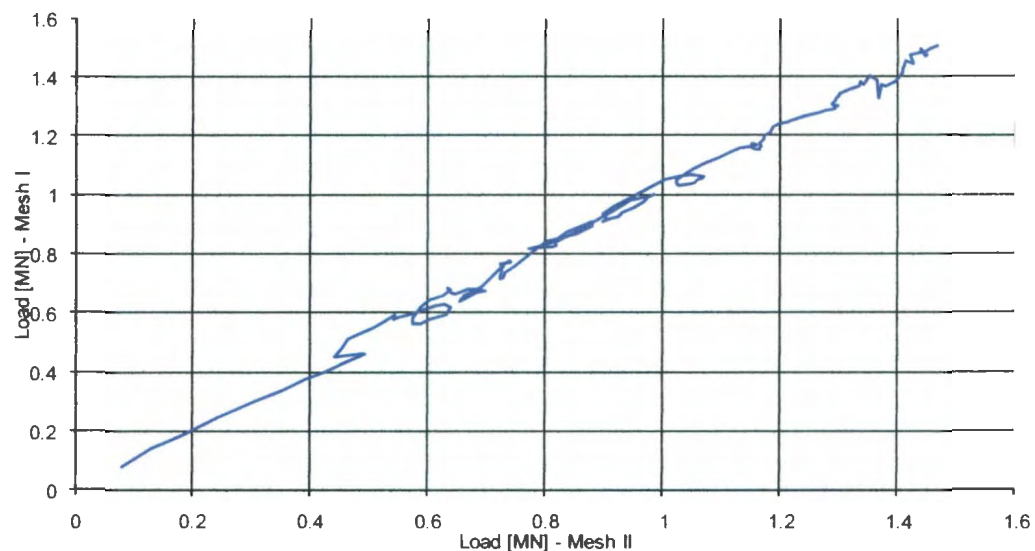


Figure 3-11: Mesh conversion study – comparison of Mesh 1 and Mesh 2 results.

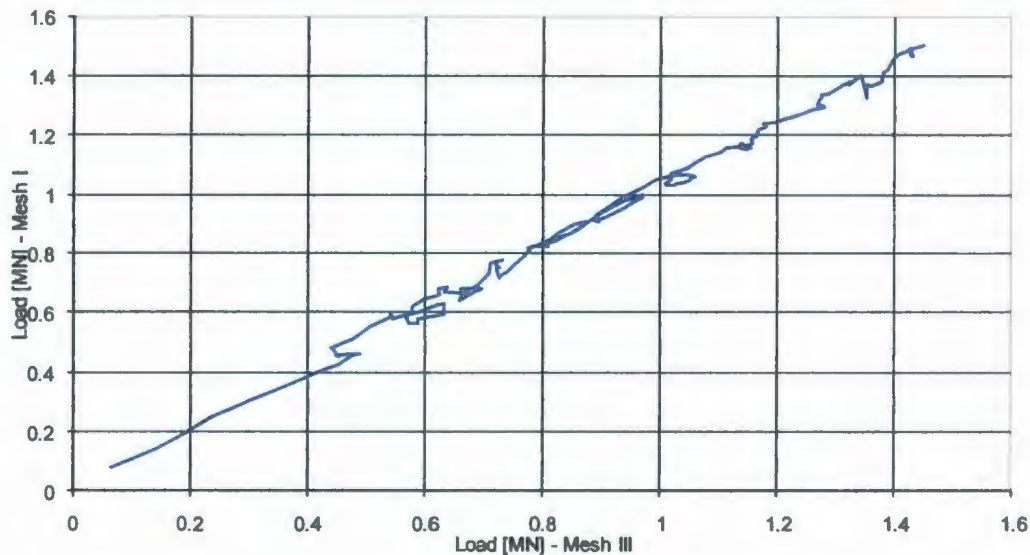


Figure 3-12: Mesh conversion study – comparison of Mesh 1 and Mesh 3 results.

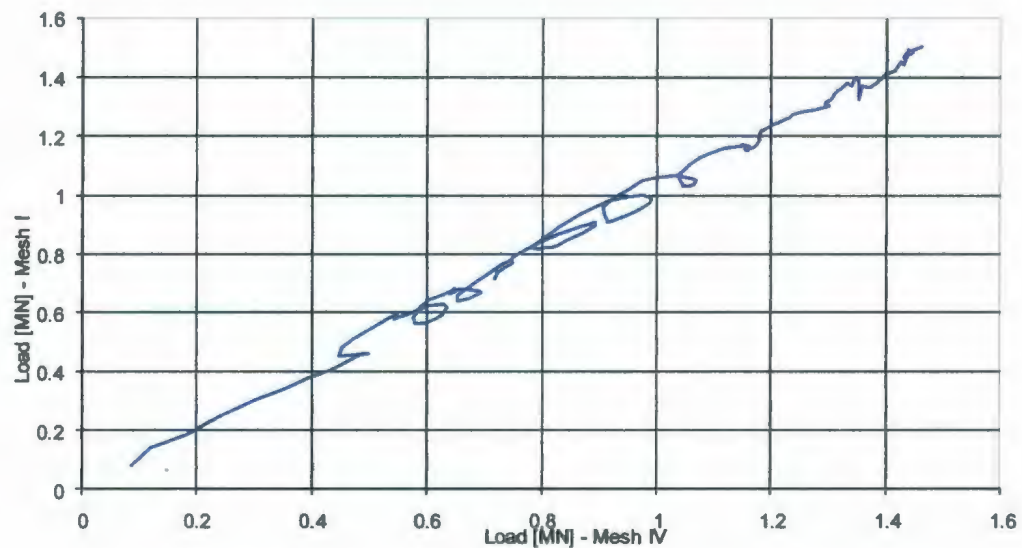


Figure 3-13: Mesh conversion study – comparison of Mesh 1 and Mesh 4 results.

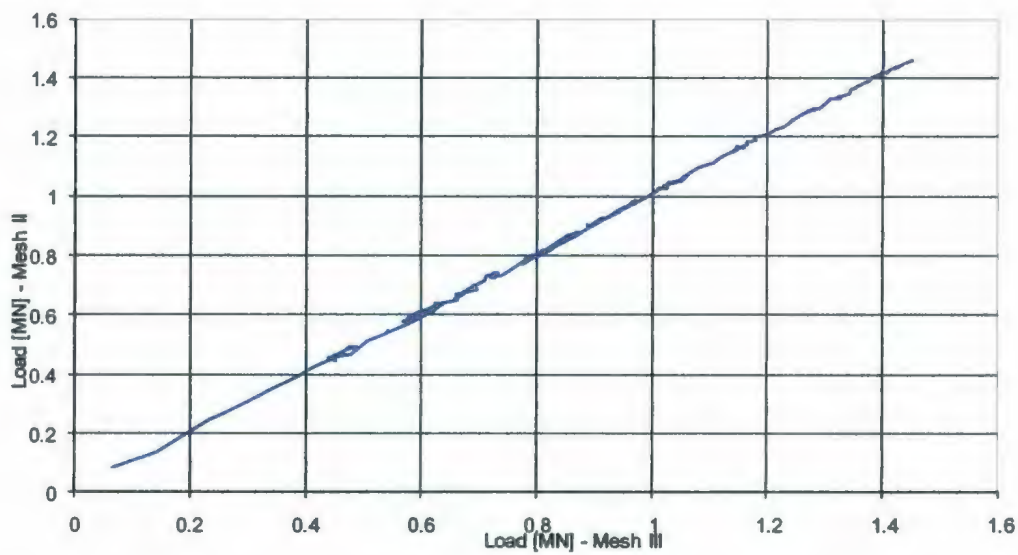


Figure 3-14: Mesh conversion study – comparison of Mesh 2 and Mesh 3 results.

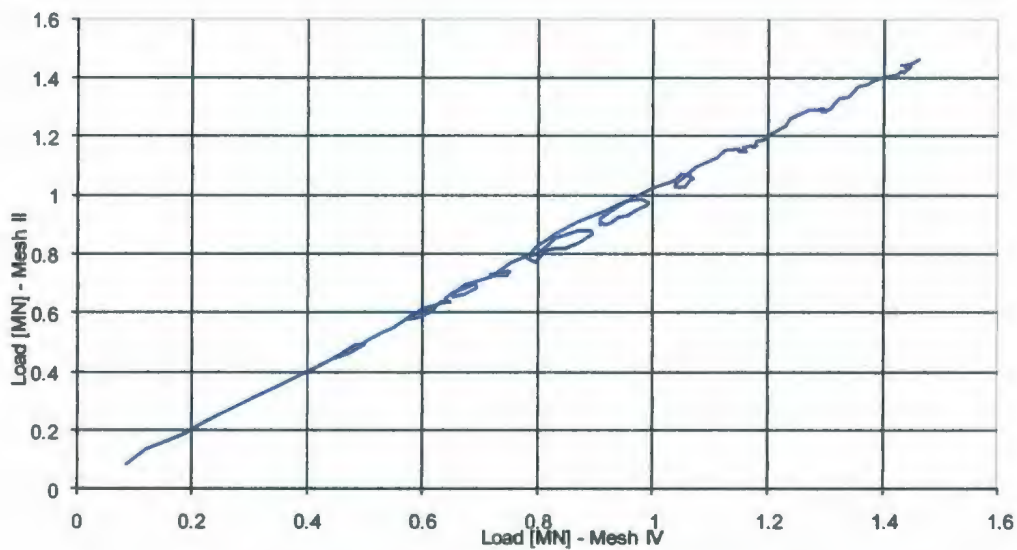


Figure 3-15: Mesh conversion study – comparison of Mesh 2 and Mesh 4 results.

3.4 Material Model

A material model is a material formulation together with its required inputs. A material formulation is similar in idea to an element formulation; that is, it defines the physics that will be included in a material model, and controls how those physics are implemented. Dyna has over 200 material formulations from which to choose.

Two material formulations were ultimately chosen and employed in this numerical model. They are MAT_PIECEWISE_LINEAR_PLASTICITY (Mat_24) (LSTC 2007b) and MAT_RIGID (Mat_20) (LSTC 2007b). Mat_24 was used to model the deformable large grillage structure and Mat_20 was used to model the rigid steel indenter used in the experiments outlined in Chapter 2.

Much time and energy was put into investigating the most appropriate material model with which to model the deformable large grillage structure. Many different material model formulations including Mat_3 – MAT_PLASTIC_KINEMATIC (LSTC 2007b) and Mat_105 – MAT_DAMAGE_2 (LSTC 2007b) were tested. Mat_3 is basically a simpler version of Mat_24, and Mat_105 is a continuum damage mechanics model which can be used to model necking in a tensile steel specimen. These material models were ultimately rejected in favour of Mat_24 because better results were achieved using that formulation (see section 3.13 for an explanation of desired results).

3.4.1 Mat_24

The proper name for Mat_24 is *Piecewise Linear Isotropic Plasticity Model*. It is an isotropic elasto-plastic material formulation. The term isotropic refers to the method of application of strain-hardening within the formulation. With isotropic strain-hardening, the centre of the yield surface is fixed and the radius is a function of plastic strain (Hallquist 2006). Elasto-plastic means that the material formulation is nonlinear and is capable of undergoing elastic (or completely reversible) deformation or plastic (permanent) deformation as required.

Using Mat_24, a user can define an arbitrary stress-strain relationship that is dependent on strain-rate. Stress-strain relationships may be defined by up to eight points directly within the formulation, or a more detailed curve may be defined that is called by the formulation. Several methods of including strain-rate effects also exist. It is possible to employ the Cowper-Symonds (Jones and Wierzbicki 1983) strain-rate model, a user-defined strain-rate model, or to implement several stress-strain curves based on different strain-rates with which the formulation will use and interpolate between as necessary.

The Cowper-Symonds model scales the yield stress by a factor of:

$$1 + \left(\frac{\dot{\epsilon}}{C}\right)^{\frac{1}{P}} \quad [3]$$

where: $\dot{\epsilon}$ is the strain-rate

C and P are the Cowper-Symonds strain-rate parameters

Mat_24 also has dedicated input for a bilinear material model (a bilinear stress-strain curve is shown in Figure 3-16) which requires only three inputs to define the stress-strain

relationship: Young's (elastic) modulus, yield stress, and tangent modulus. The tangent modulus is the slope of the second line in the bilinear model and it defines the rate of strain-hardening with strain. For a thorough description of Mat_24, please see Hallquist (2006).

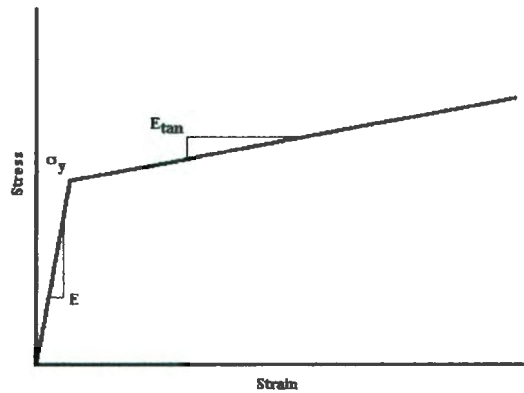


Figure 3-16: Bilinear stress-strain curve.

Much experimentation was done using the Mat_24 material formulation. Some of the experience gained from this experimentation is given below.

3.4.2 Mat_20

Mat_20 is a convenient way of turning a part into a rigid body. Rigid bodies are extremely efficient because rigid elements are bypassed in the element solving, and no storage is allocated for saving their history variables (Hallquist 2006). Inputs for Mat_20 include inertia properties, Young's Modulus, and Poisson's ratio. The latter two inputs

are used for determining sliding interface parameters for contact with other bodies.

Mat_20 was used for the indenter model.

3.4.3 Utilizing uniaxial tensile test data in numerical models

Much research exists regarding the utilization of uniaxial tensile tests results in numerical models. Paik (Paik 2007a) summarizes the common practices in this regard and presents a new method for accomplishing this effectively. These common practices and Paik's method for manipulating these test data are outlined below.

3.4.3.1 Method I

Method I is the traditional method used in finite element simulations. It involves using the following equations to transform an engineering stress-strain curve into a true stress-strain curve:

$$\sigma_t \approx \sigma_e(1 + \varepsilon_e) \quad [4]$$

and

$$\varepsilon_t \approx \ln(1 + \varepsilon_e) \quad [5]$$

where: σ_t is true stress

σ_e is engineering stress

ε_t is true strain

ε_e is engineering strain

Only points of the engineering stress-strain curve up to the ultimate stress are considered for this method. Method I is often not appropriate as it overestimates the strain-hardening characteristics and does not account for necking/softening beyond the ultimate stress.

3.4.3.2 Method II

Method II is identical to method I except all points on the engineering stress-strain up to the failure-strain are used in the transformation. Necking is modeled more accurately with this method; however, it overestimates the strain-hardening characteristics.

3.4.3.3 Method III (Paik's method)

Method III is a brand new approach proposed by Paik (2007a), called the “knock-down factor approach”. This approach was validated against tensile tests using steel coupons. Equation [4] and the following new equations are used to transform an engineering stress-strain curve to a true stress-strain curve:

$$\sigma_t \approx f(\varepsilon_e) \sigma_e (1 + \varepsilon_e) \quad [6]$$

where: $f(\varepsilon_e)$ is the “knock-down factor” function

and

$$f(\varepsilon_e) = \begin{cases} \frac{c_1 - 1}{\ln(1 + \varepsilon_u)} \{ \ln(1 + \varepsilon_e) \} + 1 & 0 < \varepsilon_e \leq \varepsilon_u \\ \frac{c_2 - c_1}{\ln(1 + \varepsilon_f) - \ln(1 + \varepsilon_u)} \{ \ln(1 + \varepsilon_e) \} + c_1 - \frac{(c_2 - c_1) \ln(1 + \varepsilon_u)}{\ln(1 + \varepsilon_f) - \ln(1 + \varepsilon_u)} & \varepsilon_u < \varepsilon_e \leq \varepsilon_f \end{cases} \quad [5]$$

where: ε_f is the engineering fracture strain

ε_u is the strain at the engineering ultimate stress

$$C_1 = 0.9$$

$$C_2 = 0.85$$

Method III modeled the necking and strain-hardening behaviour of the tensile tests very well (Paik 2007a).

3.4.4 Material Instability

It was quickly discovered that material models containing a negative slope in the stress-strain curve (i.e. strain softening) caused element deformations that grew without bound. Such a stress-strain curve, defined by 27 stress-strain point inputs, is given in Figure 3-17. Literature (specifically Chapter 6, section 7 of Belytschko, Liu, and Moran (2000)) suggested that a negative stress-strain slope for material formulations similar to Mat_24 (i.e. elasto-plastic formulations) caused this unstable deformation. To verify this theory, a simple numerical model of a plate was created with an entirely negative stress-strain curve for its material model (see Appendix C: Material Instability Test for specific details). A small perturbation to the centre of this plate caused unstable growth of the plate's deformation, thus confirming that material instability was the cause of the problem (see Hill (1962)).

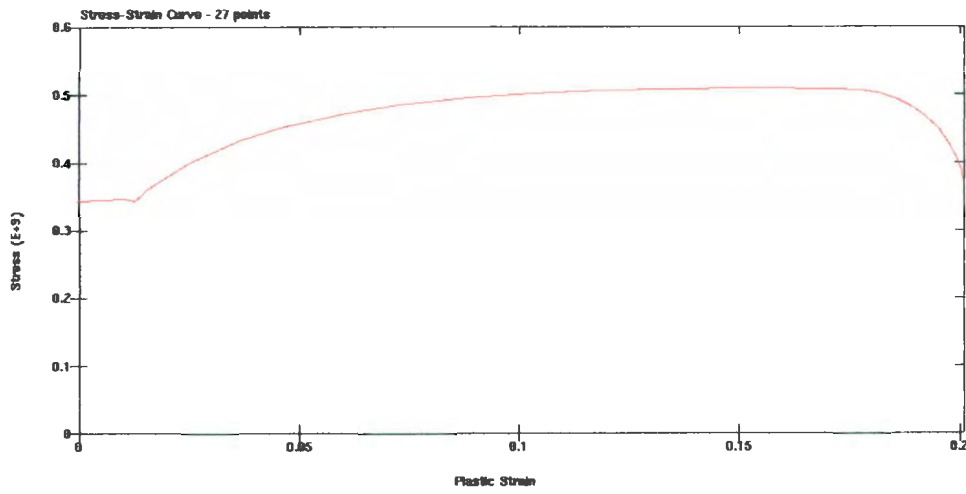


Figure 3-17: 27 point stress-strain curve with strain softening.

3.4.5 Stress-strain curve definition

Various degrees of stress-strain curve complexity were explored: a 17-point curve, a 10-point curve, a trilinear curve, and a bilinear curve. It may be seen in Figure 3-18 that shape of the actual stress-strain curve shown in Figure 2-16 is captured very well by the 17 and 10-point stress-strain curve definitions (which are shown plotted only up to the ultimate stress). The trilinear curve was an attempt to include the stress plateau (the flattened area of a stress-strain curve just after the elastic portion) in a “bilinear type” model. The bilinear curve is a standard bilinear model which requires input of only the Young’s modulus, yield stress, and tangent modulus. A tangent modulus of 1.0 GPa was found to work well and provided a realistic ultimate strength for the failure-strain (shown by green line in Figure 3-18). The reader is referred to Kozarski (2005) for a detailed treatment of the bilinear stress-strain model.

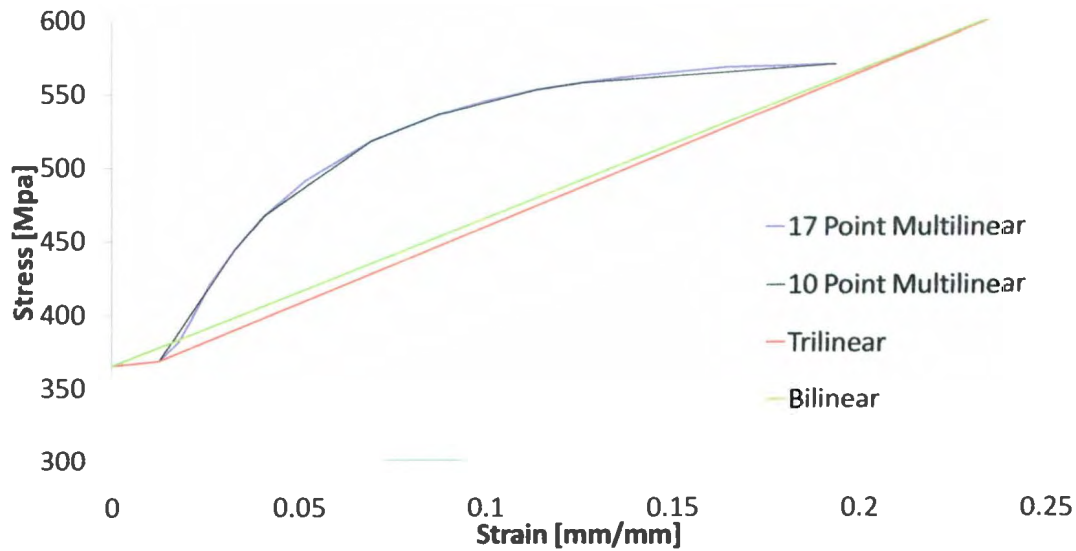


Figure 3-18: Stress-strain curves of varying complexity.

Results for each of these stress-strain curves are presented in Figure 3-19, along with the load-displacement curve from the large grillage experiments for load-patch 1. This experimental load was the load applied to the numerical model for these tests. It is apparent from this figure that the bilinear material model (green line labelled line “B” in the Figure 3-19) best matches the experimental load-displacement curve.

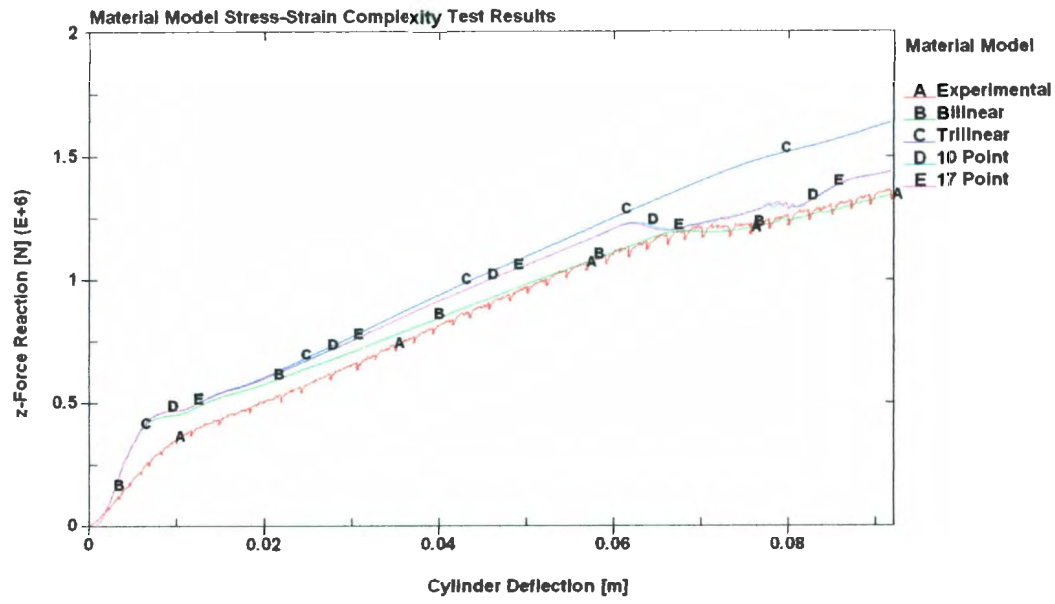


Figure 3-19: Load-displacement curve results for various material model inputs.

3.4.6 Material model for each component

The large grillage is composed of five components (described in 2.2.1 and 3.6). A uniaxial tensile test was conducted for each of the five components. It was theorized that assigning separate material models to each component, based on their uniaxial tensile test results, would improve the overall accuracy of the numerical model. The parameters for each material model based on these tensile tests, and modified using Paik's method (outlined in 3.4.3.3), are given in Table 3-3. Load-displacement results for both the multiple material models and the single bilinear material model are given in Figure 3-20, along with the experimental results. As in 3.4.5, the single bilinear material model gave the best results.

Table 3-3: Material model (Paik's Method) parameters for five components.

Transverse Frame 18mm Steel (Specimen 1) - Bilinear				
Density [kg/m ³]	E [Pa]	Poisson's Ratio	Yield Stress [Pa]	Etan [Pa]
7850	1.84E+11	0.3	3.48E+08	1.00E+09
Boundary Structure 30mm Steel (Specimen 4) - Bilinear				
Density [kg/m ³]	E [Pa]	Poisson's Ratio	Yield Stress [Pa]	Etan [Pa]
7850	2.31E+11	0.3	4.26E+08	1.20E+09
Plate 10mm Steel (Specimen 2) - Bilinear				
Density [kg/m ³]	E [Pa]	Poisson's Ratio	Yield Stress [Pa]	Etan [Pa]
7850	2.15E+11	0.3	4.21E+08	1.07E+09
Long Stiffener Web 9mm Steel (Specimen 3) - Bilinear				
Density [kg/m ³]	E [Pa]	Poisson's Ratio	Yield Stress [Pa]	Etan [Pa]
7850	2.19E+11	0.3	3.77E+08	9.96E+08
Long Stiffener Flange 10mm Steel (Specimen 5) - Bilinear				
Density [kg/m ³]	E [Pa]	Poisson's Ratio	Yield Stress [Pa]	Etan [Pa]
7850	2.30E+11	0.3	3.48E+08	1.14E+09

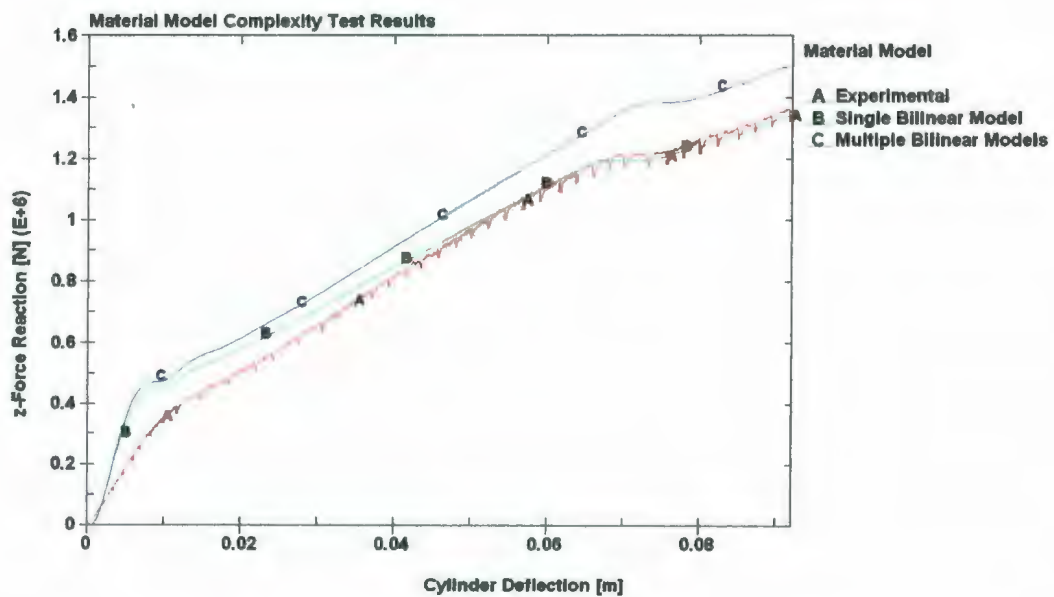


Figure 3-20: Load-displacement curve results for multiple and single material models.

3.4.7 Final material models

For the large grillage model, the research outlined in this section ultimately suggested that a single bilinear material model implemented using Mat_24 and employing Paik's method III, provided the best comparison with experimental results. The inputs for this material model are given in Table 3-4.

Table 3-4: Large Grillage material model parameters.

Large Grillage Material Model - Mat_24				
Density [kg/m ³]	E [Pa]	Poisson's Ratio	Yield Stress [Pa]	Etan [Pa]
7850	2.00E+11	0.3	3.50E+08	1.00E+09

For the indenter model, Mat_20 was used to define it as rigid. Inputs for Mat_20 were identical to those given in Table 3-4 where appropriate.

3.5 Boundary Conditions

The boundary conditions for this model come from two main sources: experimental model supports, and contact. The latter will be discussed in detail in section 3.7.

The large grillage model is supported by the test frame as discussed in section 2.3. The test frame was not expected to plastically deform during the large grillage experiments and therefore, because the plastic deformation of the large grillage structure is so large, any elastic deformation of the test frame is considered negligible. Hence, the boundary conditions applied to the large grillage model during the experiments were effectively

applied via the bolts used to attach the structure to the test frame. It is assumed the position of these bolts is fixed.

The bolt patterns (see black areas in Figure 3-21) used to attach the large grillage structure to the test frame during the physical experiments were such that rotations and displacements in all degrees of freedom for the structure were fixed. The final mesh of the large grillage finite element structure was such that nine nodes occupied the approximate size and position of each bolt for the transverse frames, and six nodes for each bolt for the 30 mm boundary structure (on the longitudinal ends). These "bolt nodes" were fixed against rotational and translation in all degrees of freedom.

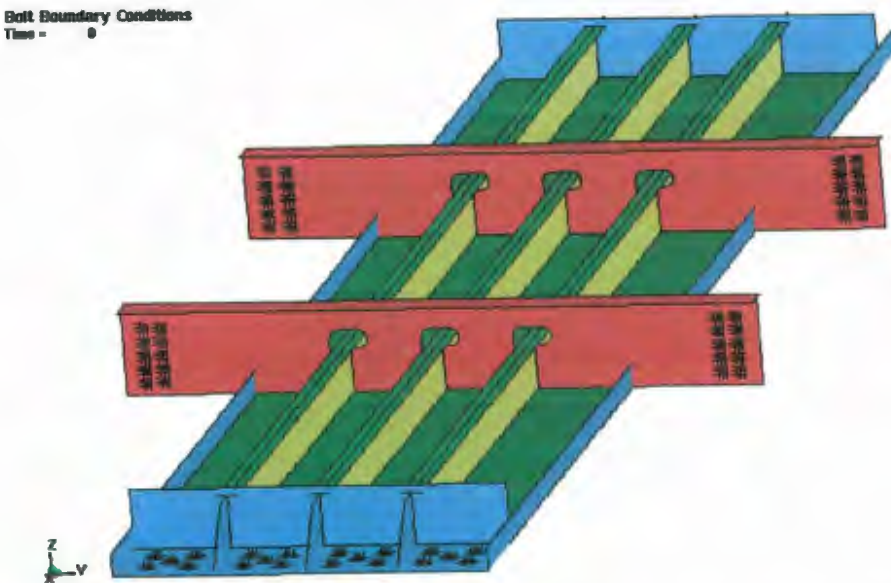


Figure 3-21: Fixed nodes (shown in black) used to model bolted boundary conditions.

3.6 Part Definition

As mentioned in Chapter 2, Section 2.2.1, the major components of the large grillage structure are: the transverse frames (top left of Figure 3-22); the boundary structure (bottom left of Figure 3-22); the hull plating (top right of Figure 3-22); and the longitudinal stiffener webs and the longitudinal stiffener flanges (both shown in bottom right of Figure 3-22). Dyna applies element parameters and material models to elements by collecting them into groups called *parts*.

Ideally, each large grillage component has uniform steel thickness and material properties. Also, elements used to model the components would likewise have homogenous parameters. Therefore, it was convenient to define the numerical *parts* to be equivalent to the large grillage components.

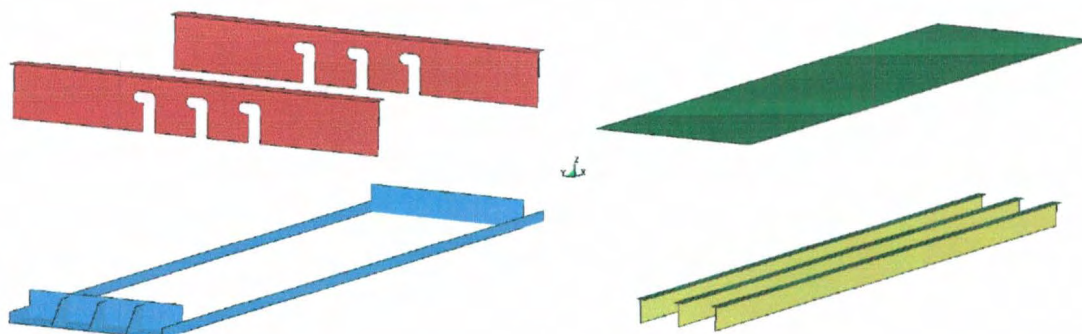


Figure 3-22: Large grillage model “parts”.

In addition to these parts, a rigid indenter part was defined. It is shown in Figure 3-23.

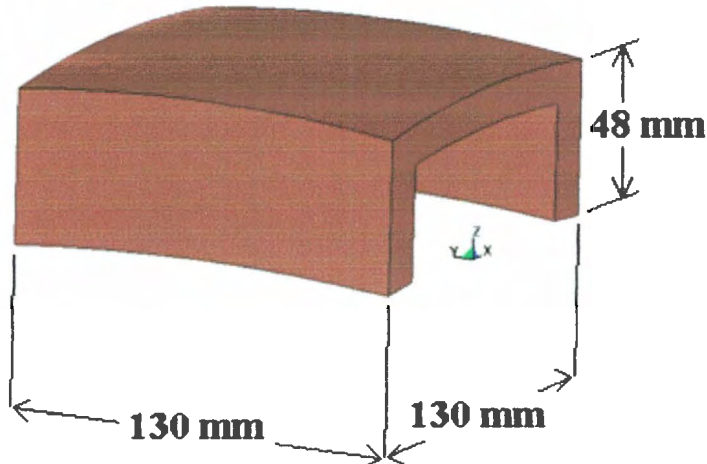


Figure 3-23: Rigid indenter “part”.

3.7 Contact

Implementation of a contact algorithm in these simulations was necessary to allow the large grillage structure to interact with the indenter model. Contact algorithms have been included in Dyna since at least 1976 and their implementations are based on three basic contact methods: the kinematic constraint method (Hallquist 1976), the penalty method, and the distributed parameter method (Hallquist 1978). The penalty method is possibly the most-general and most-used contact algorithm (Hallquist 2006), and will be discussed in detail below.

Regardless of the contact algorithm used, Dyna defines contact interfaces in three dimensions by listing all triangular and quadrilateral segments that make up each side of

the interface (Hallquist 2006). Interface surfaces are differentiated by labelling one side the *master* surface and the other the *slave* surface. Upon contact between the master and slave surfaces, nodes on the slave surface are constrained to slide on the master surface until a tensile force occurs, at which time the surfaces may separate.

3.7.1 Penalty method

In contrast to the kinematic constraint method where slave nodes are not allowed to pass through the master surface (problems arise if this happens), the penalty method expressly makes use of slave node penetration into the master surface. The penalty method consists of identifying the slave nodes that penetrate the master surface and placing discrete springs normal to the surface between the master surface and slave nodes (Hallquist 2006). A given spring exerts a force on its slave node that is proportional to the slave node's penetration through the master surface (Hallquist 2006). Each spring's modulus is unique and depends on the bulk moduli of the slave and master surfaces. Drastic differences in material bulk moduli at the interface can cause problems and several algorithms are available to address these issues; however, for these simulations, both the large grillage structure and the indenter are composed of similar steel; negating the need to employ other than the standard algorithm. Because of this, the standard algorithm provides spring moduli approximately equal to the material moduli at the contact interface. An added benefit of having approximately equal spring and material moduli is that the explicit time step is not affected by the contact algorithm (Hallquist 2006).

Further explanation of the penalty method is necessary. The time steps of explicit structural simulations are sufficiently small (on the order of 10^{-7} seconds for these simulations) such that the slave node penetration for each time step is also small. During a single time step, the relative position of the slave and master surfaces are calculated without considering contact between them. The contact algorithm is then employed (Belytschko, Liu, and Moran 2000) and if a contact interface is found, slave nodes that penetrate the master surface are “pushed” back to the surface by a force equal to the nodal penetration times the interface spring modulus.

Some of the major benefits of using the penalty method include: little to no excitement of hourgassing; exact conservation of momentum without imposing impact and release conditions; and no special treatment of intersecting interfaces is required (Hallquist 2006).

3.7.2 Shell element thickness

Shell element thickness is accounted for in the contact algorithm. Because the “hull plating” is 10 mm thick, with the shell element through thickness centre having 5 mm of thickness on either side, then anything contacting the “hull plating” will actually contact “nothing” 5 mm below the element.

3.8 Loading

Several methods of applying loads were investigated. Forces applied to nodes, and pressures applied to elements (on an area equal in size to that of the experimental indenter) were the two methods first attempted. These methods resulted in the hull plating expanding like a balloon (high membrane forces) around the longitudinal stiffener web, while the web remained comparatively unloaded. Next, direct displacement of the nodes (coinciding with the size and position of the indenter) was tried. This proved much better for loading the structure than the first method (force/pressure), but tended to stretch the surrounding finite element mesh unnaturally because elements that would normally be moving perpendicular to the load direction were instead being restrained. Finally, a separate finite element mesh for the indenter was created, and loads were applied to the grillage structure by displacing the indenter and defining contact between the grillage model and the indenter. This method allowed the hull plating to be displaced by the indenter (as in the experiments), while not unduly restricting any nodal degrees of freedom.

3.9 Damping

Tests of the numerical model during its development revealed that structural oscillations were evident in the 120-150 Hz range. These oscillations were an artefact of the loading method chosen. Several methods of removing these oscillations were attempted. The most effective method was to employ 20% critical damping to the structure over the 120-150 Hz range using the DAMPING_FREQUENCY_RANGE card. Sensitivity tests were

conducted regarding the level of critical damping, and it was subsequently found that 20% was the most appropriate level.

3.10 Solution Controls

Solution controls define how the finite element code solves the numerical problem, and which results to record. For this numerical model, four solution controls were utilized: energy, shell, termination, and timestep.

The “energy” control defines the types of energies computed and included in the energy balance. For these simulations, all types of energy were included; they are: hourglass energy, Stonewall energy (default), sliding interface energy (default if contact is employed), and Rayleigh energy (damping energy).

The “shell” control defines how shell elements respond during the numerical simulation. The salient options utilized in these simulations are ISTUPD and THEORY. ISTUPD controls the shell thickness changes. A value of 1 was chosen for ISTUPD, which implies that shell element thickness will change as a function of membrane stress. THEORY controls the element formulation for all shells. A value of 2 was input implying that the Belytschko-Tsay formulation was to be used.

The “termination” control defines the point in *simulation time* that the simulation of the problem terminates. This value changes depending on the *simulation time* required by each simulation.

The “timestep” control defines the “computed timestep scale factor”, and allows for “mass scaling” which overrides the computed timestep in favour of a user-defined one. Mass scaling is useful for quasi-static simulations because it can reduce the amount of time required to solve a simulation (i.e. the *run time*). Mass scaling was not used in this numerical model because minimization of *run time* was not an issue. The computed timestep scale factor was unchanged from the default value of 0.9. This is essentially a safety factor, in that it decreases the computed timestep such that the numerical simulation remains stable. Values lower than 0.9 were tested, but gave no appreciable change in results.

3.11 Results Declaration

Results are recorded in Dyna via two databases: an ASCII database and a binary database (also known as the *dyna database*). The output frequency (i.e. the amount of *simulation time* between output of results) may be specified separately for each database. Results from the ASCII database may be plotted versus time, or cross-plotted against other results. The *dyna database* may also be plotted thus; however, it also contains information that may be plotted in fringe plots overlaying the elements in the numerical model. Two examples of this are structural deformations and stresses. The finite element

mesh may be plotted in a deformed state with stresses caused by the deformation (see Figure 3-24).

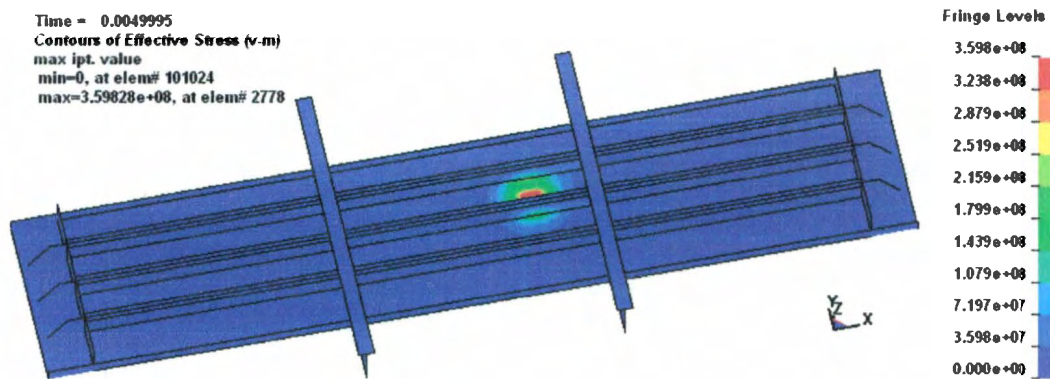


Figure 3-24: Plot of deformed structure overlaid with von Mises stress fringe plot.

3.12 Modifications from Trial-and-Error

As mentioned above, creation of this numerical model is a design spiral process. This means that the process is not linear such that one step flows seamlessly into the next. Continual testing and modification of the numerical model was necessary in order to bring it to a level in which confidence in the results are high.

3.12.1 Hourgassing

Hourgassing was observed for mesh 2 along the central longitudinal stiffener above the loaded area. The hourgassing problem was resolved by increasing the mesh density along the central longitudinal stiffener flange for its entire length between the transverse

stiffeners and for a short distance to either side of them. This mesh refinement is shown in Figure 3-25.

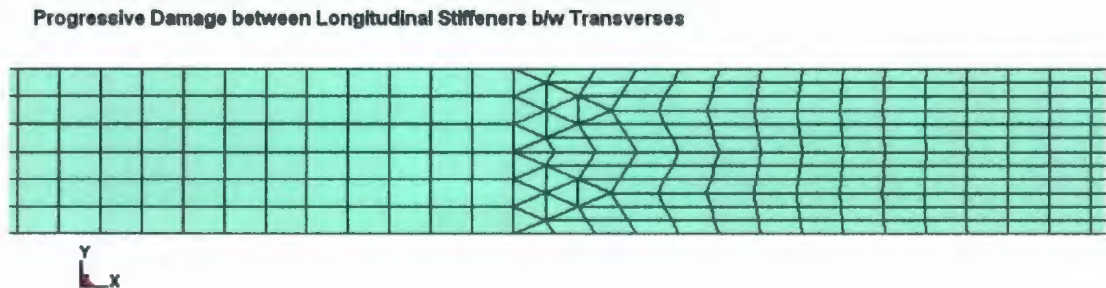


Figure 3-25: Refinement of central longitudinal stiffener flange near transverse stiffener.

3.13 Model Validation

The numerical model outlined above was validated against the results of the experiments presented in Chapter 2. The load applied to the numerical model for validation purposes was identical to that applied to load patch 1 in the experiments. The model was considered validated when the load-displacement curves for both the experiments and the numerical model were within acceptable agreement.

3.13.1 Load

During the experiments, the hull plating at load patch 1 (see Figure 2-4) was displaced 92 mm from its original position, in a direction normal to the hull plating. This displacement was imposed using a hydraulic ram that was pushing a steel indenter into the hull plating. This displacement-load was applied in small quasi-static increments as described above.

A similar load was applied to the deformable large grillage numerical model using the rigid indenter model – the details of both are described above. Instead of applying the load in small increments, as in the experiments, the load was applied at a constant rate of indentation from 0 to 92 mm. Since time-dependant phenomena (e.g. material strain-rate and sliding friction) were not included in this numerical model, the choice of indentation rate depended only on ensuring that enough timesteps were included in the *simulation time* that the structural reaction to the load was properly modeled. Indentation rates that equated to simulation-times of 0.001, 0.1, and 1 second were tried. The results for 0.1 and 1 second were identical; indicating that 0.1 seconds was a sufficient period of *simulation time* in which to apply the 92 mm displacement.

3.13.2 Results

The results of the numerical model validation are given in the form of load-displacement curves. The numerical model was considered validated when the structural reaction force versus indenter displacement curves matched as closely as possible. Figure 3-26 shows these results. It is obvious from this figure that the numerical model overestimates the structural response to smaller displacement-loads; however, the response is very good for higher displacement-loads. Much effort was put into modifying the numerical model so that the lower response was more accurate; however, in all cases this caused the upper response to worsen dramatically. It was decided to continue with the numerical model that provided the results shown below as the best compromise. The discrepancy at the lower indentation levels is most likely because the steel test frame on which the large

grillage structure was mounted (the purple structure in Figure 2-1) during the physical experiments was not numerically modeled. If included in the numerical model, the test frame would most likely have absorbed a considerable amount of energy during the lower (linear) portion of the load-displacement curve. Including the test frame in the numerical model would most likely have lowered the reaction force felt by the indenter and provided closer agreement with the experimental results. Note that it is also possible that there was some “settling” of the large grillage structure during the initial experimental loading (akin to the “slipping in the grips” associated with material tensile tests). This settling would also serve to reduce the initial reaction load.

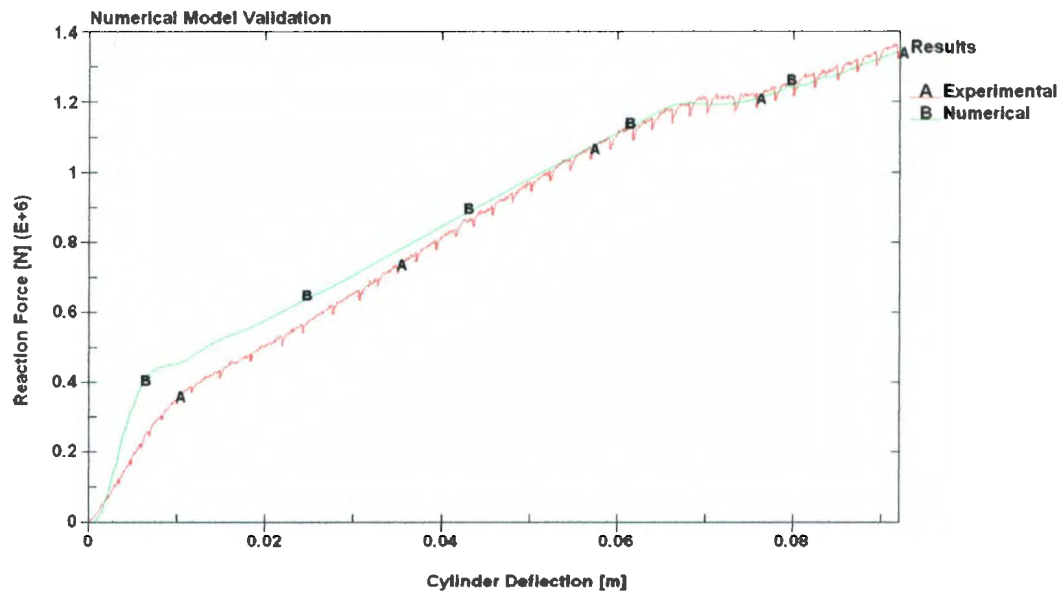


Figure 3-26: Comparison of experimental and numerical model results.

3.14 Numerical Model Summary

This section summarizes the inputs used to define the numerical model.

3.14.1 Finite element mesh

Mesh 2, with the re-meshed central longitudinal stiffener flange was chosen as the final mesh.

3.14.2 Material model

A single bilinear material model implemented using Mat_24 was used for the large grillage structure. The inputs for this material model were given in Table 3-4 and are repeated here in Table 3-5

Table 3-5: Large Grillage material model parameters.

Large Grillage Material Model - Mat_24				
Density [kg/m ³]	E [Pa]	Poisson's Ratio	Yield Stress [Pa]	Etan [Pa]
7850	2.00E+11	0.3	3.50E+08	1.00E+09

Mat_20 was used to define the indenter model as rigid. Inputs for Mat_20 are identical to those given in Table 3-5 where appropriate.

3.14.3 Boundary conditions

Constraints were applied using “single point constraints”, to a set of nodes located at the positions of the bolts for the large grillage experimental model. All six degrees of freedom were fixed.

3.14.4 Part definition

Six parts were defined: transverse frames, boundary structure, hull plating, longitudinal stiffener webs, longitudinal stiffener flanges, and the indenter. Two inputs were required for part definitions: “section” and “material model”. The section refers to a card containing the element parameters. These cards are defined in 3.14.1. The material model for all parts except the indenter was Mat_24. The material model for the indenter was Mat_20.

3.14.5 Contact definition

An automatic surface to surface (ASTS) contact definition was applied to a master part set containing all the deformable parts (i.e. the entire large grillage model) and a slave part id which was the rigid indenter. The master elements considered by the contact algorithm were limited to those within a user defined box; the dimensions of which depended on the path of the rigid indenter. The Coulomb friction model and contact damping were not employed. All other values input were default values.

3.14.6 Load definition

Loads were defined using BOUNDARY_DESCRIBED_MOTION_RIGID cards which apply translational or rotational motion (as well as their time derivatives – velocity and acceleration) to a rigid part; in this case the rigid indenter. Motions were input by using DEFINE_CURVE cards to define translational motions versus time.

3.14.7 Damping definition

Damping was employed using the DAMPING_FREQUENCY_RANGE card. 20% critical damping over a frequency range of 120-150 Hz applied to the large grillage structure.

3.14.8 Solution control parameters

All energies were computed and included in the energy balance using the CONTROL_ENERGY card. Shell thickness change with membrane stretching was included using the CONTROL_SHELL card (ISTUPD-1). Further, the Belytschko-Tsay element formulation was used. The “computed timestep scale factor” was left at the default value of 0.9.

3.14.9 Results declaration

ASCII files containing results outputs for 4×10^{-4} seconds of simulation-time were recorded; they are:

- Boundary condition (BNDOUT) forces and energy
- Global statistics (GLSTAT AND GLSTAT_MASS_PROPERTIES) including mass and inertial properties
- Material energies (MATSUM)
- Nodal (NODOUT) displacement, velocity, and acceleration data for top central indenter node
- Rigid body data (RBDOUT)
- Resultant interface forces (RCFORC)
- Sliding interface energies (SLEOUT)
- Single point constraint reaction forces (SPCFORC)

Dyna database results were output for every 5×10^{-3} seconds of simulation-time. These results include:

- Geometric deformations
- Results output for top, mid, and bottom integration points
- Stress and strain tensors
- Effective plastic strain
- Stress resultants
- Internal energy and thickness
- Shell hourglass energy
- Material energy

4 PROGRESSIVE DAMAGE TESTS AND RESULTS

This chapter describes the investigation of the structural capacity and reaction of an IACS ice-strengthened large grillage model to various progressive damage scenarios. It is expected that these load scenarios would coincide with scenarios considered during the design of an IACS ice-strengthened ship. This investigation was carried out using the nonlinear explicit numerical model described in Chapter 3.

4.1 Notes on Loading, Analysis, and Results

Progressive damage causes nonlinear stress-strain behaviour; therefore, the method of load application is important because the principle of superposition does not hold. The method of load application used for this investigation consists of three separate actions: first, the indenter is pushed into the hull plating (z-direction motion only); next, the indenter is dragged laterally (x- and/or y-directions only); and third, the indenter is pulled out of the hull plating (again in the z-direction only). Henceforth, the first loading action may be referred to as the *static load*, the second may be referred to as the *dynamic load*, and the third action may be referred to as *unloading*. This loading method was chosen because it is the simplest method with which to apply progressive damage. Each change in the indenter's motion is isolated, enabling observation of its effects on the structure. Examples of several load-history curves resulting from the application of this loading method are given in Figure 4-1. It was generally observed that the structural capacity of the large grillage model was lower for the dynamic load than for the static load. The initial part of a curve (denoted by a green "S" in the figure) shows the structural reaction

to the static load. The second part of a curve (denoted by a red “D” in the figure) shows the structural reaction to the dynamic load. The third part of a curve shows the structural reaction during unloading. For brevity, the unloading section is not denoted in the figure, but it follows the dynamic load.

The final value of the static load part of a curve is the large grillage’s *static structural capacity* at the start location of the dynamic load. This value represents the structure’s reaction to a simple z-direction indentation at this location. Any value along the dynamic load part of a curve may be referred to as the *dynamic structural capacity*. This value represents the structure’s reaction to a z-direction indentation that has caused previous damage at other locations throughout the structure. Each progressive damage scenario presented in this chapter has been designed such that the dynamic load stops at a lateral location that is symmetrically opposite from that of its start location. Further, the large grillage structure is itself a symmetric structure. Because both the structure, and the start and finish locations of the dynamic load are symmetric, a direct comparison between the static structural capacity and the dynamic structural capacity may be made for these locations. Further, static indentations for various other lateral locations were carried out. These locations were chosen to be in the path of the dynamic loads for the various progressive damage scenarios described in this chapter. Knowledge of the static structural reactions at these locations enabled further comparison between the structure’s static and dynamic structural capacities.

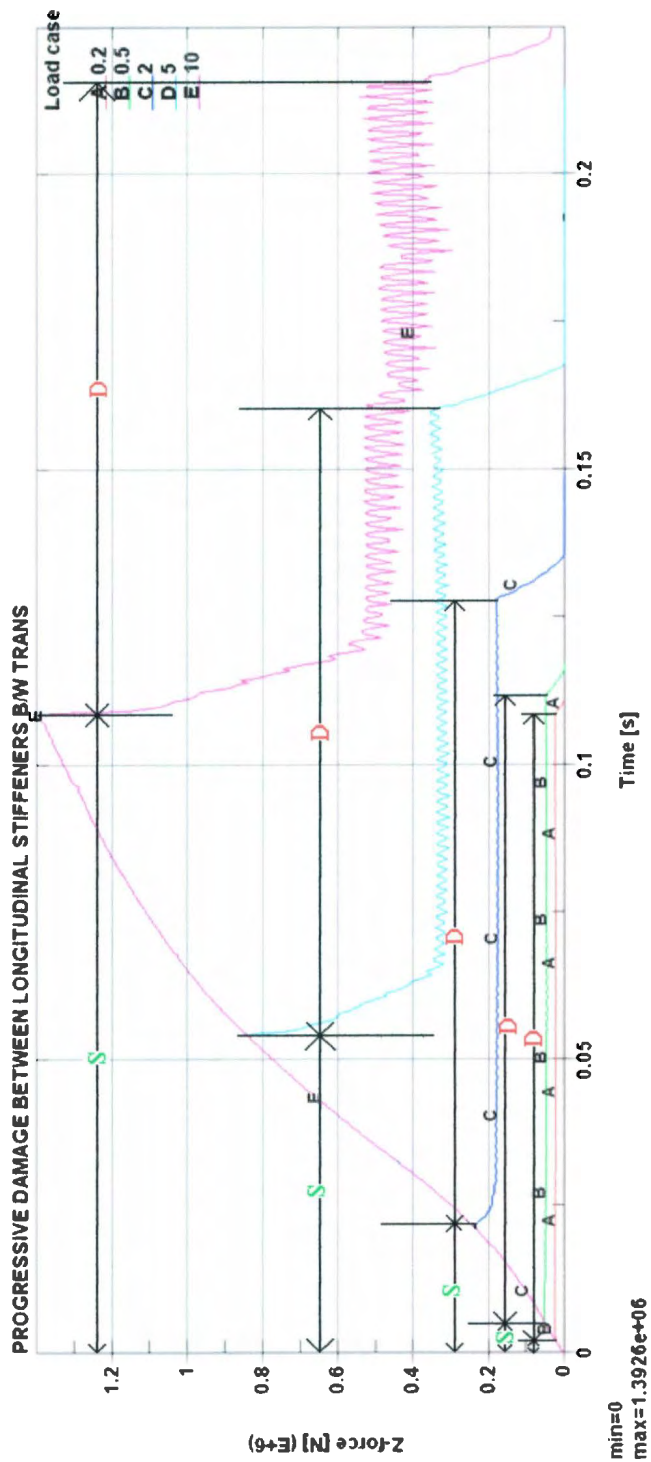


Figure 4-1: Example load history curve showing static (green "S") and dynamic (red "D") loads.

Note that loads are applied by imposing displacements on the indenter (as outlined in chapter 3.8). The indenter's velocity during the static load and the unloading was the same for all simulations conducted for this thesis – as was the indenter's lateral velocity (although not equal to its z-velocity). The family of load curves presented in Figure 4-1 have dynamic sections that all take the same length of time, indicating that the lateral distance travelled by the indenter was the same in each. The static load sections all take different amounts of time, indicating that the level of indentation was different for each case.

Eight progressive damage load scenarios were considered in this chapter. These eight load scenarios may be broken into three categories: progressive damage between transverses, progressive damage across multiple transverses, and progressive damage parallel to transverses. Several *load scenarios* within each category were considered; they are given in Table 4-1.

Table 4-1: Progressive damage load scenarios.

Category	Scenario
Between Transverses	Between Longitudinals
	Along Longitudinal
	Diagonally Across Longitudinals
Across Transverses	Between Longitudinals
	Along Longitudinal
	Diagonally Across Longitudinals
Perpendicular to Transverses	Between Transverses
	Along Transverse

For each load scenario, five *load cases* were simulated. The dynamic load was the same for each load case, but the static loads were not. These static loads were equal to $0.1\%L$, $0.25\%L$, $1\%L$, $2.5\%L$, and $5\%L$; where L is the transverse frame spacing of an “IACS polar class” ship. For these simulations, the transverse frame spacing of the large grillage structure described in Chapter 2.2 was used. This frame spacing is $L=2000$ mm; therefore the applied static loads were: 0.2, 0.5, 2.0, 5.0, and 10.0 cm. Each load case is referred to in this thesis by its static load value. Given that there are eight load scenarios with five load cases per scenario, 40 progressive damage simulations were performed.

Material failure was not modeled in these simulations, and therefore the finite elements could strain to infinity. For this reason the results for the 10 cm load cases (and sometimes the 5 cm load cases, as outlined below) should not be viewed as predicting the actual behaviour or structural capacity of the structure. In all likelihood, the large grillage structure would fail under these extreme load conditions (as explained below where applicable). The 10 cm load cases were performed in order to obtain an exaggerated view of the phenomena occurring during lower load cases.

The results of each simulation are given in the form of load-displacement plots, and various other figures. Unless otherwise stated, all load-displacement curves report the structure’s reaction force in the z-direction versus the resultant lateral displacement of the indenter. That is, the force pushing the indenter out of the structure compared to the indenter’s motion in the plane of the hull plating. Note that these “load versus lateral displacement” curves show that the z-force reaction does not start from zero at zero

displacement. This is true because the static load (i.e. z-direction loading) has already occurred before any lateral indenter motion takes place; therefore, there is already a large force on the indenter when the lateral motion is still zero, and hence a large z-force at the start of the load-displacement curves. As a point of note, all following plots are given in standard SI units (e.g. Pascals and metres) unless otherwise noted.

4.2 Progressive Damage between Transverse Frames

The first part of this study consists of load scenarios where progressive damage is applied to the large grillage structure between its transverse frames. The transverse frames themselves are not directly loaded. All load scenarios in this category begin with the static load at a longitudinal (x-direction) distance of 450 mm away from a transverse frame, and end with removal of the load at a distance of 450 mm away from the other transverse frame. A distance of 450 mm was used because it corresponds with load patches 1 and 2 from the large grillage experiments (described in Chapter 2). This distance allows the shear reaction of the structure at this longitudinal position to be investigated without excessive influence from the much stiffer transverse frame. Progressive damage closer than 450 mm to the transverse frames is discussed in section 4.3.

4.2.1 Load scenario 1: progressive damage between longitudinals

The static load was applied to the hull plating between two longitudinal stiffeners at location 1 (shown in Figure 4-2). The dynamic load consisted of dragging the indenter

1.1176 m in the longitudinal direction to the point of unloading. Figure 4-2 depicts this scenario as well as the location of the static and dynamic structural capacity comparison (labelled “location 1”).

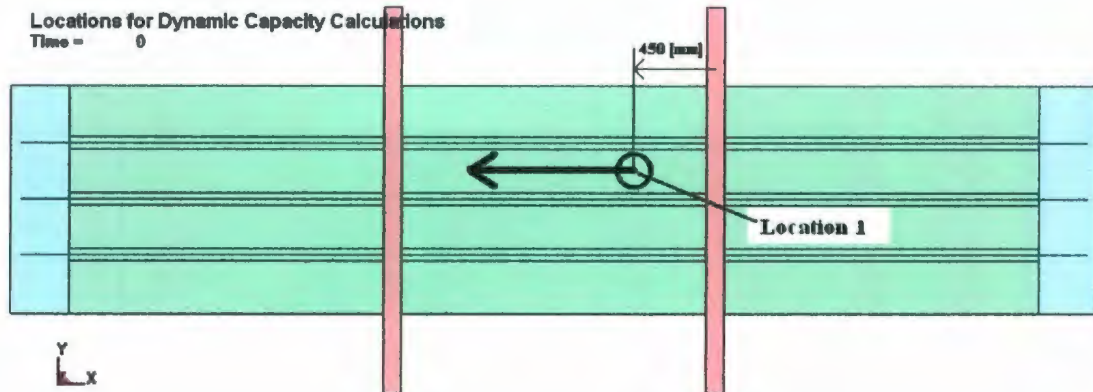


Figure 4-2: Load scenario 1: progressive damage between longitudinals and transverses.

Results for the five load cases simulated for this scenario are presented in the form of z-force reaction versus lateral displacement curves. The load-displacement results for the 0.2 and 0.5 cm load cases are given in Figure 4-3. Note that the locations of the static load and the unloading points are symmetric about the longitudinal centre of the structure. Therefore, if the principle of superposition held, the load-displacement curves shown in Figure 4-3 would be symmetric about a point half way along the x-axis of the plot. The load-displacement curves would be “bowl shaped”, with their maximum loads at $x=0$ and $x=1.1176$ m, and their minimum load at $x=0.5588$ m. The z-force reactions near the transverse frames would be maxima because these frames are much stiffer than the surrounding structure. The longitudinal bending moments would tend to be about the transverse frames. These bending moments would be small for loads near the transverses,

because the lever arms would be small. The structural reaction to these loads would be dominated by shear forces (i.e. high shear forces and low bending moments). When the indenter reached the centre of the structure, the bending moment would be maximized, and the shear force required to support the load would therefore be reduced; causing the “bowl shaped” load-displacement curves.

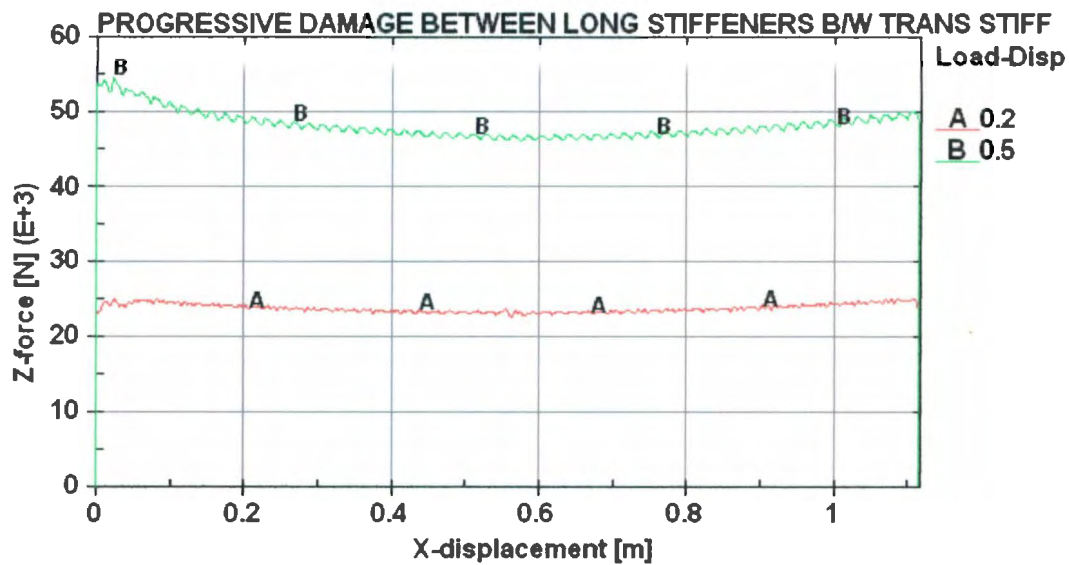


Figure 4-3: Load scenario 1: load-displacement curves for 0.2 and 0.5 cm load cases.

Indeed, this superposition supposition is true for the 0.2 cm load case. The z-force reaction drops slightly as the indenter moves away from its start, is a minimum at the centre of the lateral displacement, and gradually rises again to the same level as it approaches the other transverse frame. Because the start and finish loads are equal, the static structural capacity and the dynamic structural capacity are the same for location 1. In addition, because superposition holds, the structures reaction to this load case is

effectively elastic. Figure 4-4 shows the residual plastic strain in the large grillage structure for the 0.2 cm load case. It is apparent from this figure that very little plastic damage was done to the structure. Note that the maximum plastic strain²⁰ shown is 0.00078 (i.e. <0.1% elongation past yield) and the average plastic strain is approximately 0.00039. Thus, it is safe to assume that the structural reaction is effectively elastic.



Figure 4-4: Load scenario 1: Residual plastic strain for 0.2 cm load case.

The load-displacement curve for the 0.5 cm load case is somewhat different from the 0.2 cm load case. It has the “bowl shape” of the previous load case, but the final load is not equal to the start load. This load-displacement curve is, therefore, asymmetric; indicating

²⁰ Plastic strain refers to the component of total strain that occurs after yield; and does not include the elastic strain. I.e. total strain = elastic strain + plastic strain.

that superposition does not hold, and that the local plastic damage has affected the overall structural reaction. Figure 4-5 shows a plot of the residual plastic strain for the 0.5 cm load case. The maximum plastic strain is 1.381% plastic elongation (an order of magnitude higher than the 0.2 cm load case) and the average plastic strain is just less than 1%. While these values are not large values of plastic strain, they are much larger than for the 0.2 cm load case.

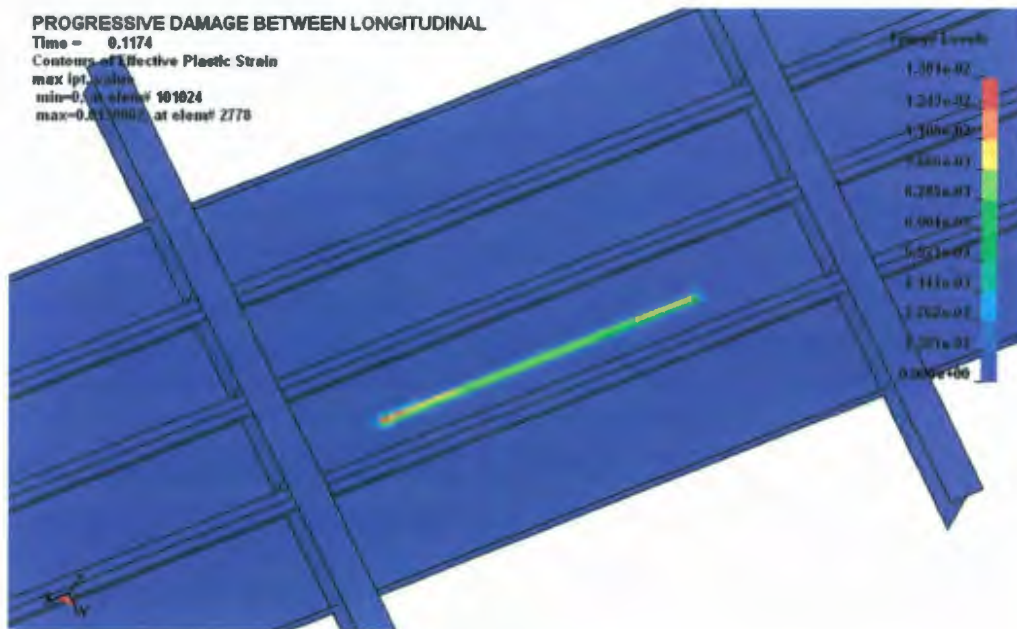


Figure 4-5: Load scenario 1: Residual plastic strain for 0.5 cm load case.

The z-force reaction for the 0.5 cm load case starts at 54.6 kN and finishes at 49.5 kN. Therefore, the dynamic application of the same load that was initially applied statically resulted in a decreased structural capacity. This is a decrease of 9% from the static structural capacity to the dynamic structural capacity (for location 1). This suggests that

the structural mechanisms associated with the dynamic application of a load have a negative effect on the structures capacity to sustain that load.

The load-displacement results for all five load cases are given in Figure 4-6. A distinct and immediate drop in the z-force reaction is apparent for the higher load cases. This load drop happens upon commencement of the lateral motion of the indenter for the 2, 5, and 10 cm load cases. As well, the “bowl shape” of the 0.2 and 0.5 cm load-displacement curves is not evident for the higher load cases. Instead, the load drops sharply to a much lower level, at which point it approximately remains steady (i.e. independent of lateral position).

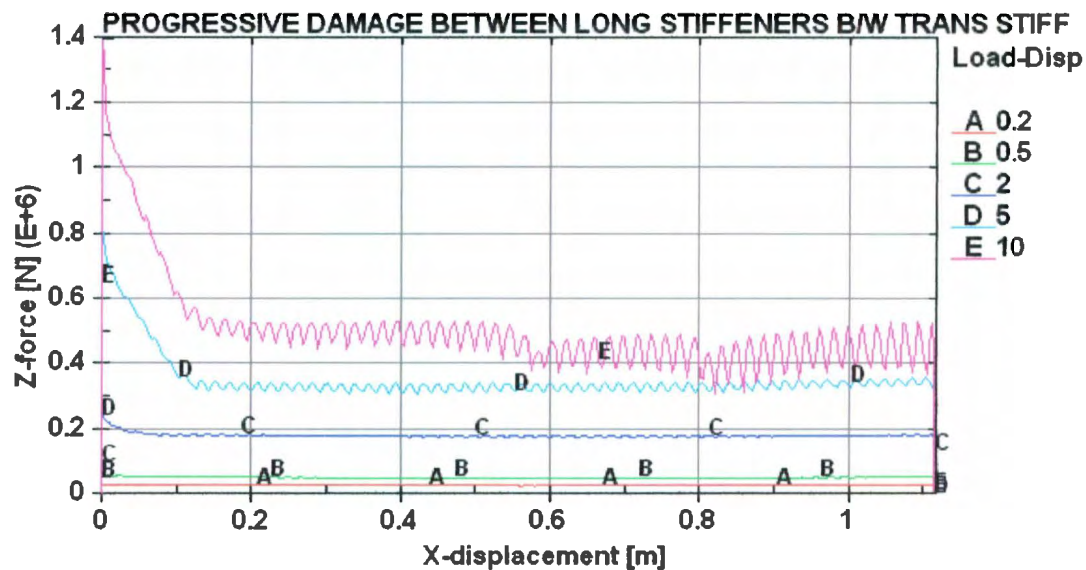


Figure 4-6: Load scenario 1: load-displacement curves for all five load cases.

Figure 4-7 shows the z-force time-history curves for these load cases. This figure presents the same z-force information as Figure 4-6, but because it is plotted against time, the maximum values for the static load reactions are easier to discern.

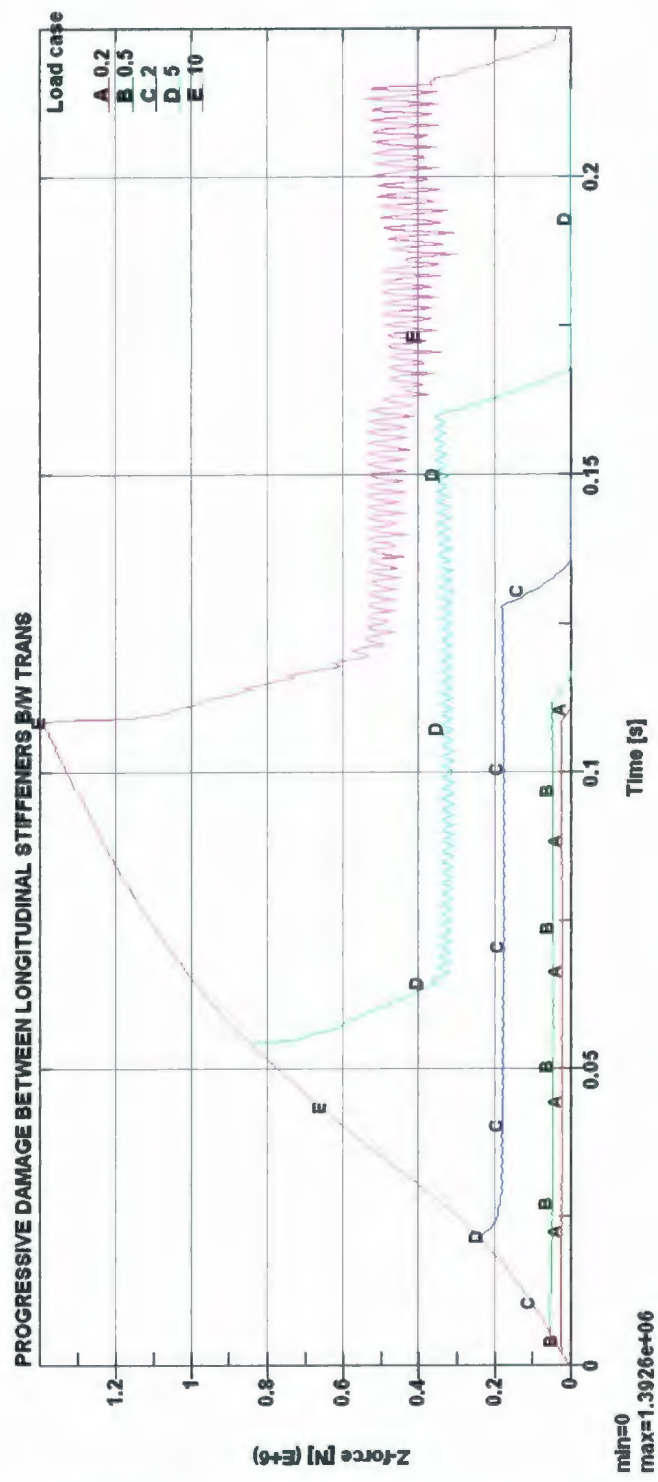


Figure 4-7: Load scenario 1: z-force time-history plot for all load cases.

The structure's reaction to a static load is apparently quite different to that of a dynamic load for these higher load cases. For the 2 cm load case, the static load capacity at location 1 is approximately 244 kN (as seen in Figure 4-7: line C before the load drop). The dynamic capacity is approximately 175 kN (as seen in Figure 4-7: line C just before the unloading section). This equals a 28% decrease in structural capacity between the static and dynamic loads. For the 5 cm load case, the static load capacity is 838 kN, the dynamic load capacity is 337 kN, and the dynamic decrease in capacity is approximately 60%. For the 10 cm load case, the static load capacity is 1.39 MN, the dynamic load capacity is 450 kN, and the dynamic decrease in capacity is approximately 68%²¹.

Figure 4-8 and Figure 4-9 show the residual plastic strains for the 2 and 5 cm load cases. The maximum and average plastic strains for the 2 cm load case are 4.32% and 3.45% plastic elongation, respectively. The maximum and average plastic strains for the 5 cm load case are 41.01% and 16.40% plastic elongation, respectively. Figure 4-10 shows a maximum plastic strain of 143% plastic elongation, and an average of approximately 56% plastic elongation for the 10 cm load case. Note that the load-curve for the 10 cm load case is not to be taken as an indication of the structures actual reaction to a 10 cm progressive damage load. Clearly, the hull plating would have failed under these conditions. It is presented to give an exaggerated indication of the phenomena prevalent in the lower load cases.

²¹ This latter number is presented only to indicate the trend. As mentioned above, it is expected that the large grillage would fail (i.e. the indenter would tear through the hull plating) for this load case.

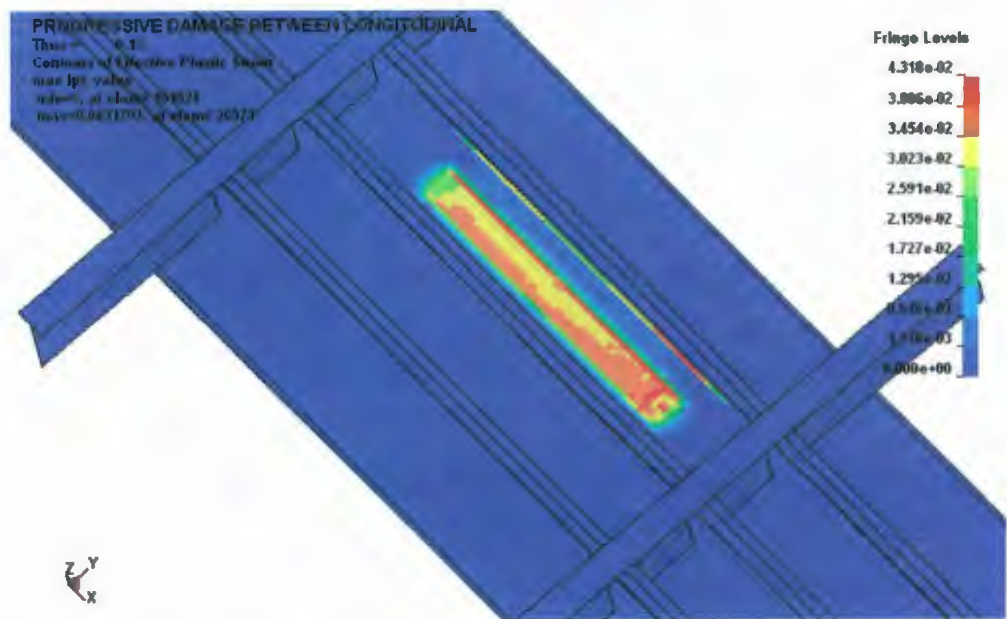


Figure 4-8: Load scenario 1: residual plastic strain for load case 1: 2 cm indentation.

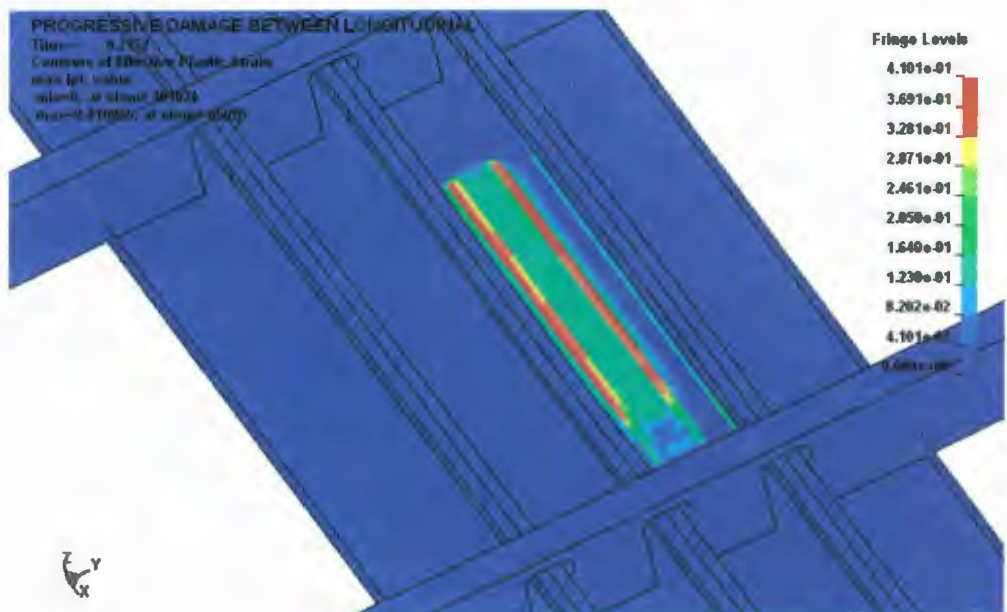


Figure 4-9: Load scenario 1: residual plastic strain for load case 1: 5 cm indentation.



Figure 4-10: Load scenario 1: residual plastic strain for load case 1: 10 cm indentation.

By comparing the load-displacement curves of Figure 4-6 with their respective plastic structural damage, it is clear that there is an inverse relationship between structural load-capacity and plastic damage for all load cases.

4.2.1.1 Further investigation

An attempt to identify the structural mechanisms causing the dramatic decrease between static and dynamic structural capacities was made. Investigation of the existing results suggests that the structure's response to the static load is approximately symmetric around the point of application of the load. That is, resultant structural displacements are smooth and decrease evenly with increasing distance from the load (Figure 4-11); plate bending is smooth and occurs in two directions (illustrated by the twisting moment plot given in

Figure 4-12); and plate membrane stresses are approximately radially constant (Figure 4-13). Of course, the surrounding stiffening structure (i.e. the longitudinal and transverse stiffeners) deforms as well, but there are no major failure structural mechanisms at work (e.g. stiffener buckling).

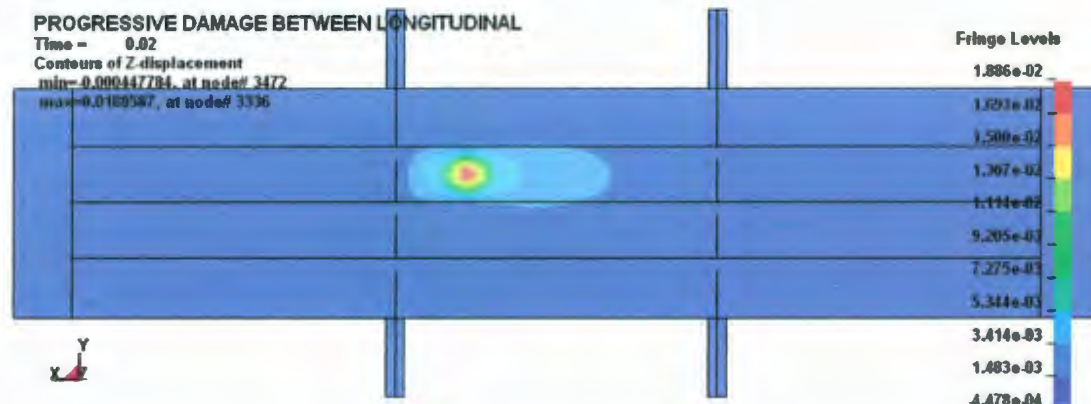


Figure 4-11: Load scenario 1: static load z-displacement (indenter not shown): 2 cm load case.

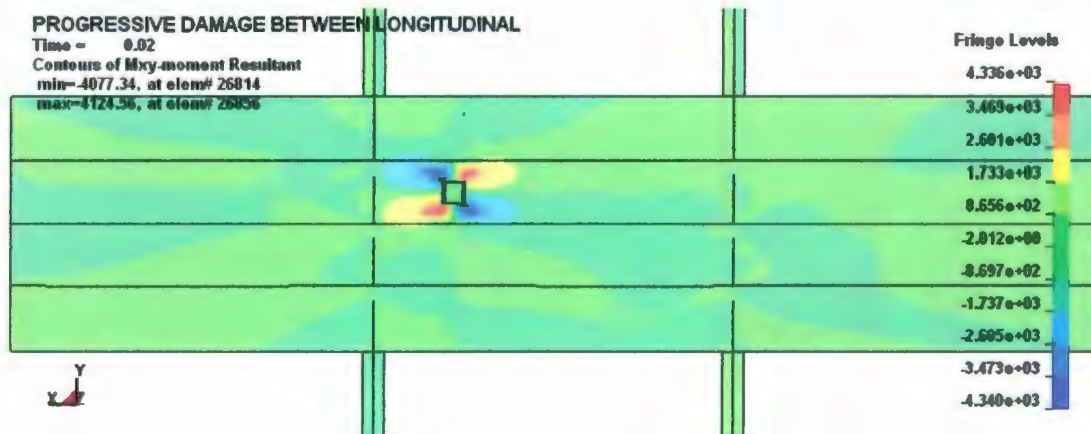


Figure 4-12: Load scenario 1: static load M_{xy} moment distribution: 2 cm load case.

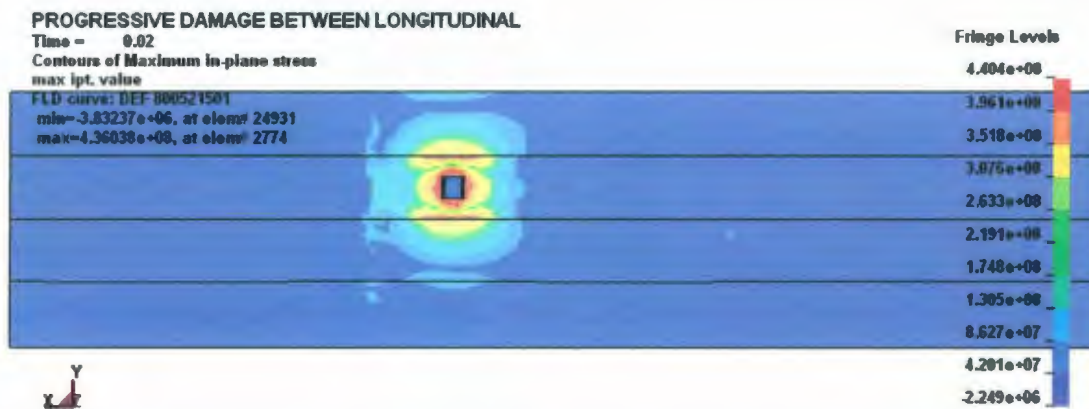


Figure 4-13: Load scenario 1: static load in-plane maximum stress (indenter shown, transverses not shown): 2 cm load case.

Investigation of the dynamic load revealed that the symmetries present for the static load no longer exist. Upon commencement of lateral motion, the indenter is required to deform the structure “ahead” of its lateral path while the structure behind it retains considerable residual deformation. This phenomenon is illustrated in Figure 4-14, which shows the z-displacement (i.e. into the page) of the hull plating during the dynamic load. Notice that the structure behind the indenter retains its z-deformation long after the indenter has passed by, indicating that the structure is permanently deformed in this region.

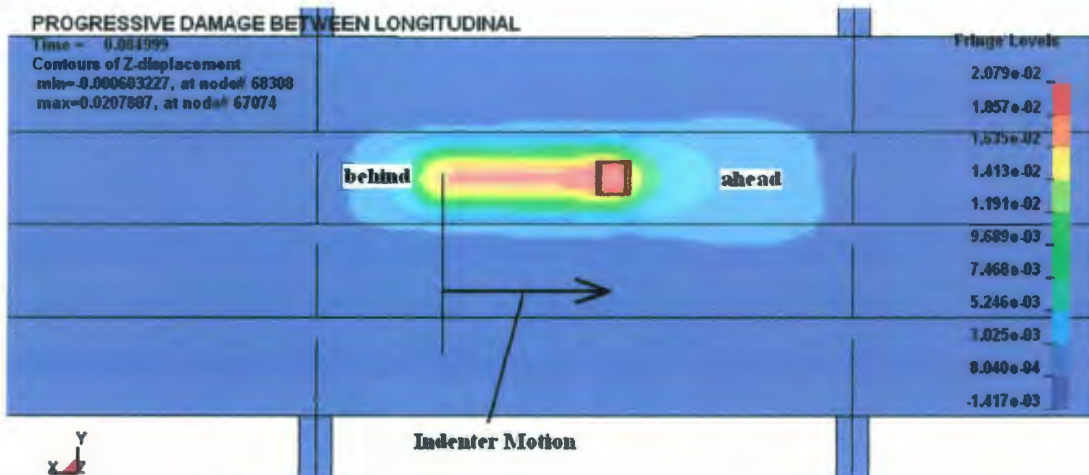


Figure 4-14: Load scenario 1: dynamic load z-deformation: 2 cm load case.

From the M_{xy} moment distribution plot given in Figure 4-15, it is apparent that significant plate bending is occurring ahead of the indenter's lateral motion, but not behind it. This is indicated by the asymmetry of the bending moment distribution around the indenter. This asymmetry is shown by the presence of only two "lobes" of large magnitude M_{xy} bending moments ahead of the indenter, rather than the four lobes present in Figure 4-16 for the 0.2 cm elastic load case.

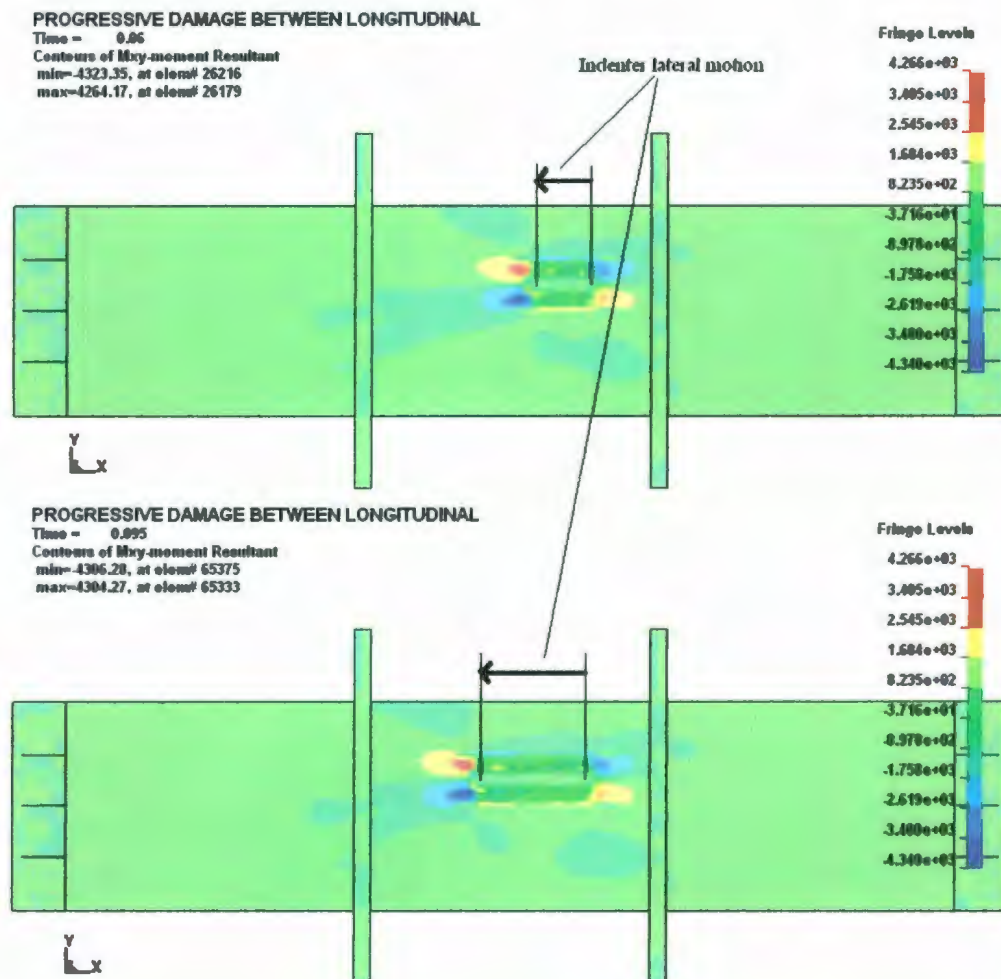


Figure 4-15: Load scenario 1: dynamic load M_{xy} bending moment distribution: 2 cm load case.

Because plate bending occurs mostly ahead of the lateral motion, the indenter is doing considerably less work to bend the hull plating than during the symmetric response to the static load. This indicates that prior plastic damage reduces the extent of plate bending that occurs during the dynamic load. This reduction in the plate bending response most likely contributes to the decrease in structural capacity observed between the static and dynamic loads.

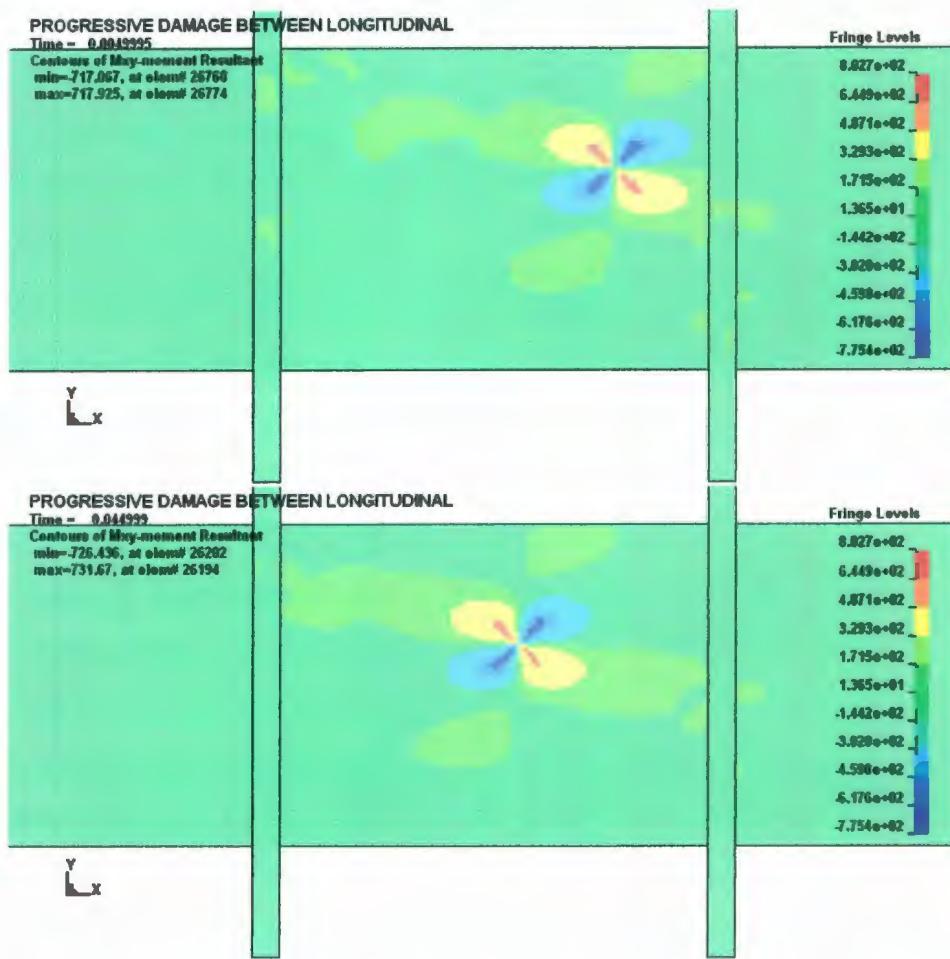


Figure 4-16: Load scenario 1: M_{xy} plot for static (top) and dynamic (bottom) loads: 0.2 cm load case.

Plots similar to Figure 4-15 for maximum in-plane stress are given in Figure 4-17. These plots illustrate the membrane stresses present during the dynamic loading of the 2 cm load case. The symmetry of the membrane stresses observed during the static load (as seen in Figure 4-13) still seems to be present in the dynamic load, but is augmented with two extra areas of high stress-concentration near the “behind” corners of the indenter (areas shown circled in Figure 4-17). These extra highly-stressed regions seem to be the result

of new tension that was not present during the static load. Figure 4-18 shows an N_{xy} in-plane shear force distribution that is overlaid with pink squares denoting the location of the largest maximum in-plane stresses shown in Figure 4-13. From Figure 4-18, it is apparent that the new highly-stressed areas result from in-plane shear forces that were not present during the static load. As well, these areas are coincident with the part of the hull plating behind the indenter that carries no M_{xy} bending moment. Because of this, it was theorized that these new highly-stressed areas supported very little through-plane shear force, and hence partially disabled the structures ability to produce a z-force reaction.

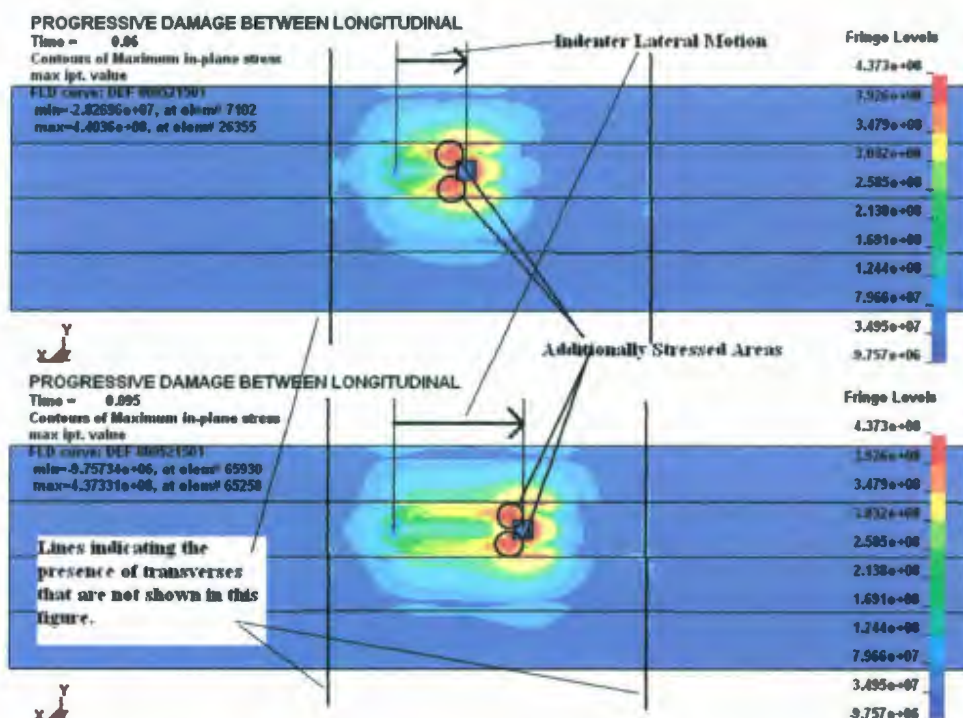


Figure 4-17: Load scenario 1: dynamic load in-plane maximum stress distribution: 2 cm load case.

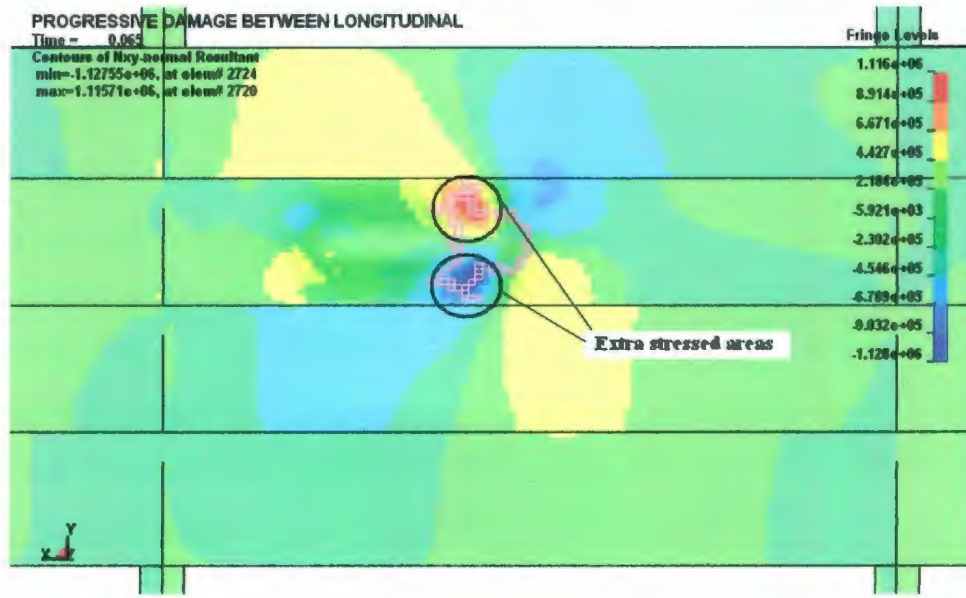


Figure 4-18: N_{xy} plot with highest maximum in-plane stressed elements outlined in pink.

Figure 4-19 and Figure 4-20 show the Q_x and Q_y through-plane shear force distributions around the indenter for the static load (top of each figure) and the dynamic load (bottom of each figure). Note the symmetry of the through-plane shear force distributions around the indenter for the static load, and the asymmetry for the dynamic load. These figures show a reduced through-shear capacity for the structure behind the indenter for the dynamic load. Further, the Q_y through-plane shear is approximately zero for the new highly stressed areas. This reduction in through-plane shear capacity contributes to the decrease in dynamic structural capacity observed in this load case.

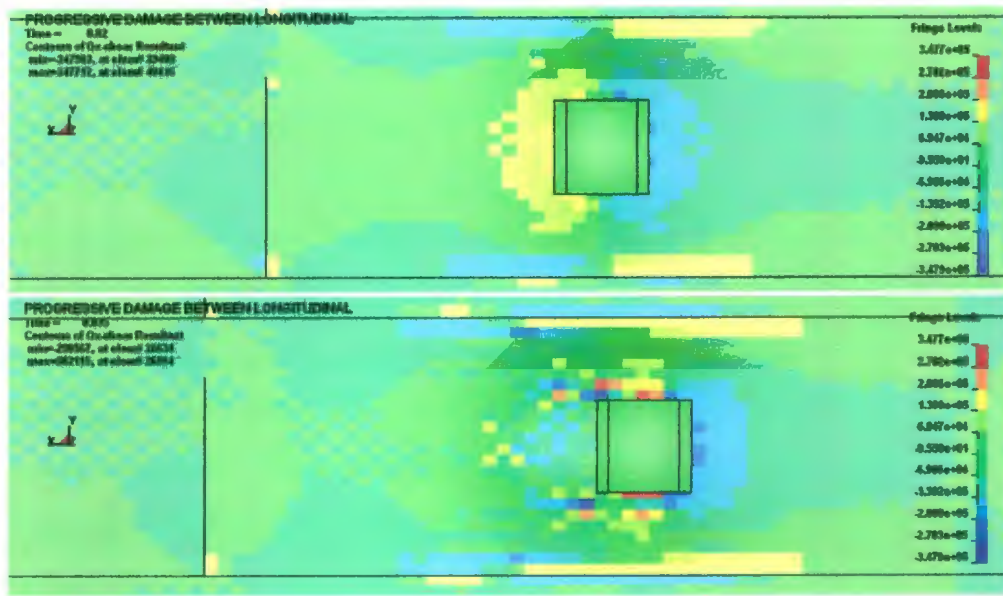


Figure 4-19: Load scenario 1: Q_x through-plane shear force for static load (top) and dynamic load (bottom): 2 cm load case.

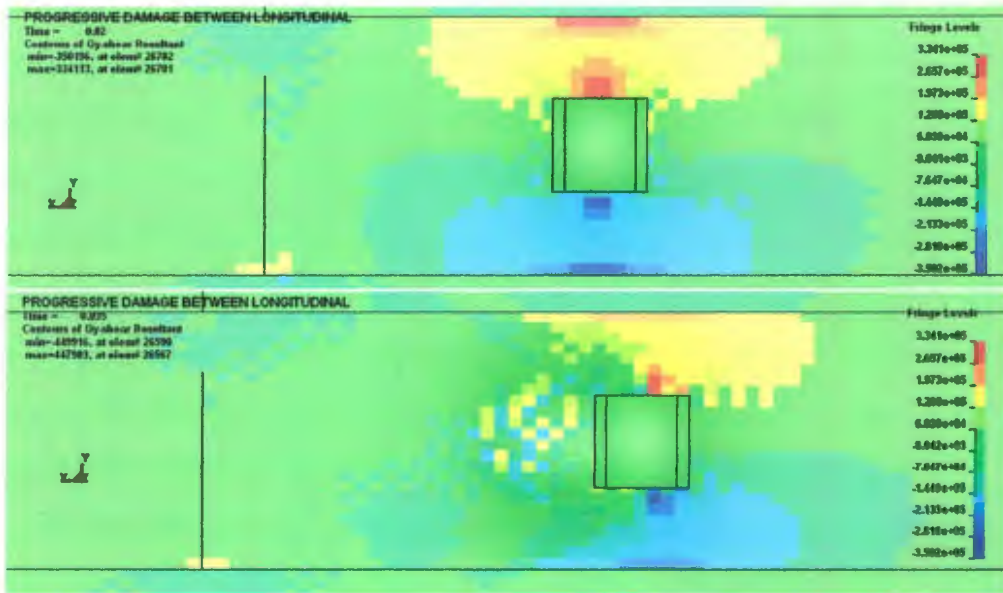


Figure 4-20: Load scenario 1: Q_y through-plane shear force for static load (top) and dynamic load (bottom): 2 cm load case.

4.2.2 Load scenario 2: progressive damage along a longitudinal

The static load was applied to the central longitudinal stiffener at location 2 (shown in Figure 4-21). The indenter was then dragged 1.1176 m in the longitudinal direction, and then the structure was unloaded. Figure 4-21 depicts this scenario as well as the locations of the static and dynamic structural capacity comparisons (labelled “location 2” and “location 3”).

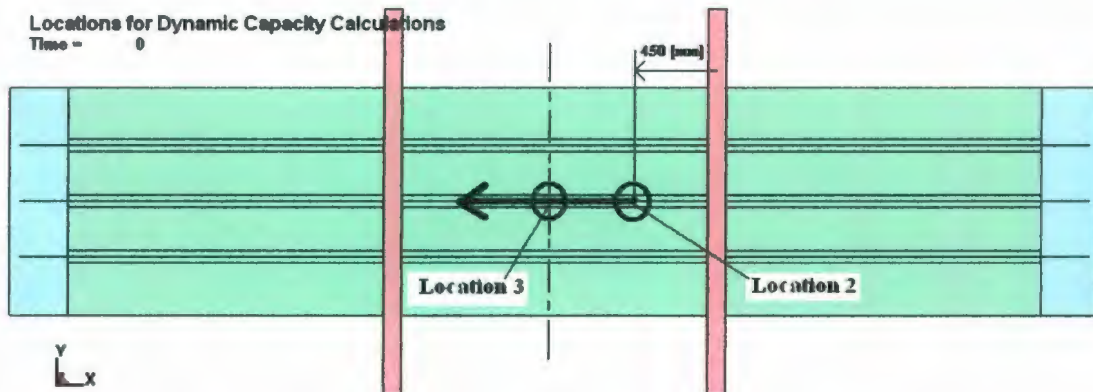


Figure 4-21: Load scenario 2: progressive damage along longitudinal and between transverses.

Results for the load cases simulated for this scenario are presented in the form of z-force reaction versus lateral displacement curves. The load-displacement results for the 0.2 and 0.5 cm load cases are given in Figure 4-22.

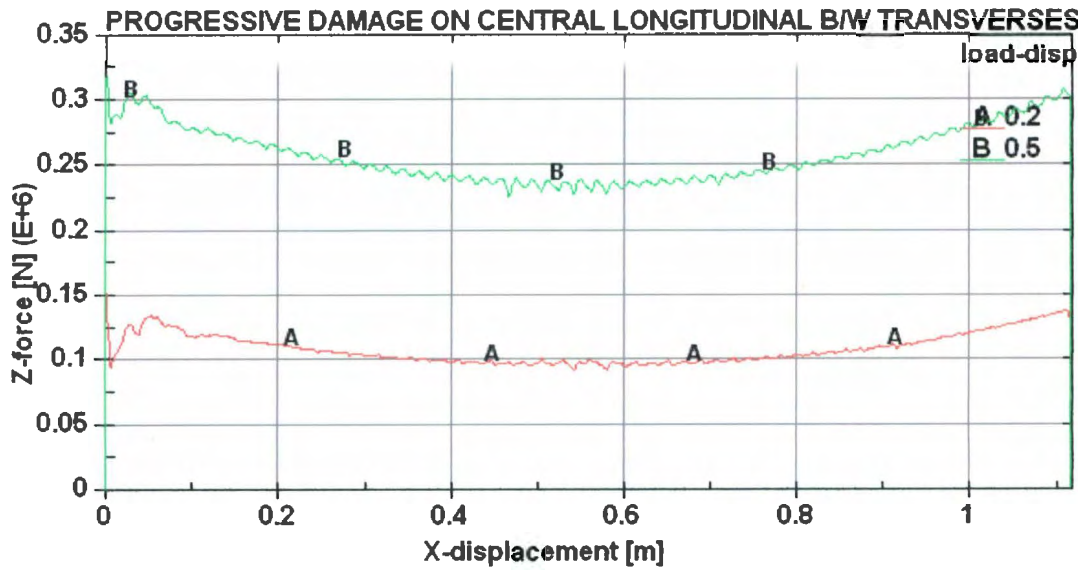


Figure 4-22: Load scenario 2: load-displacement curves for 0.2 and 0.5 cm load cases.

As in load scenario 1, the “bowl shaped” reaction force is present for the 0.2 and 0.5 cm load cases. Unlike the previous load scenario, there is an initial drop in load that rises again quickly. Further, the start and finish loads are not equal for both cases.

4.2.2.1 0.2 cm load case

Investigation of the 0.2 cm load case showed that plate bending was small for this level of indentation. The longitudinal stiffener is much stiffer than the hull plating, and tends to dominate the structural response. To illustrate this, Figure 4-23 shows the M_{xy} moment distribution for the dynamic load section of the 0.2 cm load case, for both load scenario 1 and load scenario 2. The fringe levels in both plots have been set equal so that a direct comparison may be made. It is obvious from the figure that the magnitude of the M_{xy} moment distribution is much smaller for load scenario 2 than for load scenario 1.

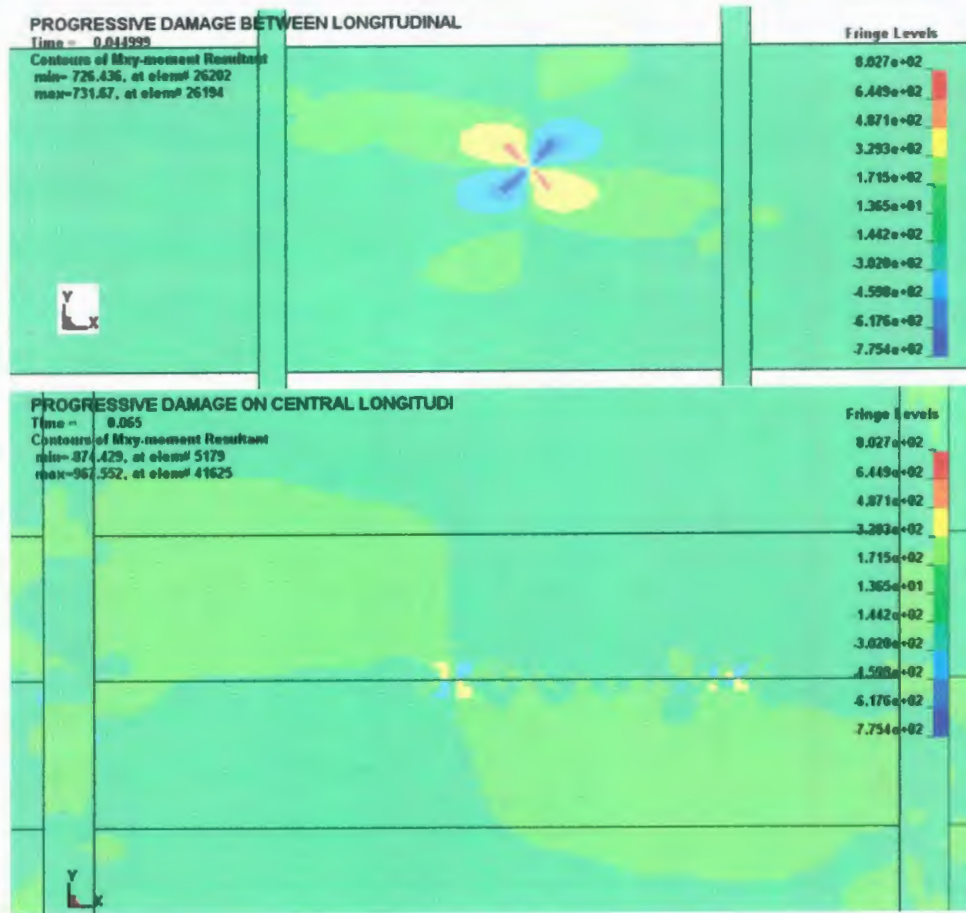


Figure 4-23: Load scenario 2: dynamic load M_{xy} plot for load scenarios 1 (top) and 2 (bottom): 0.2 cm load case.

Further, hull plate membrane stretching and longitudinal stiffener buckling are negligible. The structure remained almost entirely elastic during this load scenario. The slight plastic deformation that did occur is shown in Figure 4-24. It is assumed that this plastic strain is negligible due to its extremely small extent and magnitude (the maximum plastic elongation is <1% and the average is <0.4%). Plastic deformation was therefore ruled out as a possible cause for the initial drop in load observed in Figure 4-22.

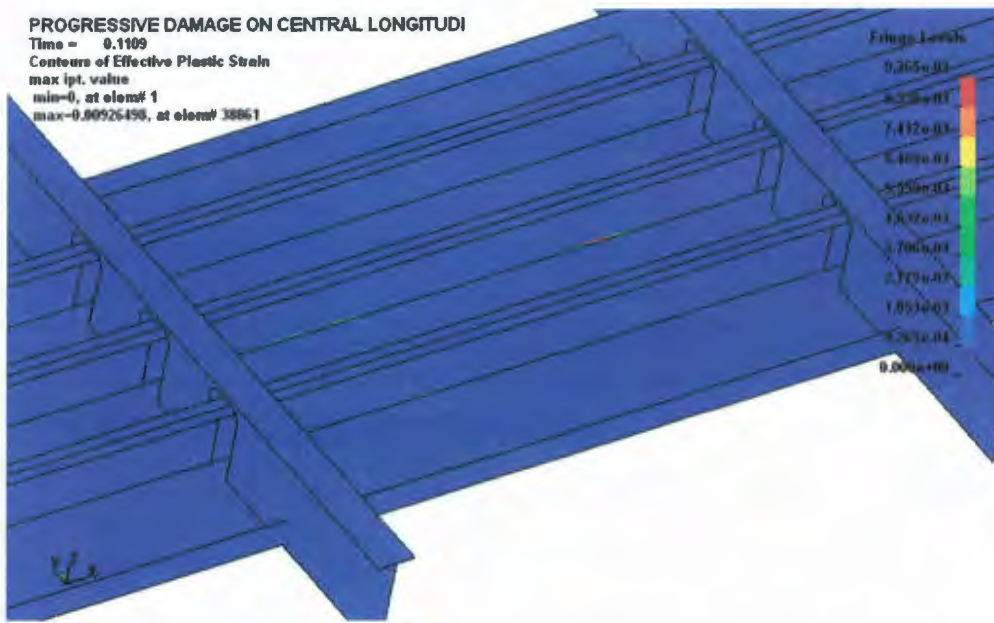


Figure 4-24: Load scenario 2: plastic strain for load case 0.2 cm.

It was found that the initial drop in load was a dynamic result of the method of application of load. Figure 4-25 shows the z-direction rigid-body motion time-history of the longitudinal stiffener web at a point above the static load, for the entire load case. As mentioned above, loads were applied to the structure by imposing displacements on the indenter. Displacements were imposed at a constant velocity; therefore, at the end of the static loading section of the load case, the indenter's velocity changed from constant to zero (rest) in a very short time period (causing near infinite deceleration of the indenter). The indenter's z-motion ceased abruptly while the large grillage structure continued to deform slightly in the z-direction due to its inertia. For the 0.2 cm load case (and to a lesser extent, the 0.5 cm load case), a minor structural response oscillation at the natural frequency of the structure occurred causing an artificially high initial load, followed by a

drop in load, followed by another rebound at which point the vibration was finally damped out. It is therefore assumed that the initial load drop observed in Figure 4-22 is an artefact of the method of application of load, and that the load-displacement curve for the 0.2 cm load case should have equal start and finish loads. Further, the load-curve should be “bowl shaped” and symmetric about the centre of the x-axis of Figure 4-22. The same holds true to a lesser extent for the 0.5 cm load case. Plastic damage is slightly more prominent for this load case (as outlined below) but it is not clear if this plastic damage is sufficient to affect the structures overall response. It is probable however, that this plastic damage served to dampen the dynamic oscillation to a greater degree than for the 0.2 cm load case, resulting in an initial load oscillation that was smaller in magnitude.

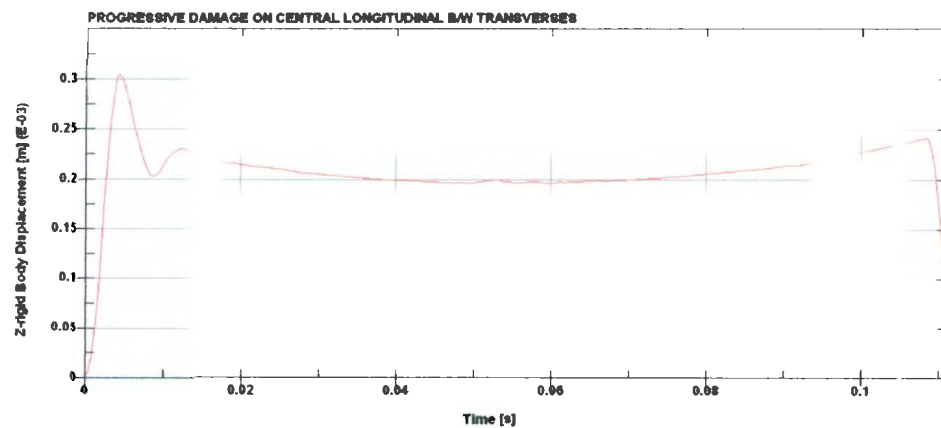


Figure 4-25: Load scenario 2: rigid body z-displacement of the longitudinal stiffener web: 0.2 cm load case.

4.2.2.2 Other load cases

Despite the dynamic oscillation noted above, the static capacity at location 2 for this load case is known because location 2 is coincident with “load patch 1” from the large grillage experiments. “Load patch 1” was used to validate the numerical model. The z-force versus z-displacement curve for location 2 is given in Figure 4-26.

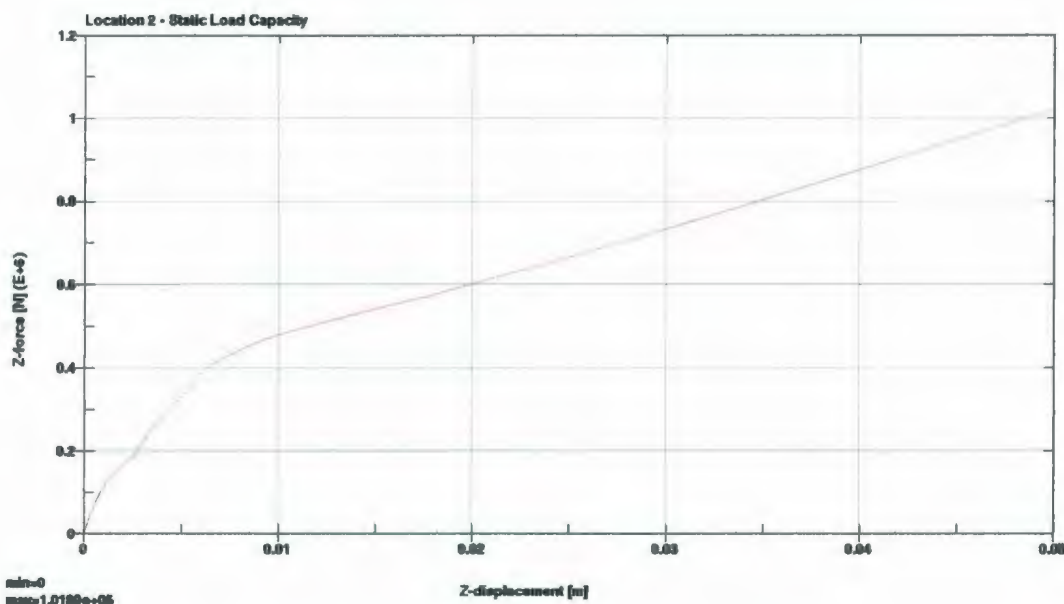


Figure 4-26: Static load capacity curve for location 2.

From this figure, the static load capacity for location 2 at an indentation of 0.5 cm is 329 kN. From Figure 4-22, the dynamic load capacity is 294 kN. Therefore, the decrease in structural capacity for the 0.5 cm load case at location 2 is approximately 10.5%. Further, the static load capacity at location 3 is also known. A separate simulation was conducted to discover this curve, which is presented in Figure 4-27. From this figure, the static

structural capacity for location 3 at an indentation of 0.5 cm is 249 kN. The dynamic structural capacity from Figure 4-22 is 233 kN. Therefore, the decrease in structural capacity for the 0.5 cm load case at location 3 is approximately 6.5%.

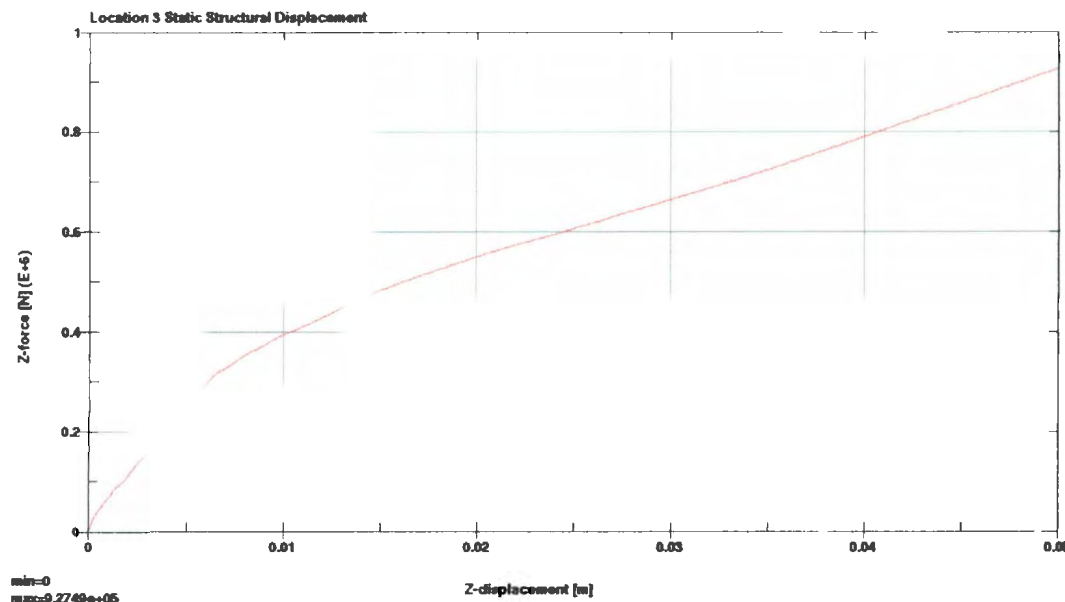


Figure 4-27: Static load capacity curve for location 3.

Investigation into the dynamic decrease in structural capacity was conducted. Plastic damage to the longitudinal stiffener and the hull plating began to affect the reaction of the structure at the 0.5 cm load case. Plastic strain for the structure for this load case is a maximum of approximately 8% plastic elongation, and an average of approximately 4% plastic elongation (as seen in Figure 4-28). A plot of the M_{xy} moment distribution (Figure 4-29) reveals that plastic damage is starting to affect the symmetry of the structural plate bending (as seen by the relative difference in “lobe” areas 1 and 2). The

plate-bending component of the overall structural reaction, however, seems to be small compared with that provided by the compression of the longitudinal stiffener web and the bending of the longitudinal stiffener flange.

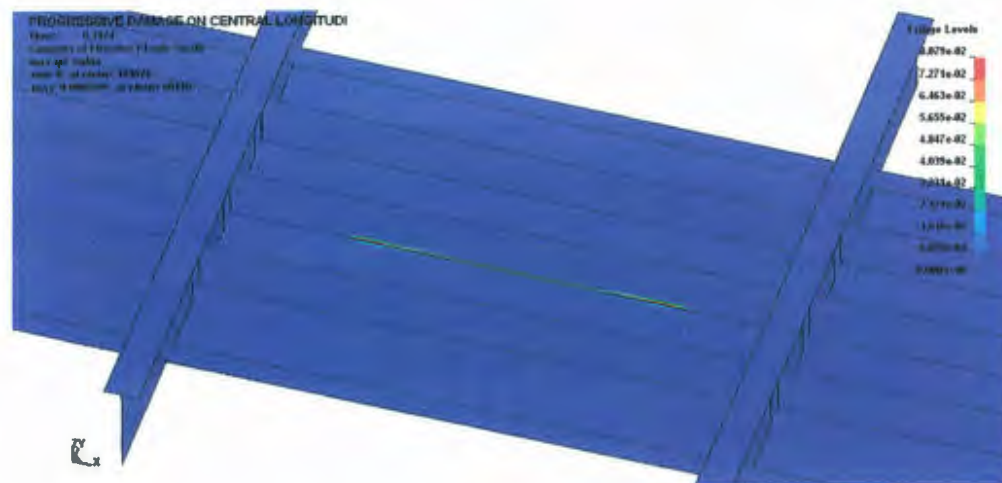


Figure 4-28: Load scenario 2: plastic strain for the 0.5cm load case.

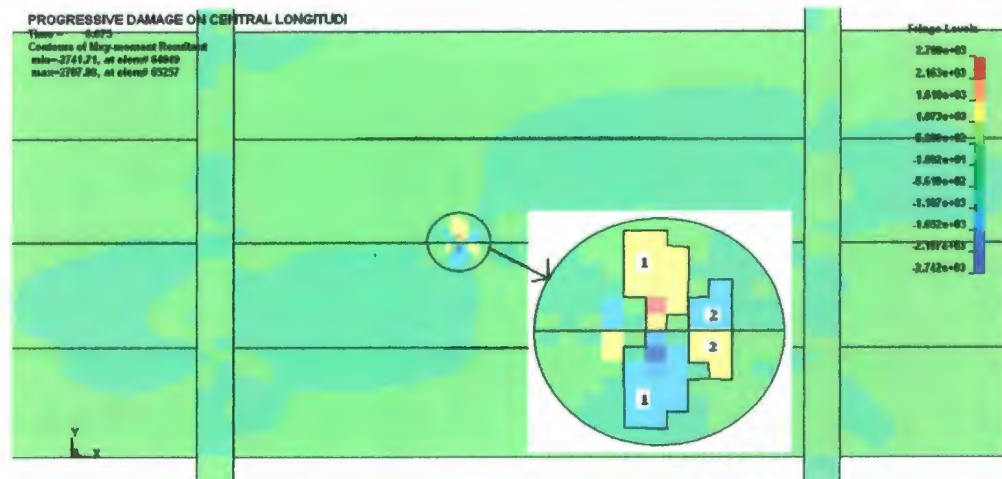


Figure 4-29: Load scenario 2: dynamic load M_{xy} plot for the 0.5 cm load case.

The load-displacement curves for all load cases except the 10 cm load case²² are given in Figure 4-30. Like load scenario 1, there are initial drops in z-force for the higher load cases; and similarly, the load drops are proportional to the magnitude of indentation.

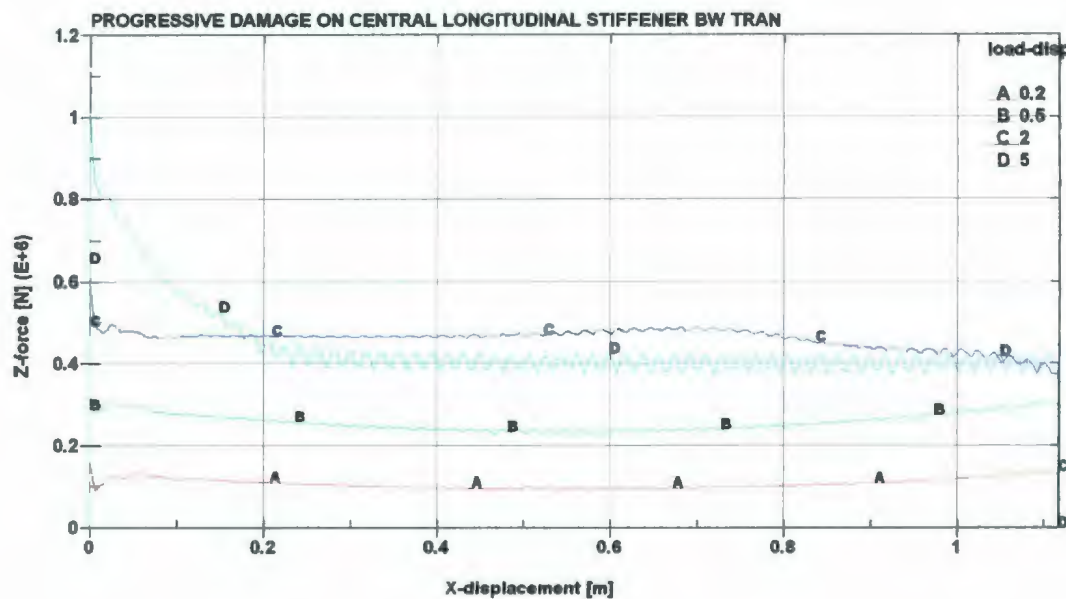


Figure 4-30: Load scenario 2: load-displacement curves for all load cases.

As in load scenario 1, this figure suggests that upon commencement of the dynamic load, the capacity of the structure decreases dramatically from its static load capacity. In fact, this figure suggests that the dynamic capacity of the structure to withstand a 5 cm dynamic load is actually less than its capacity to withstand a 2 cm dynamic load. At location 2, for the 2 cm load case, the static structural capacity is approximately 600 kN and the dynamic structural capacity is 380 kN. This indicates a 37% decrease in

²² The results for the 10 cm load case were only meant to provide an exaggerated extrapolation of the phenomena found in the lower load cases. In this case, results from the 10 cm load case added no value to the figure.

structural capacity at location 2. At location 3, for the 2 cm load case, the static structural capacity is approximately 550 kN (from Figure 4-27) and the dynamic structural capacity is 475 kN. This indicates a 13.5% decrease in structural capacity at location 3. At location 2, for the 5 cm load case, the static structural capacity is 1.014 MN and the dynamic structural capacity is 400 kN. This indicates 60% decrease in structural capacity at location 2. At location 3, for the 5 cm load case, the static structural capacity is 927 kN and the dynamic structural capacity is 400 kN. This indicates 57% decrease in structural capacity at location 3.

Investigation into the structural mechanisms causing the dynamic reduction of structural capacity suggests that there are three mechanisms involved: stiffener buckling, plate bending, and membrane stretching.

It is known that the central longitudinal stiffener web does not buckle at location 2 until a static load of approximately 7 cm is reached (see Chapter 2, Figure 2-4 or Chapter 3.13). The indentation required to buckle the stiffener at location 3 is not known; however, it is known (from a static indentation simulation) that no buckling occurs for a 10 cm static load (shown in Figure 4-31). Upon commencement of the dynamic load, the central longitudinal stiffener began to buckle immediately for the 2 and 5cm load cases.

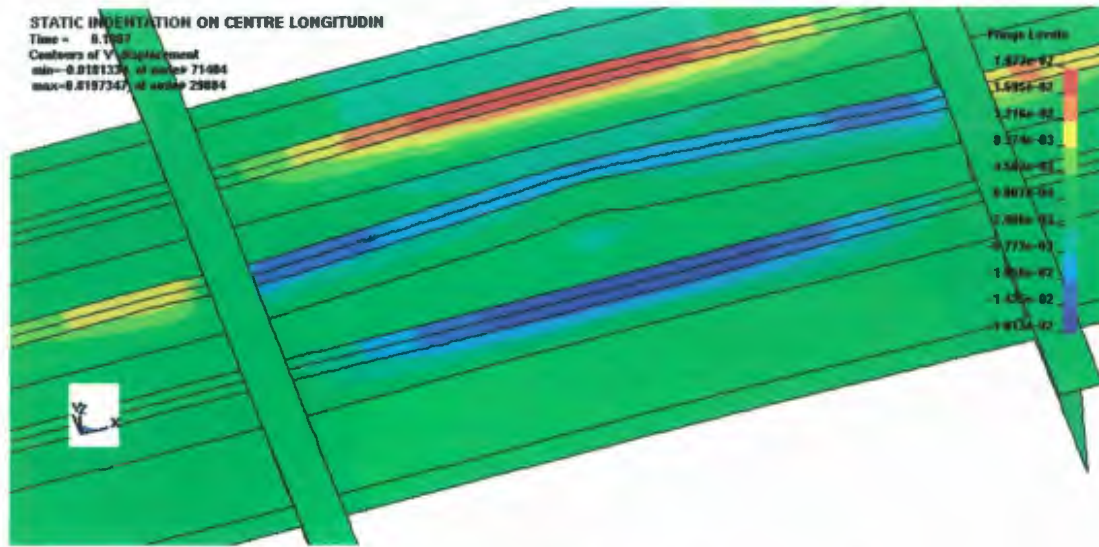


Figure 4-31: y-displacement plot for 10 cm static load at location 3.

For the 2 cm load case, stiffener buckling was small (shown in the top of Figure 4-32) until the indenter reached the longitudinal centre of the longitudinal stiffener. At this point, the buckling became much larger and continued to grow with increasing lateral indenter motion (shown in the top of Figure 4-33). This larger “post longitudinal centre” buckling had an alleviating affect on the existing “pre longitudinal centre” buckling, reducing its magnitude.

The magnitude of plate bending and membrane stretching for the 2 cm load case was proportional to the severity of the longitudinal stiffener buckling; that is, when the stiffener buckling was small, so too was the plate bending and the membrane stretching (see the middle and bottom of Figure 4-32, respectively). This indicates that the majority of the dynamic load was being supported by compression of the longitudinal stiffener web, and bending of the longitudinal flange. During the latter half of the dynamic load

(when the stiffener buckling was more pronounced), the plate bending and membrane stretching reactions increased in magnitude. This indicates that plate bending reaction and membrane stretching (see the middle and bottom of Figure 4-33, respectively) were carrying more load. Note from Figure 4-32 and Figure 4-33 that the M_{xy} bending moment distributions show bending only in the direction ahead of the indenter's lateral motion (i.e. asymmetric plate bending). As in load scenario 1, this asymmetric plate bending most likely contributes to the decrease in structural capacity observed between the static and dynamic loads. The membrane behaviour, however, remains relatively symmetric until the stiffener buckling becomes large during the second half of the dynamic load. At this time, the “highly stressed” areas discussed in load scenario 1 reappear.

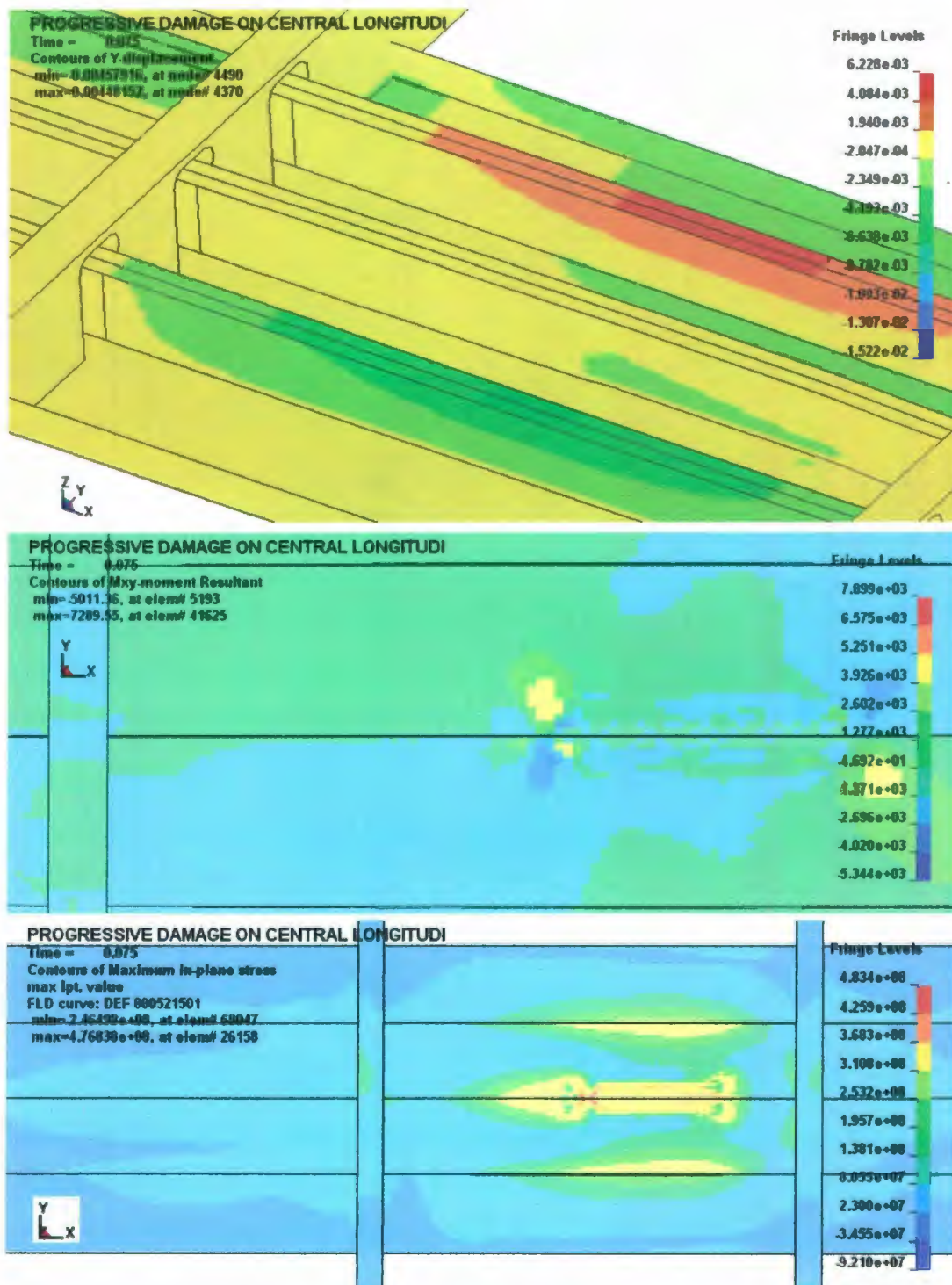


Figure 4-32: Load scenario 2: initial central stiffener buckling (top), M_{xy} moment (mid), and max in-plane stress (bottom): 2 cm load case.

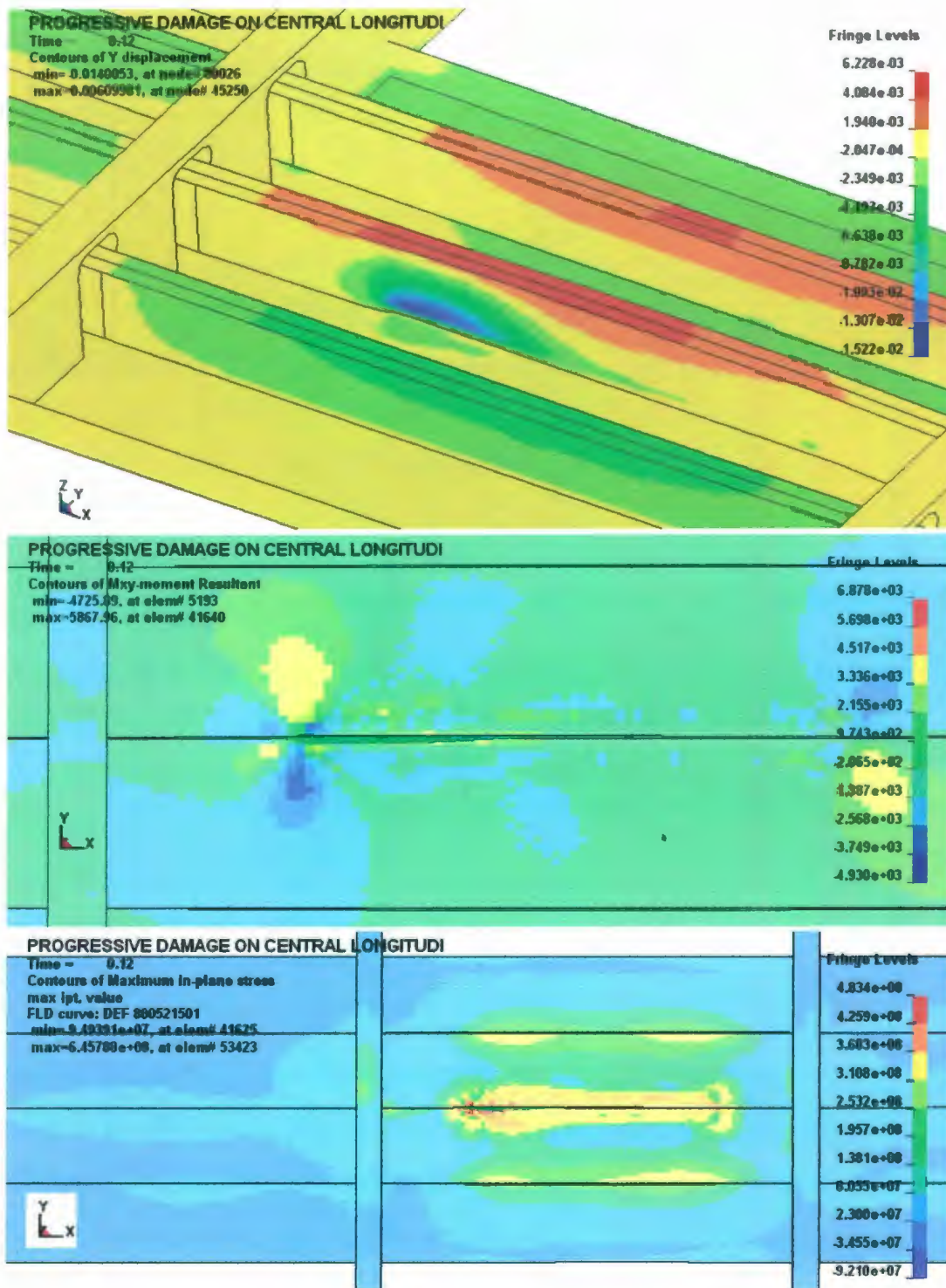


Figure 4-33: Load scenario 2: subsequent central stiffener buckling (top), M_{xy} moment (mid), and max in-plane stress (bottom): 2 cm load case.

For the 5 cm load case, the magnitude of the longitudinal stiffener buckling was much larger immediately following the commencement of the dynamic load than for the 2 cm load case. The interaction of plate bending, membrane stretching, and longitudinal stiffener buckling was similar to that of the 2 cm load case, but was more subdued. This is because the longitudinal stiffener buckled more after the start of the dynamic load, requiring the M_{xy} bending and the membrane stretching reactions to carry more load initially. Figures showing the near start and near finish longitudinal stiffener buckling, M_{xy} bending, and maximum in-plane stress plots (similar to those presented above for the 2 cm load case), are given in Figure 4-34 and Figure 4-35, respectively. It is interesting to note that the “highly stressed” areas present for the second half of the 2 cm load case, were present for the entire dynamic load for the 5 cm load case.

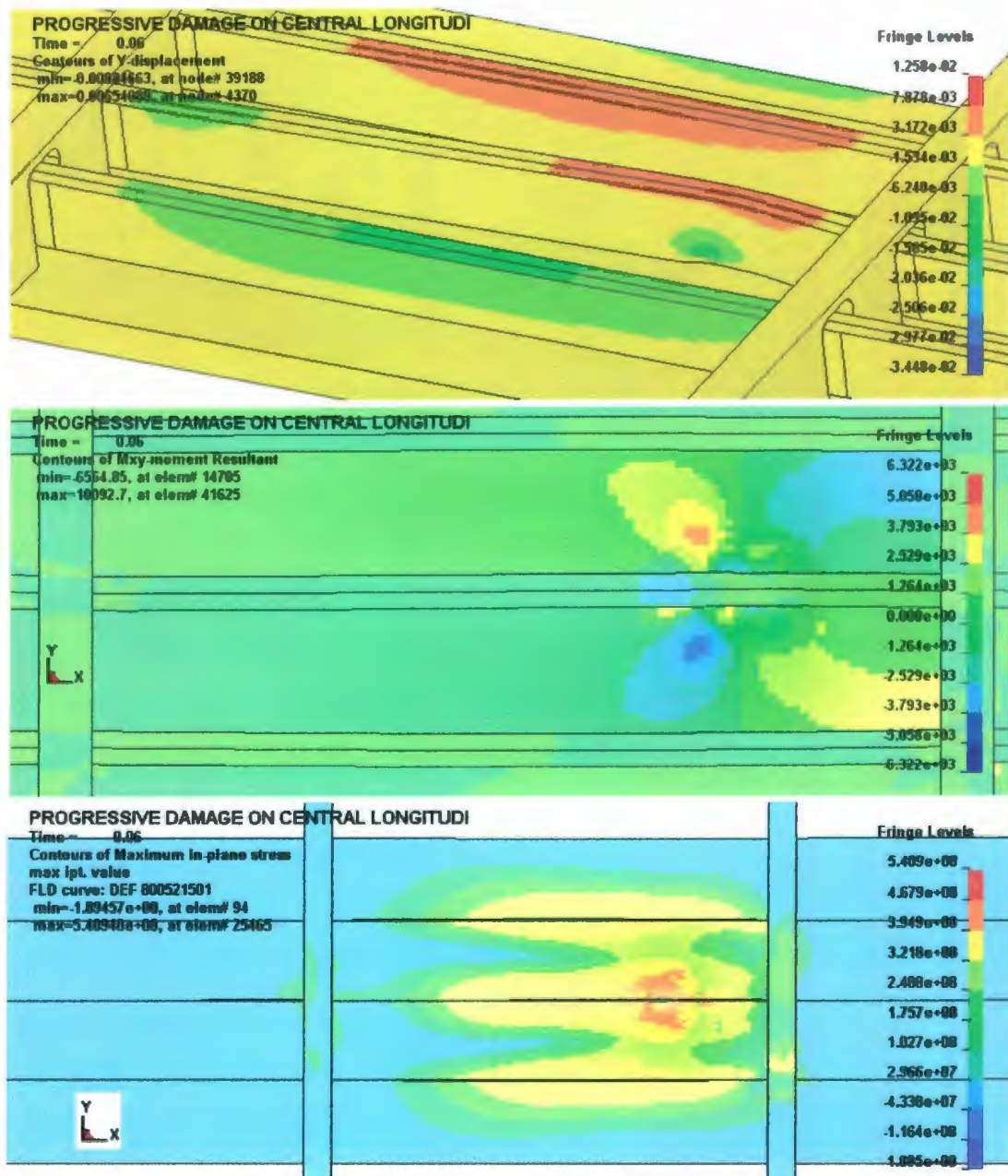


Figure 4-34: Load scenario 2: initial central stiffener buckling (top), M_{xy} moment (mid), and max in-plane stress (bottom): 5 cm load case.

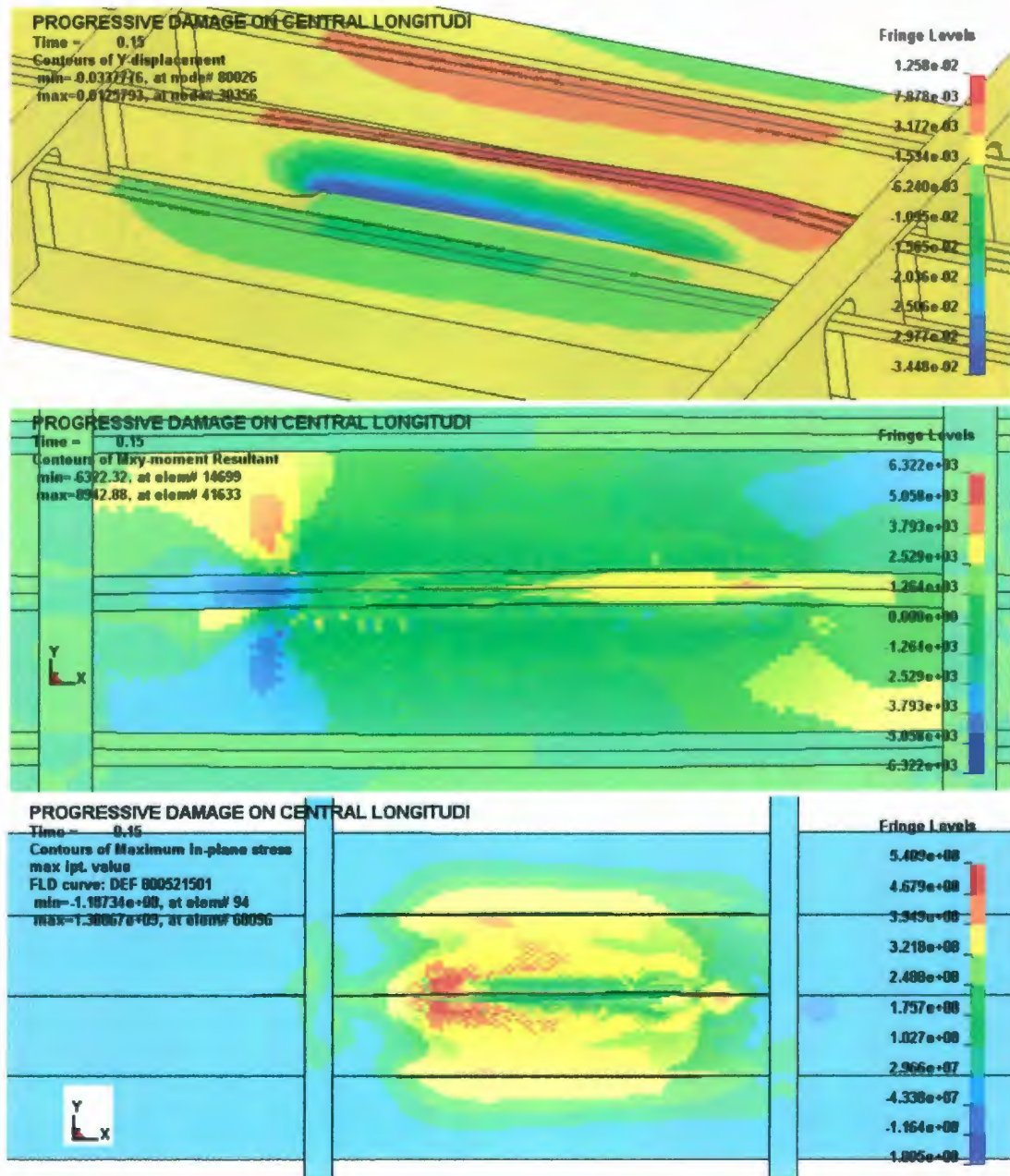


Figure 4-35: Load scenario 2: subsequent central stiffener buckling (top), M_{xy} moment (mid), and max in-plane stress (bottom): 5 cm load case.

4.2.3 Load scenario 3: progressive damage diagonally across longitudinals

This static load was applied at location 4 (see Figure 4-36), between the boundary structure and a longitudinal stiffener. The indenter was then simultaneously dragged 1.1176 m in the longitudinal direction and 1.050 m in the transverse direction (for a total diagonal distance of 1.553 m). The structure was then unloaded. Figure 4-36 depicts this scenario as well as the locations of the static and dynamic structural capacity comparisons (labelled “location 3” and “location 4”).

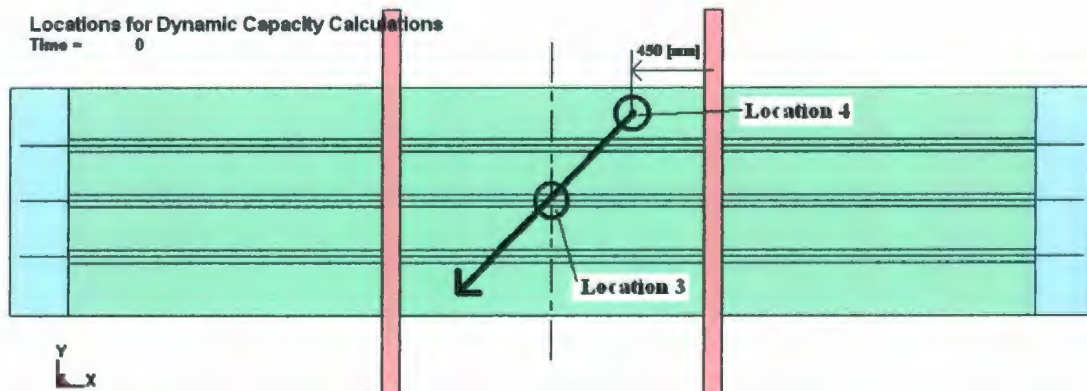


Figure 4-36: Load scenario 3: progressive damage across longitudinals and between transverses.

Results for the load cases simulated for this scenario are presented in the form of z-force reaction versus lateral displacement curves. The load-displacement results for the 0.2 and 0.5 cm load cases are given in Figure 4-37.

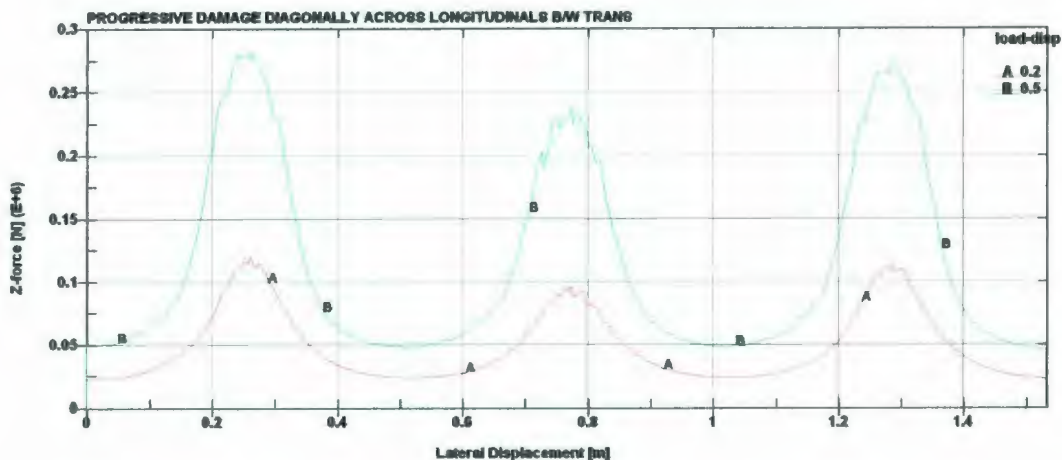


Figure 4-37: Load scenario 3: load-displacement curves for 0.2 and 0.5 cm load cases.

Observation of this plot shows that there are humps and hollows in the load-displacement curves. In each case, the middle hump is lower in magnitude than the other two, but the hollows are approximately equal. As well, both curves are essentially symmetric about the middle of the x-axis, indicating that the structural responses of these load cases are predominantly elastic. Indeed, there was very little plastic strain present in the 0.2 cm load case; the maximum plastic strain value was less than 0.35% plastic elongation. Plastic strain for the 0.5 cm load case was more prevalent, and its effects on the structural reaction are similar to load scenario 2 in that the plastic strain was established enough to cause asymmetric plate bending,²³ but the asymmetric bending reaction was small compared with the structure's elastic response.

²³ That is, the structure behind the indenter was sufficiently plastically deformed that it did not carry a bending moment, while the undeformed structure ahead of the indenter did.

The humps in Figure 4-37 represent structural reactions as the indenter encounters the longitudinal stiffeners during its lateral motion. The indenter crosses the first and last longitudinals at points equidistant from a transverse. It crosses the centre longitudinal directly in between two transverses (i.e. at the centre of the whole structure). The structure is stiffer near the transverses than in between them. Thus, the reactions near the transverses are dominated by shear forces, rather than bending. The centre of the structure is less stiff, allowing more bending to occur. This difference in stiffness based on longitudinal location accounts for the difference in the magnitude of the humps in Figure 4-37.

The load-displacement curves for the first four load cases (again the 10 cm load case added little value to the plot) are given in Figure 4-38. Note that unlike the 0.2 and 0.5 cm load cases, the curves for the 2 and 5 cm load cases are not symmetric. The humps for the 2 cm load case all have approximately the same magnitude, but the magnitudes of the start and finish loads are different. The humps for the 5 cm load case actually increase in height, and again the magnitudes of the start and finish loads are different.

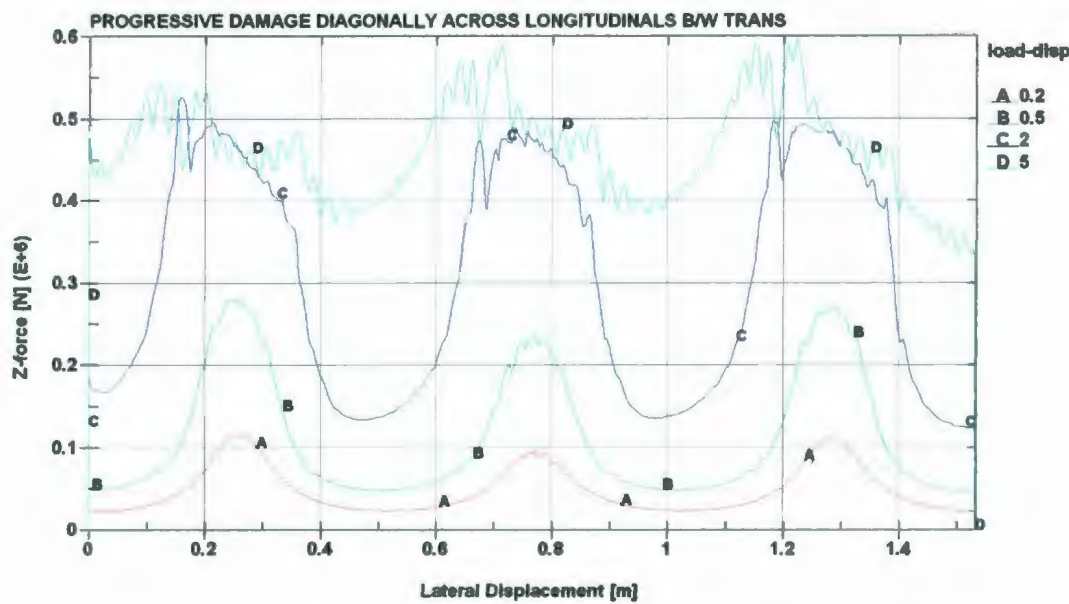


Figure 4-38: Load scenario 3: load-displacement curves for 0.2 to 5 cm load cases.

This figure suggests that upon commencement of the dynamic load, the capacity of the structure decreased for the 2 and 5 cm load cases (as in the above load scenarios).

The following capacity comparisons are for location 4. The static and dynamic loads for the 0.2 cm load case are identical at 24 kN, indicating no dynamic decrease in structural capacity. The static and dynamic loads for the 0.5 cm load case are 51 kN, and 46.5 kN, respectively; indicating a 9% decrease in structural capacity. The static and dynamic loads for the 2 cm load case are 188 kN, and 125 kN, respectively; indicating a 33.5% decrease in structural capacity. The static and dynamic loads for the 5 cm load case are 487 kN, and 347 kN, respectively; indicating a 28.5% decrease in structural capacity.

The following capacity comparisons are for location 3. The static and dynamic loads for the 0.2 cm load case are 111 kN, and 92 kN, respectively; indicating a 17% decrease in structural capacity. The static and dynamic loads for the 0.5 cm load case are 249 kN, and 230 kN, respectively; indicating a 7.5% decrease in structural capacity. The static and dynamic loads for the 2 cm load case are 551 kN, and 470 kN, respectively; indicating a 14.5% decrease in structural capacity. The static and dynamic loads for the 5 cm load case are 927 kN, and 550 kN, respectively; indicating a 40.5% decrease in structural capacity.

The structural mechanisms causing the decrease in dynamic structural capacity are a combination of those outlined in load scenarios 1 and 2. As the indenter diagonally traverses the hull plating, it alternately encounters the “between longitudinal” and “along longitudinal” structural mechanisms. In addition to these mechanisms, and depending on the indentation depth, collision between the side surface of the indenter and a longitudinal was observed.

This collision mechanism was observed for the 5 cm load case, where collisions with the second and third longitudinals were observed. The maximum plastic strain for the 5 cm load case was 94% plastic elongation, and the average was approximately 43% plastic elongation. Observation of the plastic strain suggests that the hull plating would have torn just prior to collision with each of the longitudinal stiffeners. Further, the increase in magnitude of successive humps in the load-displacement curve for this load case increase because of this collision mechanism. Investigation suggested the following explanation

for the increase in the z-force shown in the second and third humps in the load-displacement curve for the 5 cm load case: As plastic damage to the structure increased with lateral indenter displacement, the hull plating began to deform excessively around the indenter. Thus, the plate progressively weakened and therefore transferred less load to the longitudinal stiffeners. When the indenter reached the second (and third) longitudinal stiffener, the longitudinal stiffener was relatively undeformed in the z-direction, causing the side of the indenter to collide with the longitudinal stiffener's web. This side impact pushed the web forward, then up and over the indenter as it passed; thus causing the increased z-force load present in the second and third humps in the load-displacement curve. Because it is likely that the hull plating would have failed under these conditions, further structural mechanisms for the 5 cm load case are not explored below.

For 2 cm load case, it was observed that membrane stresses are present primarily when the indenter is in the “between longitudinals” sections of this load scenario. The highly stressed areas observed in the previous load scenarios were present for this scenario as well. In addition, the membrane stress field was separated into two regions – one region ahead of the indenter’s lateral path, the other behind it. These regions (shown in yellow in Figure 4-39) are separated by a band of lower stress (shown in green) that passes diagonally through the corners of the indenter.

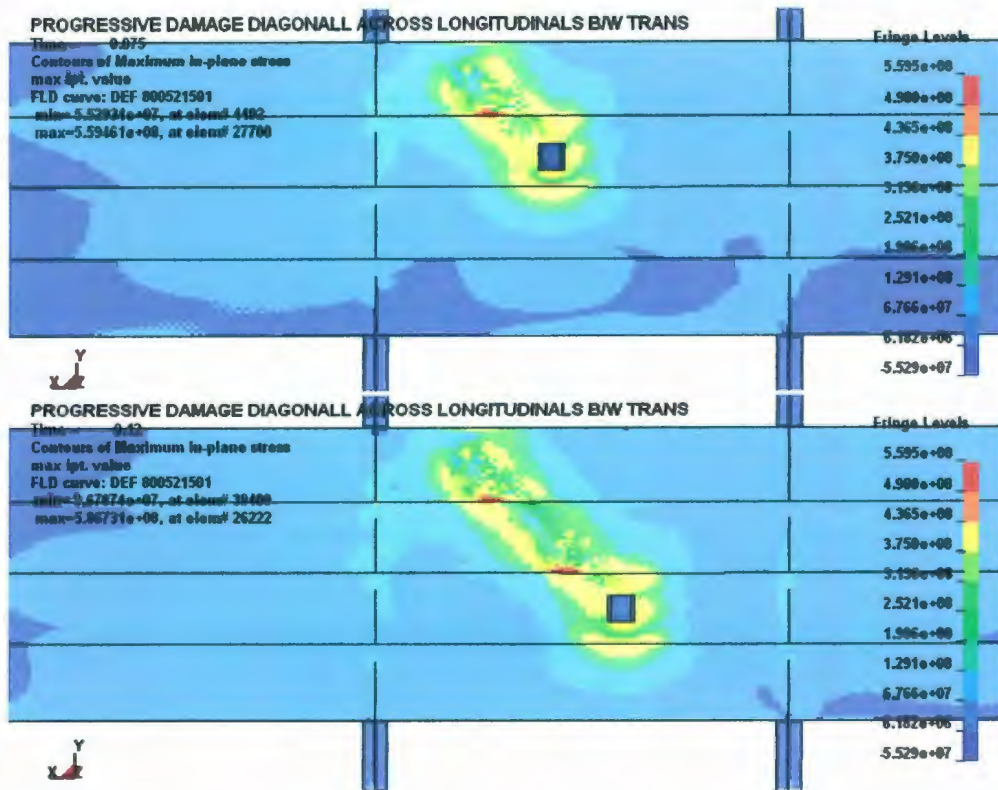


Figure 4-39: Load scenario 3: maximum in-plane stresses: 2 cm load case.

The bending reaction of the plate for the 2 cm load case was also slightly different for this load scenario than for the previous ones. Symmetric bending in two directions was observed (as per usual) for the static load, but the M_{xy} bending distribution for the dynamic load exhibited three “lobes” emanating from the corners of the indenter, rather than the two “lobes” observed previously. This indicates that bending in two directions occurs around the two “ahead” sides of the indenter, but not around the two “behind” sides of the indenter (note that because the indenter is translating diagonally, one of its corners is the leading part instead of one of its sides, as in the above load scenarios; shown in Figure 4-40). These new bending phenomena are shown in Figure 4-41.

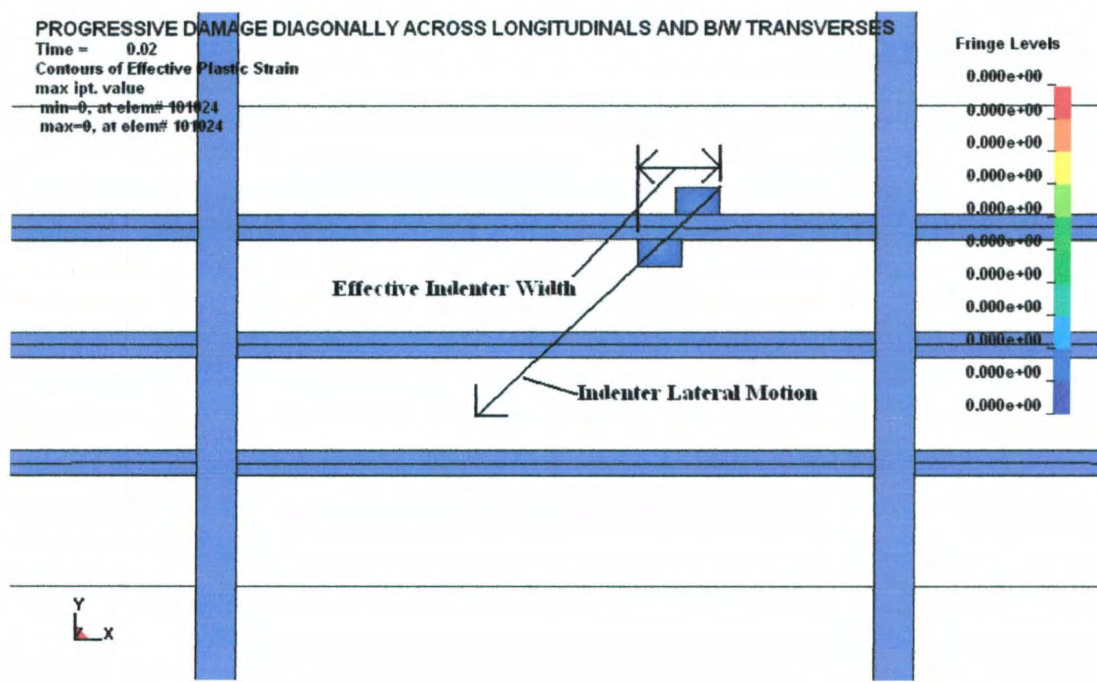


Figure 4-40: Load scenario 3: indenter lateral motion and effective width (plate not shown).

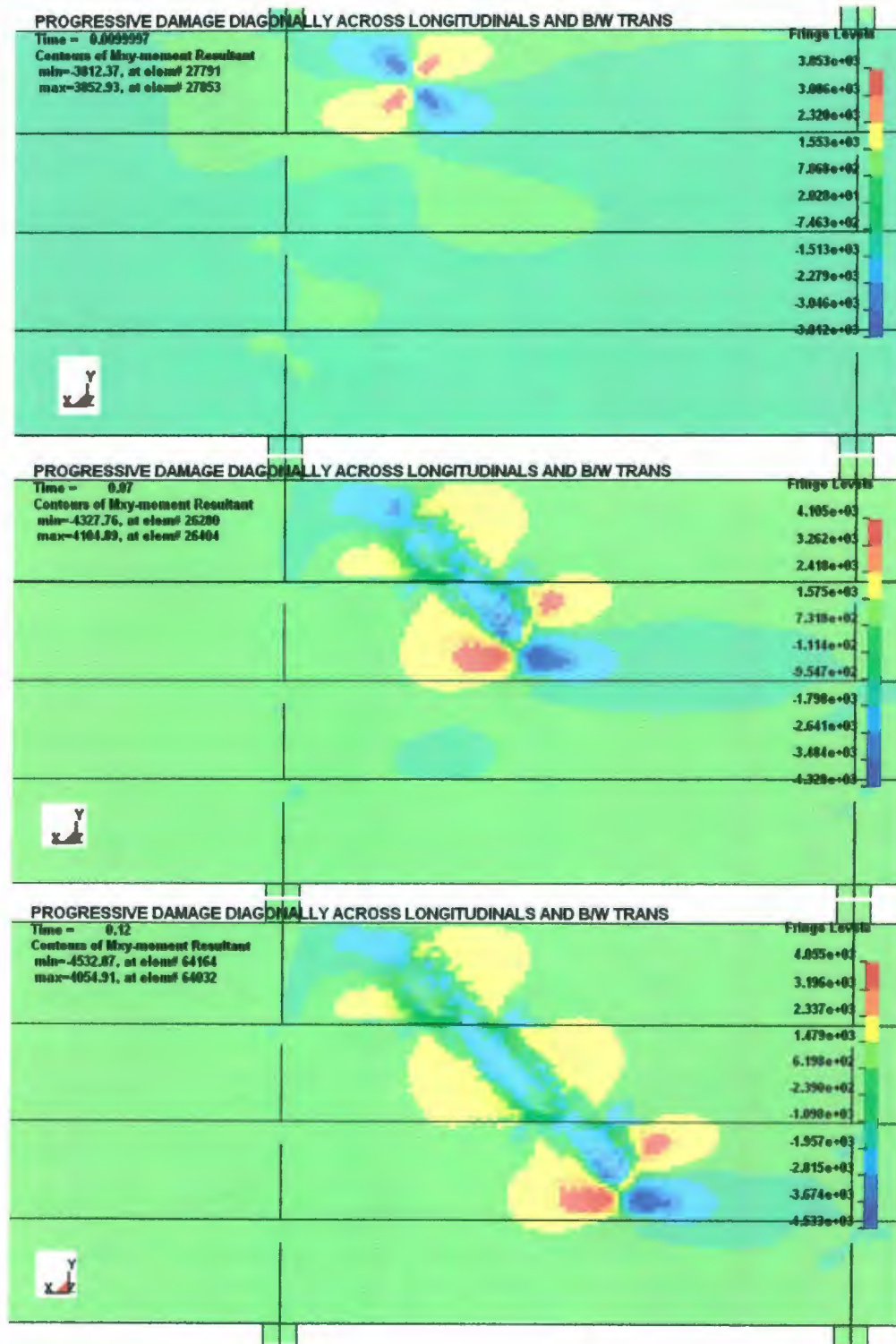


Figure 4-41: Load scenario 3: M_{xy} bending moment distribution: 2 cm load case.

As in load scenario 2, longitudinal stiffener buckling occurred for the 2 and 5 cm load cases. Based on the large grillage experiments, stiffener buckling would not occur under these loading conditions if the loads were statically applied. A plot of the residual y-direction displacements (see Figure 4-42) shows the locations of the stiffener buckling, and the path of the indenter. The magnitude of the residual y-displacement is less for the central longitudinal stiffener than for the others. This is due to the structure being less stiff in the centre than near the transverse frames. A greater part of the load is absorbed in bending near the centre, resulting in less stiffener buckling at this point.

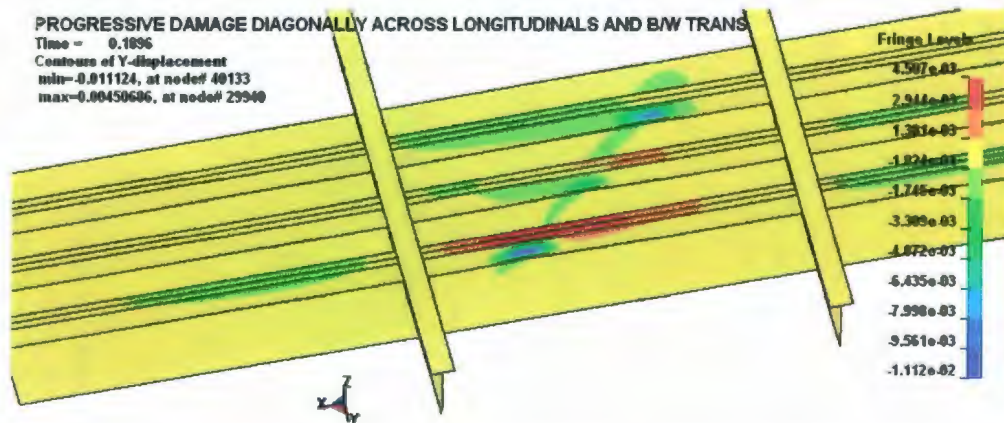


Figure 4-42: Load scenario 3: residual y-direction displacements: 2 cm load case.

4.3 Progressive Damage across Transverses

The second part of this study extends the three load scenarios outlined in section 4.2 to include direct application of progressive damage to the transverse stiffeners. All load scenarios in this category begin with the static load at a longitudinal (x-direction) distance of 475 mm away from the boundary structure at the end of the large grillage, and end with removal of the load at a distance of 475 mm away from the boundary structure at the other end of the grillage. The total change in longitudinal position of the indenter for each load scenario in this section is 5.1176 m. The indenter encounters both of the transverse stiffeners over this longitudinal span.

4.3.1 Load scenario 4: progressive damage between longitudinals and across transverses

This load scenario is an extension of load scenario 1 to include progressive loading of the transverse stiffeners. The large grillage model is statically loaded at location 5 (shown in Figure 4-43). The indenter is then dragged 5.1176 m laterally in the longitudinal direction to the point of unloading. Figure 4-43 depicts this scenario as well as the locations of the static and dynamic structural capacity comparisons (labelled “location 1”, “location 5, and “location 6”).

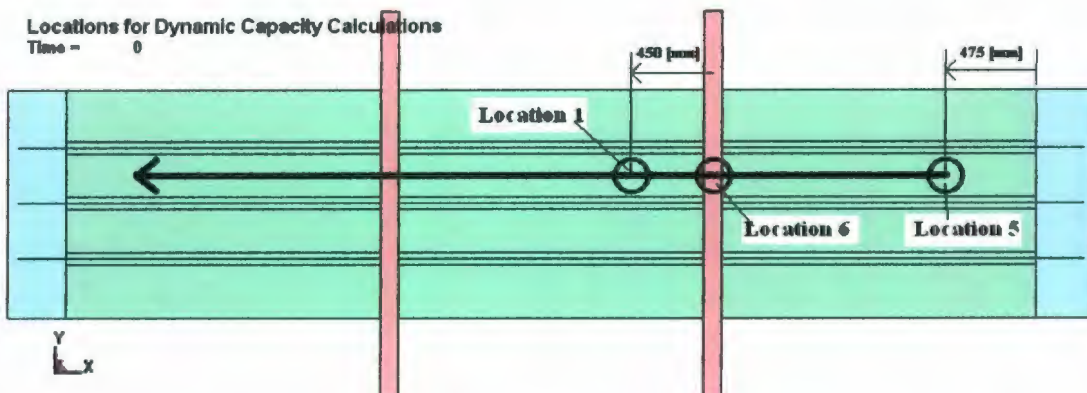


Figure 4-43: Load scenario 4: progressive damage between longitudinals and across transverses.

Results of the load cases simulated for this scenario are presented in the form of z-force reaction versus lateral displacement curves. Of the five load cases simulated, only the 0.2, 0.5, and 2 cm load cases are presented below. The load-displacement results for the 5 and 10 cm load cases are not presented because the structural reaction of the hull plating for these load cases is not realistic due to excessive finite element straining²⁴ near the transverse frames. This excessive straining is due to a structural mechanism similar to the collision mechanism described in load case 3. That is, the effects of the dynamic load are such that the z-deformation (i.e. normal to the hull plating) of the part of the transverse frame adjacent to the hull plating is small just before it encounters the indenter. For the 5 cm load case this z-deformation is only 3.4 mm, compared with the indenter's z-displacement of 40 mm above the top surface of the hull plating (i.e. 50 mm indentation through a 10 mm thick plate). This behaviour is illustrated in Figure 4-44. Note that the

²⁴ As mentioned above, material failure was not included in the numerical model, allowing for the possibility of infinite strain to occur.

boundary structure, the longitudinal stiffeners, and the indenter have been hidden in this figure.

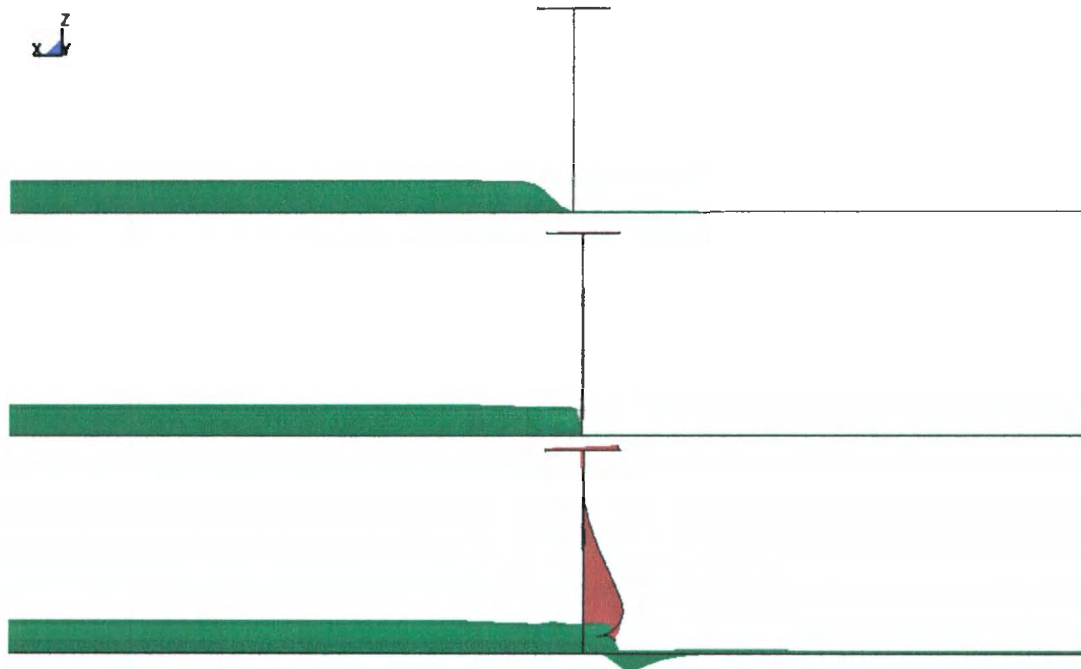


Figure 4-44: Load scenario 4: collision between the indenter and the transverse stiffener: 5 cm load case (z-deformation shown).

The load-displacement results for the 0.2 and 0.5 cm load cases are given in Figure 4-45, and again in Figure 4-46. The humps in Figure 4-45 correspond to the encounters between the indenter and the transverse frames. Figure 4-46 has a limited y-axis that allows for better examination of the structural response before and after these encounters.

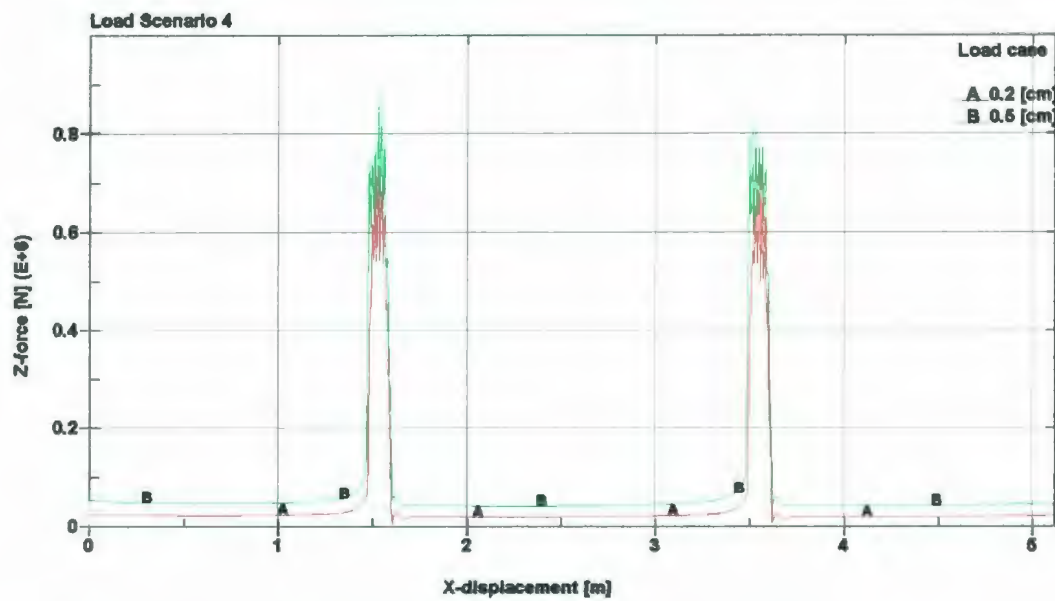


Figure 4-45: Load scenario 4: load-displacement curves for 0.2 and 0.5 cm load cases.

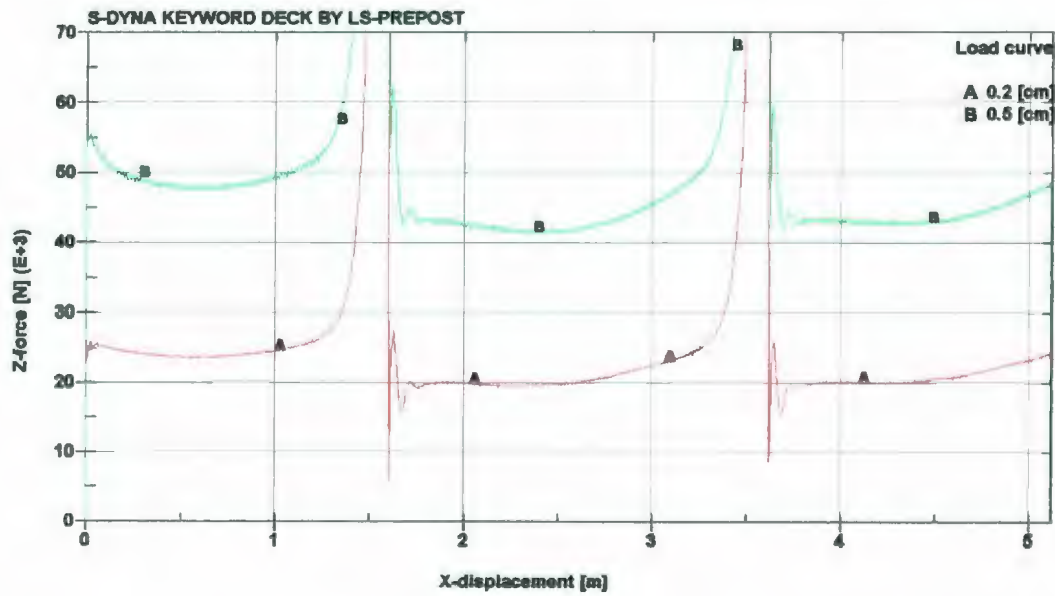


Figure 4-46: Load scenario 4: load-displacement curves for 0.2 and 0.5 cm load cases (zoomed).

Before the first transverse stiffener encounter, Figure 4-46 exhibits a “bowl shaped” load curve, as seen in load scenario 1. There is very little plastic damage for either load case. The maximum plastic elongation for the 0.2 cm load case is 0.16%, and 1.45% for the 0.5 cm load case. During the first transverse frame encounter, however, the z-force reaction increases dramatically, and the maximum plastic elongation rises to 7.2% plastic elongation for the 0.2 cm case (top of Figure 4-47), and 10.0% for the 0.5 cm load case (bottom of Figure 4-47). Most of this new plastic damage occurred at the intersection between the hull plating and the transverse stiffener.

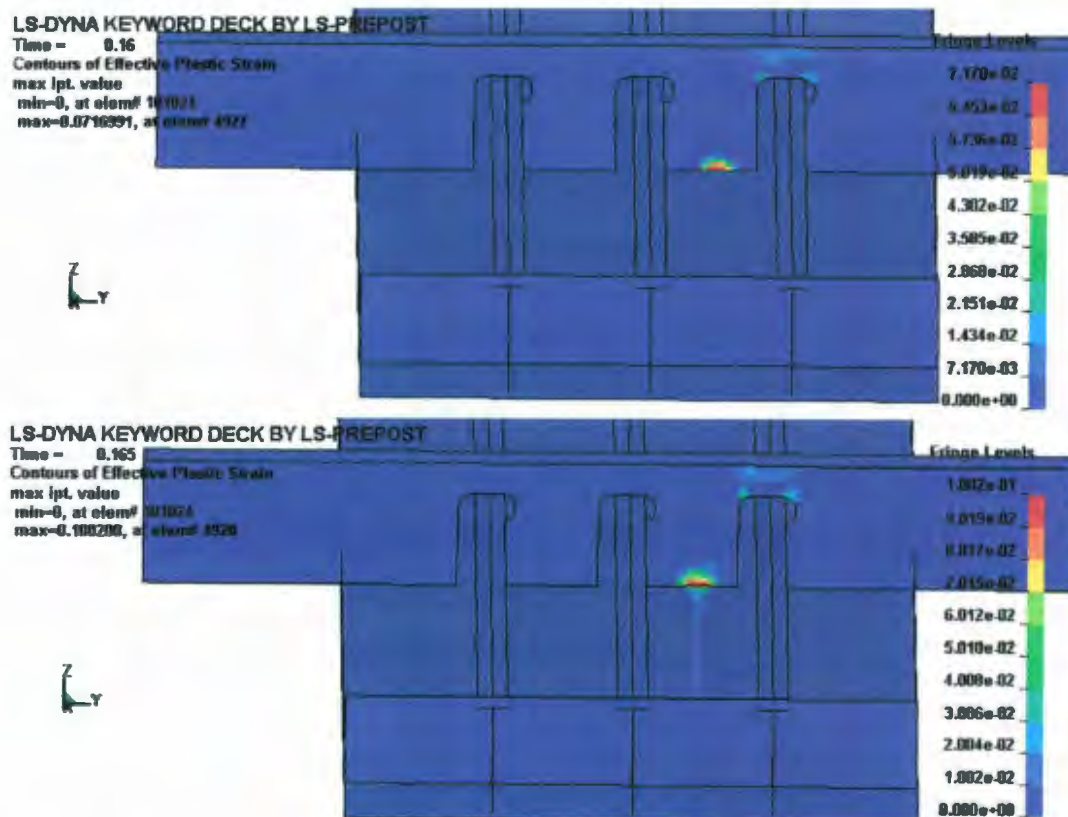


Figure 4-47: Load scenario 4: plastic damage at first transverse frame encounter: 0.2 (top) and 0.5 cm (bottom) load cases.

After the first transverse frame encounter, the load drops off so quickly that an inertial effect occurs; similar to that observed during the static loading of load scenario 2, for 0.2 and 0.5 cm load cases. This inertial reaction quickly dampens out. The plastic damage from the first transverse encounter has a noticeable effect on the load response of the structure between the transverse stiffeners. That is, the structure near location 1 shows a lower structural capacity than the structure symmetrically opposite to it (these capacities would be equal if there was no plastic damage, due to the symmetry of the structure). This indicates that the plastic damage to the transverse frame has decreased the capacity of the structure immediately adjacent to it. Further along the structure, between the transverse frames, the dynamic capacity increases. This is because the effects of the plastic damage to the transverse stiffener fade with increased lateral distance, and the shear force reaction of the structure increases as the indenter approaches the undamaged transverse stiffener. The results of the second transverse stiffener encounter, and the subsequent structural reaction, are very similar to the first.

From load scenario 1, we know that the static capacity of the structure at location 1 is approximately 25 kN for the 0.2 cm load case, and approximately 54 kN for the 0.5 cm load case. From Figure 4-46, the dynamic structural capacity at location 1²⁵ is 20 kN for the 0.2 cm load case, and 42 kN for the 0.5 cm load case. Thus, the dynamic decrease in structural capacity (including the effects of the damaged transverse stiffener) is 20% for the 0.2 cm load case and 22% for the 0.5 cm load case. These values are significant not only by themselves, but also because they are much larger than their counterparts in load

²⁵ Location 1 is at a x-displacement of 2.0 m in Figure 4-46.

scenario 1²⁶. Thus, plastic damage to the transverse stiffener can have a dramatic effect on dynamic structural capacity.

For location 5, from Figure 4-46 the static structural capacities for 0.2 and 0.5 cm load cases are approximately 24 kN and 54 kN, respectively. The dynamic structural capacities are 24 kN for the 0.2 cm load case, and 48 kN for the 0.5 cm load case. Therefore, the dynamic decreases are 0% and 11% for the 0.2 and 0.5 cm load cases, respectively. The 0% value indicates that the plastic damage to the transverse stiffeners has no effect on the structural capacity near the boundary structure for the 0.2 cm load case.

A separate simulation was conducted to discern the static structural capacity at location 6. The static z-force versus z-displacement curve²⁷ for this simulation is given in Figure 4-48. For location 6, the static structural capacities for the 0.2 and 0.5 cm load cases are approximately 500 kN and 762 kN, respectively. The dynamic structural capacities (i.e. the hump values from Figure 4-45) are 635 kN for the 0.2 cm load case, and 731 kN for the 0.5 cm load case. Therefore, the dynamic decreases are -27% and 4% for the 0.2 and 0.5 cm load cases, respectively. The 0.2 cm load case exhibits a dynamic *increase* in structural capacity of 27%. It is suspected that this is not a legitimate increase, but an

²⁶ The dynamic decrease in structural capacity for the 0.2 cm load case in load scenario 1 was 0%; and it is 20% for this load scenario. The dynamic decrease in structural capacity for the 0.5 cm load case was 9% in load scenario 1, and the value is now 22%.

²⁷ Note that because this was a simulation of static load, the indenter did not move laterally along the hull plating; only into it.

artefact of an inertial effect as seen above in other load scenarios for this very small indentation.

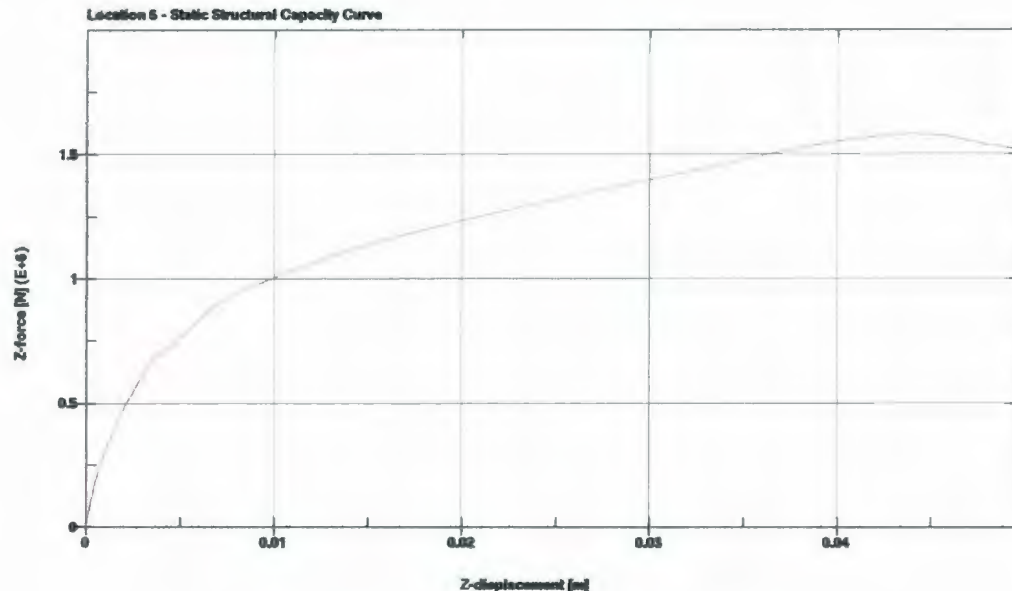


Figure 4-48: Location 6 static structural capacity curve.

The structural mechanisms present for these load cases were similar to those of load scenario 1 for the 0.2 and 0.5 cm load cases. The bending reaction was generally symmetric in two directions, and the membrane stresses were generally symmetric for both load cases. Further, there was no transverse stiffener buckling for the 0.2 or the 0.5 cm load cases.

4.3.1.1 Further investigation

The load curve for the 2 cm load case is given in Figure 4-49.

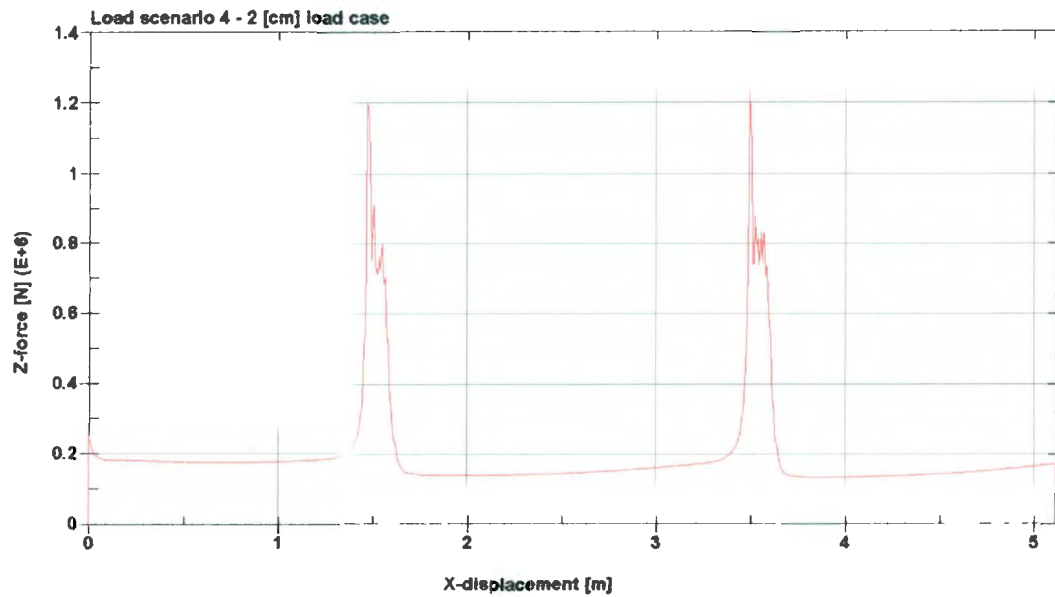


Figure 4-49: Load scenario 4: load-displacement curve: 2 cm load case.

Two things are noticeably different from Figure 4-45; they are the initial drop in structural capacity upon commencement of the dynamic load, and the difference in the shape of the humps; specifically, a load drop occurs about halfway through each hump. This load drop is due to the transverse frame buckling shown in Figure 4-50. The maximum deflection of the buckling in the x-direction is 2.0 cm, as shown by the red fringes in Figure 4-50. Note that the boundary structure, the longitudinal stiffeners, and the indenter are hidden in this figure to allow better observation of the stiffener buckling. Note also that the indenter's position in this figure is directly below the transverse stiffener. It is important to note further that the transverse stiffener does not buckle under a 2 cm static load.

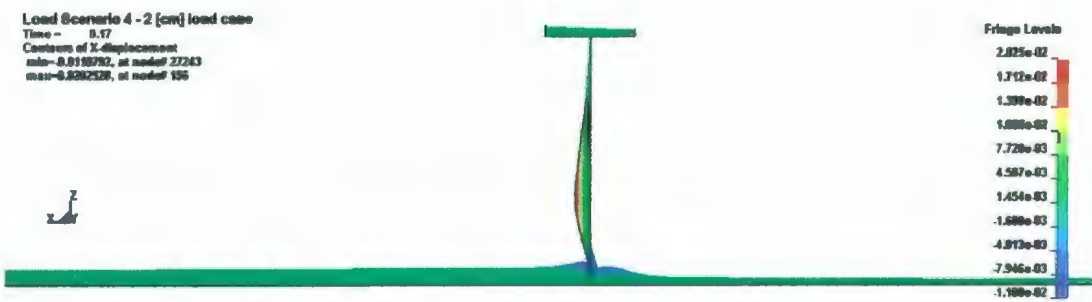


Figure 4-50: Load Scenario 4: transverse frame buckling (dynamic load): 2 cm load case (x-displacement fringes shown).

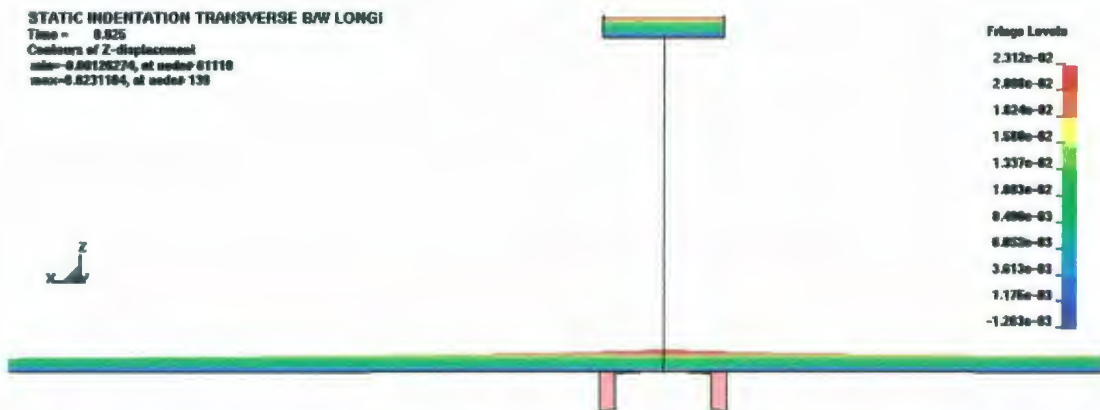


Figure 4-51: Static loading of transverse stiffener at “between longitudinals” location: z-displacement fringes shown.

A similarity to Figure 4-45 is that plastic damage to the transverse frames has decreased the structural capacity of the adjacent structure (i.e. location 6). The static capacity for location 6 at a 2 cm indentation is 1.23 MN (from Figure 4-48). The dynamic capacity²⁸ is 758 kN (from Figure 4-49); therefore the dynamic decrease in structural capacity at location 6 for the 2 cm load case is 38%. For location 1, the static capacity (from load scenario 1) is 244 kN and the dynamic capacity (from Figure 4-49 at x-displacement

²⁸ Taken from the post buckled part of the hump.

equals 2 m) is 142 kN. Therefore, the dynamic decrease in structural capacity for the 2 cm load case at location 1 is 42%. For location 5, the static capacity (from Figure 4-49) is 250 kN and the dynamic capacity is 174 kN. Therefore, the dynamic decrease in structural capacity for the 2 cm load case at location 5 is 30%.

4.3.2 Load scenario 5: progressive damage along the central longitudinal and across transverses

This load scenario is an extension of load scenario 2 to include progressive loading of the transverse stiffeners. The large grillage model is statically loaded at location 7 (shown in Figure 4-52). The indenter is then dragged 5.1176 m laterally in the longitudinal direction to the point of unloading. Figure 4-52 depicts this scenario as well as the locations of the static and dynamic structural capacity comparisons (labelled “location 2”, “location 3”, “location 7, and “location 8”).

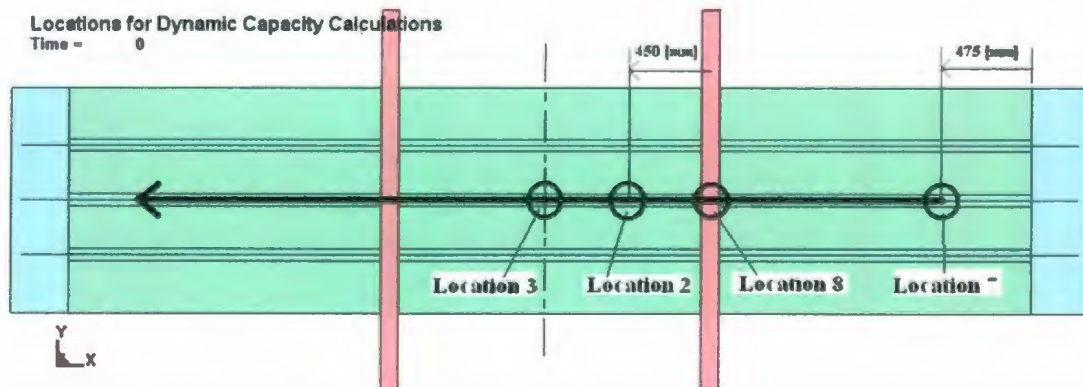


Figure 4-52: Load scenario 5: progressive damage along central longitudinal and across transverses.

Results of the load cases simulated for this scenario are presented in the form of z-force reaction versus lateral displacement curves. As in load scenario 4, the 5 and 10 cm load cases are not presented because of the excessive strain observed during indenter-transverse frame collisions.

The load-displacement results for the 0.2, 0.5, and 2 cm load cases are given in Figure 4-53. As in load scenario 4, the humps in this figure correspond to the encounters between the indenter and the transverse frames. Figure 4-54 has a limited y-axis that allows for better examination of the structural response before and after these encounters.

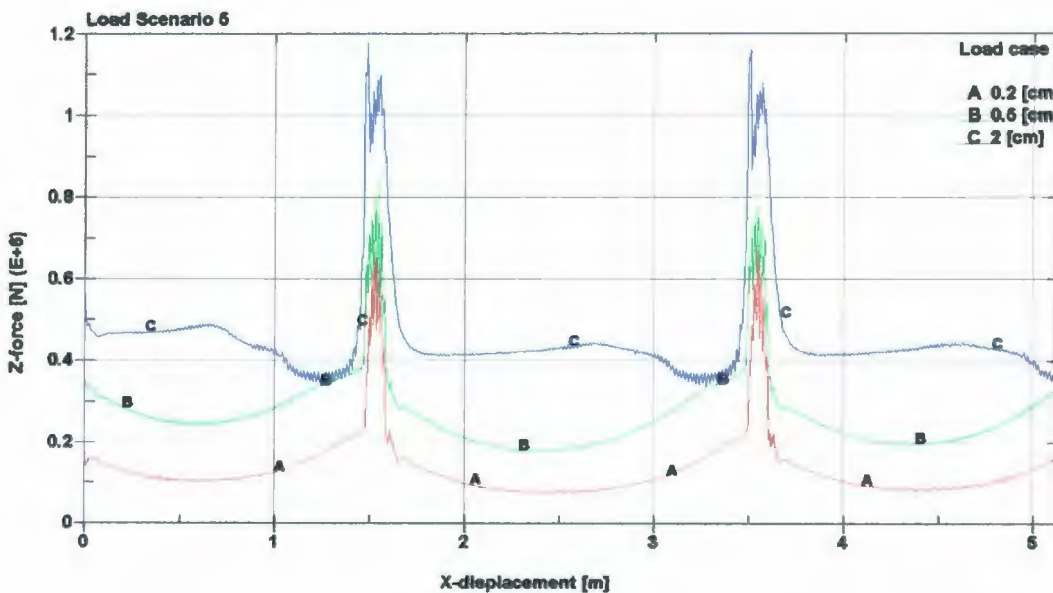


Figure 4-53: Load scenario 5: load-displacement curves for 0.2, 0.5, and 2 cm load cases.

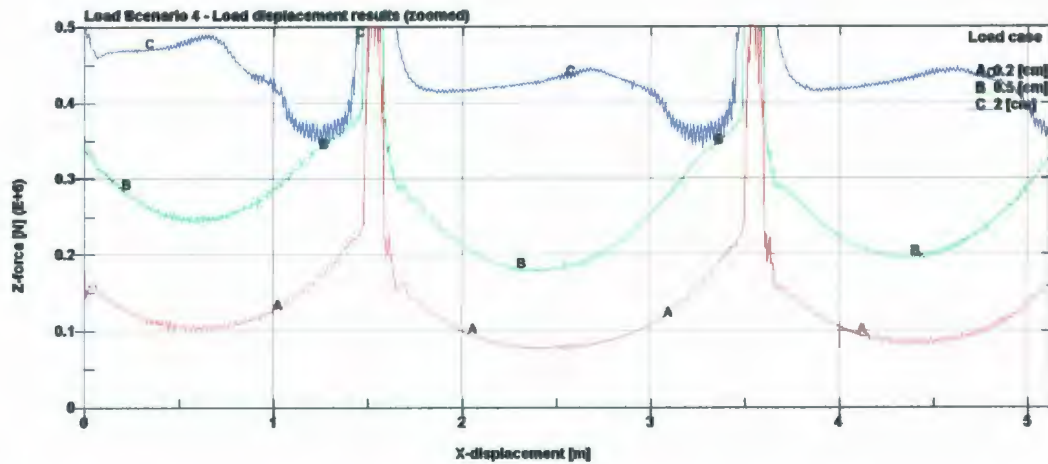


Figure 4-54: Load scenario 5: load-displacement curves for 0.2, 0.5, and 2 cm load cases (zoomed).

The inertial vibration observed in load scenario 2 for the 0.2 and 0.5 cm load cases is present here at the commencement of the dynamic load for the 0.2 cm load case only. It is less pronounced than in load scenario 2, and is quickly damped out. A “bowl shaped” load curve exists for the 0.2 and 0.5 cm load curves, up to the first transverse frame encounter (i.e. hump in the load curve). There is very little plastic structural damage for this portion of the curve for the 0.2 cm load case. There is more significant plastic damage for the 0.5 cm load case. As the indenter nears the transverse frame, the plastic damage rises from a maximum of 11% plastic elongation, to a maximum of 13.6%. There is a slight flattening of the load curve for the 0.5 cm load case that corresponds with this increase in plastic damage. As the indenter encounters the first transverse stiffener, there is a large increase in the z-force reaction. No transverse stiffener buckling occurs for the 0.2 cm load case, and very slight transverse stiffener buckling for the 0.5 cm case (the transverse stiffener web buckled less than 1.5 mm out of the vertical plane).

The “between transverse frames” sections of the 0.2 and 0.5 cm load curves are also “bowl shaped,” however, the left side (i.e. near location 2) has a noticeably lower load magnitude than the right side. As in load scenario 4, this indicates that the plastic damage to the transverse frame has lowered the capacity of adjacent structure. As the indenter nears the second transverse frame, the slight flattening of the load curve reappears for the 0.5 cm load case, as well as the 0.2 cm load case (to a much smaller degree). This flattening is again caused by increased plastic damage to the longitudinal stiffener web and hull plating at their intersection. These results show that plastic damage occurs readily near a transverse frame during a dynamic load. The second hump and remaining section of the 0.2 and 0.5 cm load cases are similar to the first hump and central section.

The load-curve for the 2 cm load case is quite different from the other curves. There is an initial drop in load upon commencement of the indenter’s lateral motion, followed by a slow rise in load, followed by a slow drop in load until the encounter with the transverse stiffener. The initial load drop is consistent with the results of load scenario 2, for the 2 cm load case, however, the subsequent rise in load is not. Significant plastic damage to the longitudinal stiffener web at location 7 during the static load was present in this case (shown in Figure 4-55). It is believed that the extent of plastic damage is due to the proximity of location 7 to the 30 mm thick steel boundary structure. This location is necessarily much stiffer than the static load location for load scenario 2, and therefore a large extent of plastic damage resulted. It is theorized that the structures dynamic structural capacity increases with distance from this initial plastic damage, thereby explaining this rise in load. The subsequent gradual decrease in load, up to the encounter

with the transverse stiffener, occurs because the longitudinal stiffener buckles. The buckling increases as the indenter approaches the transverse stiffener. The extent of longitudinal stiffener buckling just before the transverse frame encounter is shown in Figure 4-56.

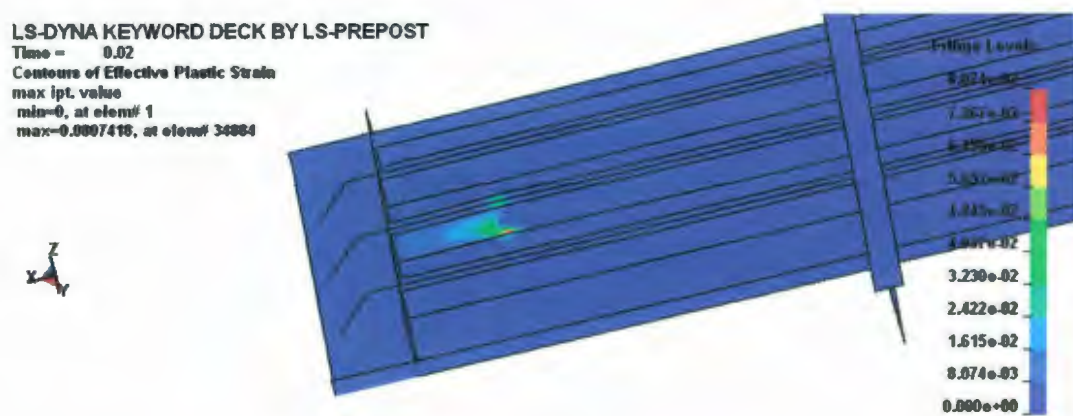


Figure 4-55: Load scenario 5: plastic damage extent for static load: 2 cm load case.

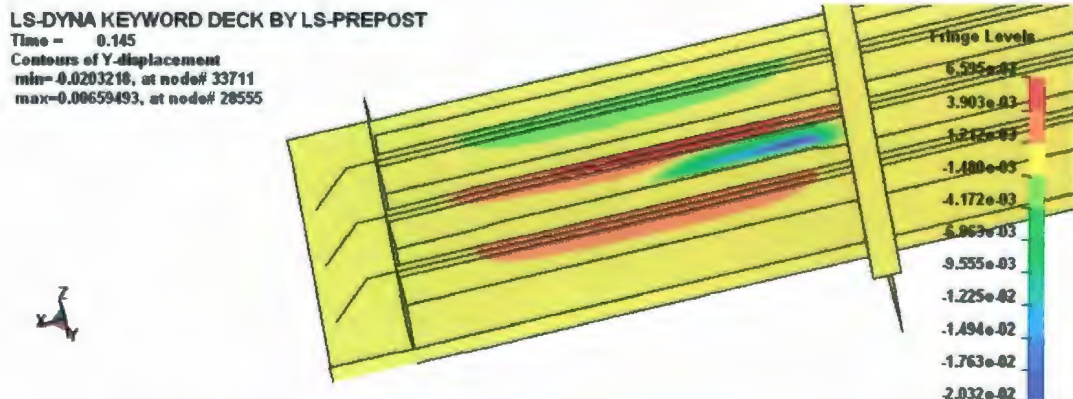


Figure 4-56: Load scenario 5: longitudinal stiffener buckling extent before transverse frame encounter: 2 cm load case.

As in load scenario 4, the transverse stiffener buckles during the encounter with the indenter; however, this time the geometry of the interaction is different. A “cut-out” is present in the transverse stiffener, as shown circled in Figure 4-57. Because of this cut-out, only approximately half the width of the indenter encounters the transverse stiffener. This reduced contact implies a reduced structural capacity, because less of the transverse stiffener is involved. In load scenario 4, for the transverse stiffener encounter, the difference between the initial “pre-buckled” load (i.e. the max “hump” value) and the following buckled load (i.e. the reduced “hump” value) is approximately 500 kN (from Figure 4-49). The difference for this load scenario (and this load case) is approximately 150 kN. This indicates that the transverse stiffener has a much lower stiffness at this “cut-out” location. Further, the overall structural reactions to the transverse stiffener encounters were of similar magnitude, for both load scenarios 4 and 5; indicating that the dynamic structural capacities are similar despite the “cut-out”.

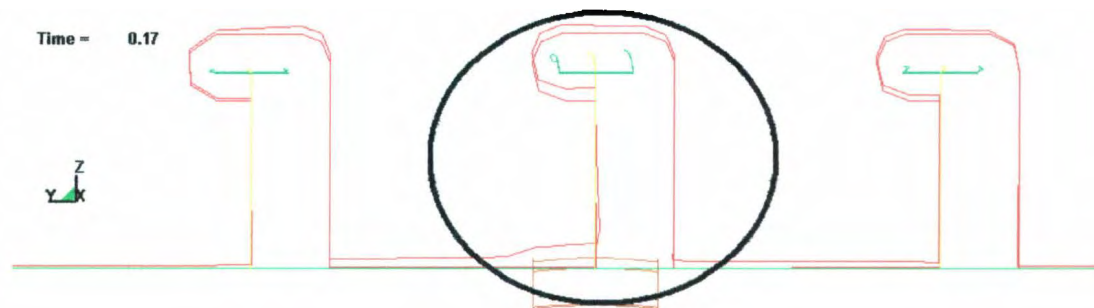


Figure 4-57: Load scenario 5: wireframe plot of cut-out and indenter-transverse frame interaction: 2 cm load case.

The reaction of the structure between the transverse stiffeners is similar to that of the structure at the start of the load curve. That is, the effect of plastic damage (in this case to the transverse stiffener) reduces with distance from the point of damage, causing a gradual increase in capacity. The capacity gradually decreases again as the indenter approaches the other transverse stiffener because the longitudinal stiffener buckles. The reaction of the rest of the structure is similar to the above.

The static structural capacity, dynamic structural capacity, and the resulting percentage decrease in structural capacity for each of the four locations shown in Figure 4-52 are given in Table 4-2, for each load case. Note that a separate simulation was performed to determine the static structural capacity at location 8. The static z-force versus z-displacement curve for location 8 is given in Figure 4-58. A similar curve for location 3 was presented for load scenario 3 in Figure 4-27.

Table 4-2: Structural capacities for load scenario 5.

Location	2			3			7			8		
	Load Case	Static [kN]	Dynamic [kN]	% Decrease	Static [kN]	Dynamic [kN]	% Decrease	Static [kN]	Dynamic [kN]	% Decrease	Static [kN]	Dynamic [kN]
0.2	167	101	39.5%	111	79	28.8%	183	159	13.1%	428	561	-31.1%
0.5	329	214	35.0%	249	183	26.5%	374	324	13.4%	748	696	7.0%
2	602	418	30.6%	550	437	20.5%	612	355	42.0%	1203	1057	12.1%

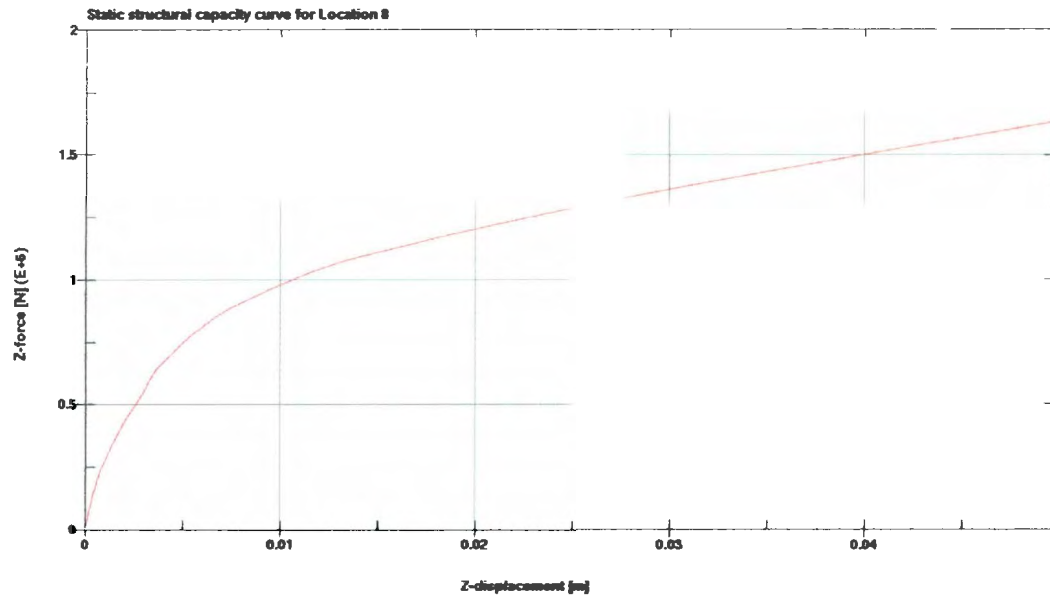


Figure 4-58: Location 8 static structural capacity curve.

4.3.3 Load scenario 6: progressive damage diagonally across longitudinals and transverses

This load scenario is an extension of load scenario 3 to include progressive loading of the transverse stiffeners. The large grillage model is statically loaded at location 9 (shown in Figure 4-59). The indenter is then simultaneously dragged laterally 5.1176 m in the longitudinal direction, and 1.050 m in the transverse direction (for a total diagonal distance of 5.224 m), to the point of unloading. Figure 4-59 depicts this scenario as well as the locations of the static and dynamic structural capacity comparisons (labelled “location 9” and “location 3”).

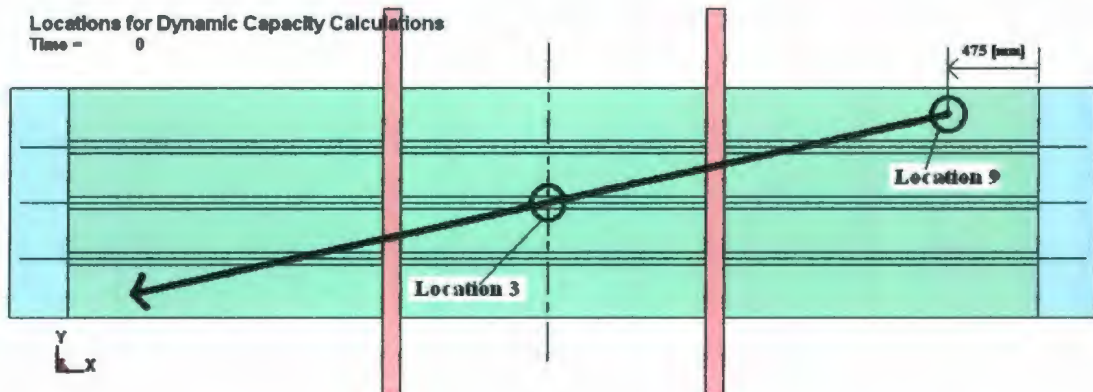


Figure 4-59: Load scenario 6: progressive damage diagonally across longitudinals and transverses.

Results of the load cases simulated for this scenario are presented in the form of z-force reaction versus lateral displacement curves. As in load scenario 4, the 5 and 10 cm load cases are not presented because of the excessive strain observed during indenter-transverse frame collisions.

The load-displacement results for the 0.2, 0.5, and 2 cm load cases are given in Figure 4-60.

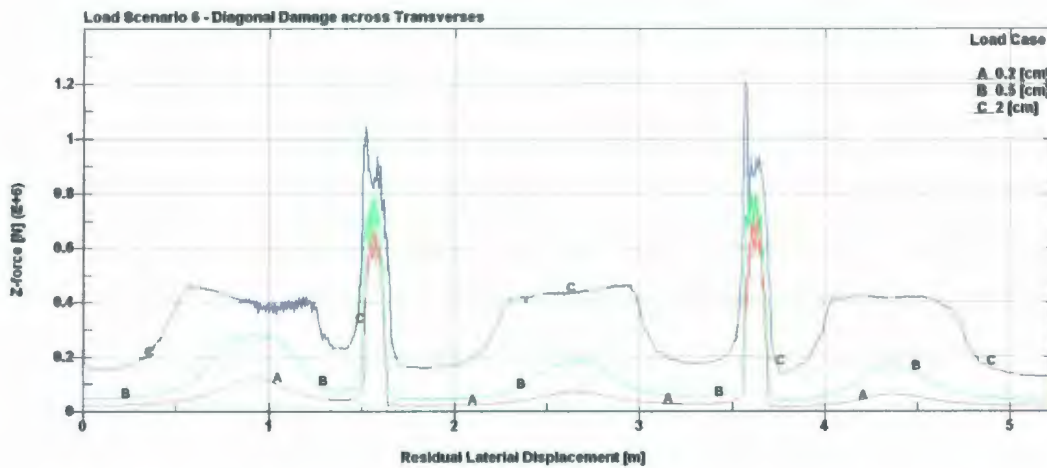


Figure 4-60: Load scenario 6: load-displacement curves for 0.2, 0.5, and 2 cm load cases.

A new hump is present for the initial section of these curves (i.e. before the indenter-transverse encounter), where there was previously a hollow for load scenarios 4 and 5. This hump corresponds with the indenter's proximity to the longitudinal stiffener closest to location 9. After the static load, the indenter steadily moves toward the indenter. Because the longitudinal stiffener is much stiffer than the adjacent hull plating, the structural reaction increases as proximity between the stiffener and the indenter decreases. The peak of these new humps for the 0.2 and 0.5 cm load cases coincides with the point where the indenter is directly below the longitudinal stiffener. For the 2 cm load case, the peak occurs before this point, because the structural reaction is limited by stiffener buckling; the effect of which is obvious in the above plot.

The phenomena present in load scenarios 4 and 5, as well as the new hump observed in this load scenario can be used to explain the mechanisms occurring in the load curves in Figure 4-60.

As in the other load scenarios, the first large magnitude hump corresponds with the first indenter-transverse encounter. Like load scenario 5, the indenter encounters the transverse at one of its longitudinal stiffener cut-outs. Unlike load scenario 5, this part of the cut-out is not supported by an attached longitudinal stiffener (see Figure 4-61); however, the structural capacity at this point is very similar to load scenarios 4 and 5, suggesting that the transverse stiffener provides the majority of the structural stiffness at this location.

LS-DYNA KEYWORD DECK BY LS-PREPOST
Time = 0.17

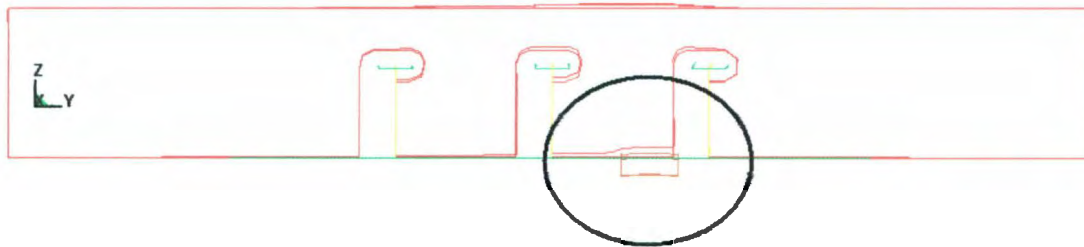


Figure 4-61: Load scenario 6: wireframe plot of cut-out and 1st indenter-transverse frame interaction: 2 cm load case.

After the indenter-transverse encounter, there is a drop in load for all scenarios caused by plastic damage to the transverse – as occurred in load scenarios 4 and 5. Following this is a gradual increase in structural capacity that is partly due to the increasing distance from

the plastic damage, and the decreasing distance to the central longitudinal stiffener. As in the initial part of the load curves, as the indenter nears the longitudinal stiffener, the structural reaction increases due to the increased structural stiffness. For the 0.2 and 0.5 cm load cases, this reaction is very similar to the initial part of their load curves. For the 2 cm load case, the reaction is different in that the load does not decrease after the onset of longitudinal stiffener buckling. This is due to the prior extensive plastic damage to the transverse stiffener as well as the increased overall flexibility of the structure at this central location. As the proximity between the indenter and this damage increases, so too does the structural reaction. Further, the extent of buckling is much less than before, indicating that it is as much a limiting factor. The increased flexibility allows the entire structure to deflect in the z-direction more than before, allowing increased bending and membrane reactions in the hull plating.

The second indenter-transverse encounter hump is larger in magnitude than the first because the encounter occurred between two cut-outs (see Figure 4-62). This meant that more of the transverse stiffener was involved in the contact, providing a stiffer reaction.

LS-DYNA KEYWORD DECK BY LS-PREPOST
Time = 0.365

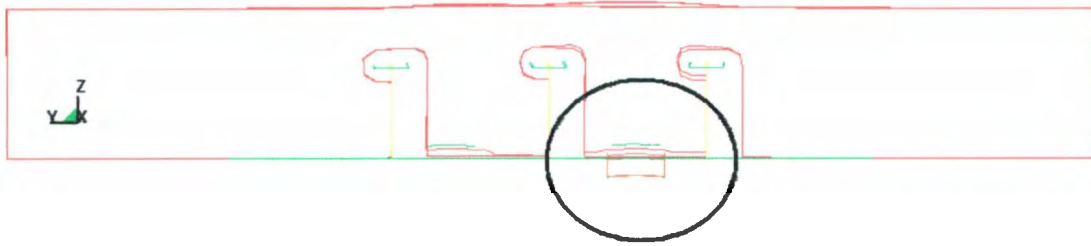


Figure 4-62: Load scenario 6: wireframe plot of cut-out and 2nd indenter-transverse frame interaction: 2 cm load case.

The subsequent structural reactions are explained similarly.

Comparisons between static and dynamic structural capacities were made for locations 9 and 3, and are given in Table 4-3.

Table 4-3: Structural capacities for load scenario 6.

Location	3			9		
	Load Case	Static [kN]	Dynamic [kN]	% Decrease	Static [kN]	Dynamic [kN]
0.2	111	72	35.1%	18	14	24.1%
0.5	249	181	27.2%	47	35	25.6%
2	550	434	21.1%	188	108	42.7%

4.4 Progressive Damage Parallel with Transverses

The third part of this study explores progressive damage parallel to the transverse stiffeners. Specifically, two load cases are considered: the first case considers progressive damage between the transverse stiffeners at a position equidistant from each (i.e. across the longitudinal centre of the structure); and the other case considers progressive damage along a transverse stiffener. All load scenarios in this category begin with the static load in the same transverse (y-direction) distance as the diagonal load scenarios 3 and 6, and end at a symmetrically opposite position on the other side of the structure. The total change in transverse position of the indenter for each load scenario in this section is 1.050 m. The indenter encounters all of the longitudinal stiffeners over this transverse span.

4.4.1 Load scenario 7: progressive damage between transverse stiffeners

This load scenario explores progressive damage between transverse stiffeners at the longitudinal centre of the structure. The large grillage model is statically loaded at location 10 (shown in Figure 4-63), the indenter is then dragged 1.050 m in the transverse direction to the point of unloading. Figure 4-63 depicts this scenario as well as the locations of the static and dynamic structural capacity comparisons (labelled “location 10” and “location 3”).

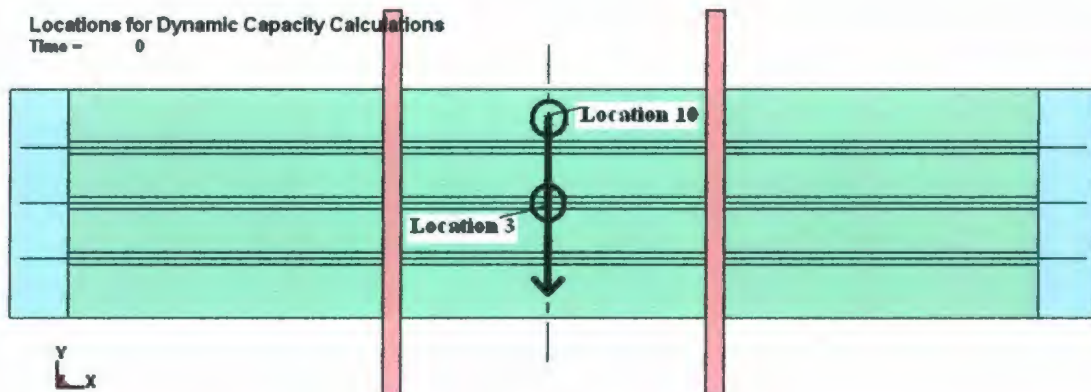


Figure 4-63: Load scenario 7: progressive damage between transverse stiffeners.

Results of the load cases simulated for this scenario are presented in the form of z-force reaction versus lateral displacement curves. As in other scenarios, the 5 and 10 cm load cases are not presented because of the excessive strain observed with the collision mechanism during the indenter-longitudinal stiffener encounters.

The load-displacement results for the 0.2, 0.5, and 2 cm load cases are given in Figure 4-64. The humps in these load-displacement curves correspond to indenter-longitudinal frame encounters.

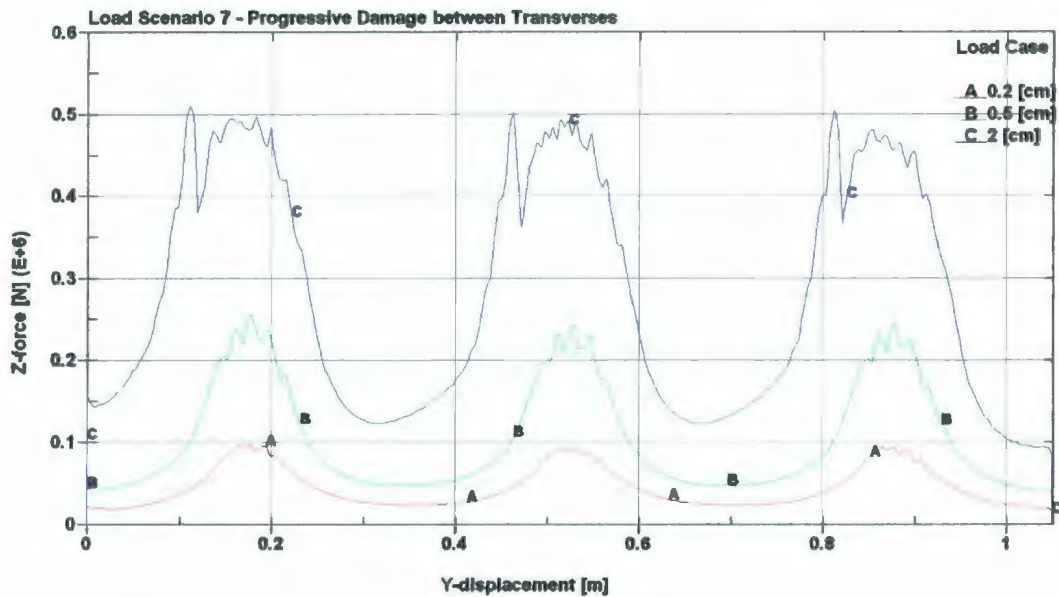


Figure 4-64: Load scenario 7: load-displacement curves for 0.2, 0.5, and 2 cm load cases.

The 0.2 cm load case exhibits a primarily elastic response to this progressive damage scenario. This assumption is based on three indicators: the load-displacement curve exhibits asymmetric hump-hollow pattern; the maximum plastic damage is less than 0.28% (plastic elongation) and is very limited in extent; and the start, end, and “hollow” load values (i.e. values corresponding with y-displacements of approximately 0.0, 0.35, 0.70, and 1.050 m) are all equal, indicating that the plastic damage is insignificant in these areas. No buckling of the longitudinal stiffener webs was observed.

The 0.5 cm appears to have a symmetric hump-hollow load curve, however the “hollow” values are not all equal, indicating that the plastic damage to the longitudinal stiffeners and the hull plating has a slight effect on the structural capacity at these locations. The

maximum plastic elongation for this load case is 3.73%, which is significantly higher than the 0.2 cm load case. Again, no longitudinal stiffener buckling was observed.

The 2 cm load case exhibits excessive plastic damage. The load curve is asymmetric, and the static and dynamic load capacities at locations 3 and 10 are very different. There is an initial drop in load, as observed in other load cases above, followed by a sharp rise in load as the indenter encounters the first longitudinal stiffener. This sharp rise develops into a hump (as with the other indenter-stiffener encounters described above), however as the hump crests, there is a drop in load followed by a sharp increase that returns the load to the same level. This drop is associated with a slight indenter-stiffener collision mechanism coupled with longitudinal stiffener web buckling. The hollow following this hump is not symmetric; it falls off more quickly on the left side than it rises on the right. This shows that the structure adjacent to the damaged longitudinal stiffener cannot support the same amount of load as the structure adjacent to the next longitudinal stiffener. Results of previous load scenarios suggest that this is because of prior plastic damage (i.e. to the first longitudinal stiffener). Each of the subsequent humps and hollows are simply a repetition of these mechanisms, with no new phenomena occurring. The maximum plastic elongation for this load case is just over 19%, indicating that the results are indeed realistic and not subject to the excessive strains associated with large indenter-stiffener collisions.

The structural mechanisms involved in this load scenario are similar to those of load scenario 3, with the addition of a slight collision mechanism coupled with longitudinal stiffener buckling.

Comparisons between static and dynamic structural capacities were made for locations 10 and 3 and are given in Table 4-4.

Table 4-4: Structural capacities for load scenario 7.

Location	3			10		
	Load Case	Static [kN]	Dynamic [kN]	% Decrease	Static [kN]	Dynamic [kN]
0.2	111	95	14.9%	20	20	0.0%
0.5	249	226	9.0%	45	39	14.2%
2	550	483	12.3%	159	83	47.7%

4.4.2 Load scenario 8: progressive damage along a transverse stiffener

This load scenario explores progressive damage along a transverse. The large grillage model is statically loaded at location 11 (shown in Figure 4-65), the indenter is then dragged 1.050 m in the transverse direction, to the point of unloading. Figure 4-65 depicts this scenario as well as the locations of the static and dynamic structural capacity comparisons (labelled “location 6” and “location 8”). This load scenario is unique from the others in that the start and finish locations of the indenter are not symmetric. This is because of the geometry of the cut-out in the transverse. Because of this asymmetry, no comparison between the static and dynamic structural capacities at location 11 will be made.

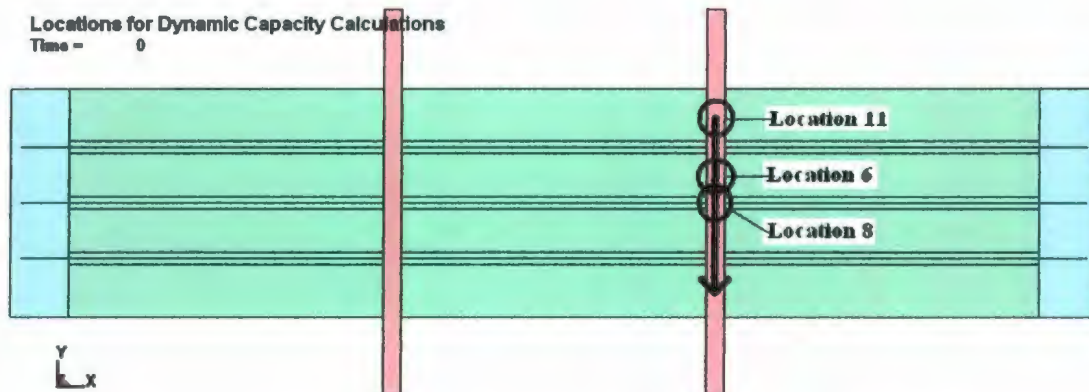


Figure 4-65: Load scenario 8: progressive damage along a transverse stiffener.

Results of the load cases simulated for this scenario are presented in the form of z-force reaction versus lateral displacement curves. As in other scenarios, the 5 and 10 cm load cases are not presented. This is because of the excessive strain observed with a collision mechanism similar to those described above. This collision mechanism occurred when the indenter encountered the opposite side of a cut-out in the transverse frame (as shown in Figure 4-66).

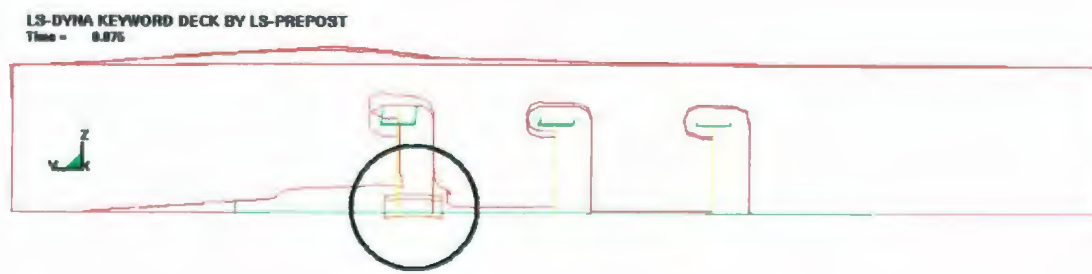


Figure 4-66: Load scenario 8: wireframe plot of indenter-cut-out collision: 5 cm load case.

The load-displacement results for the 0.2, 0.5, and 2 cm load cases are given in Figure 4-67. The hollows in these load-displacement curves correspond to indenter-“cut-out” encounters. As seen in this figure, the structural capacity at the cut-outs is significantly less than along the rest of the transverse stiffener.

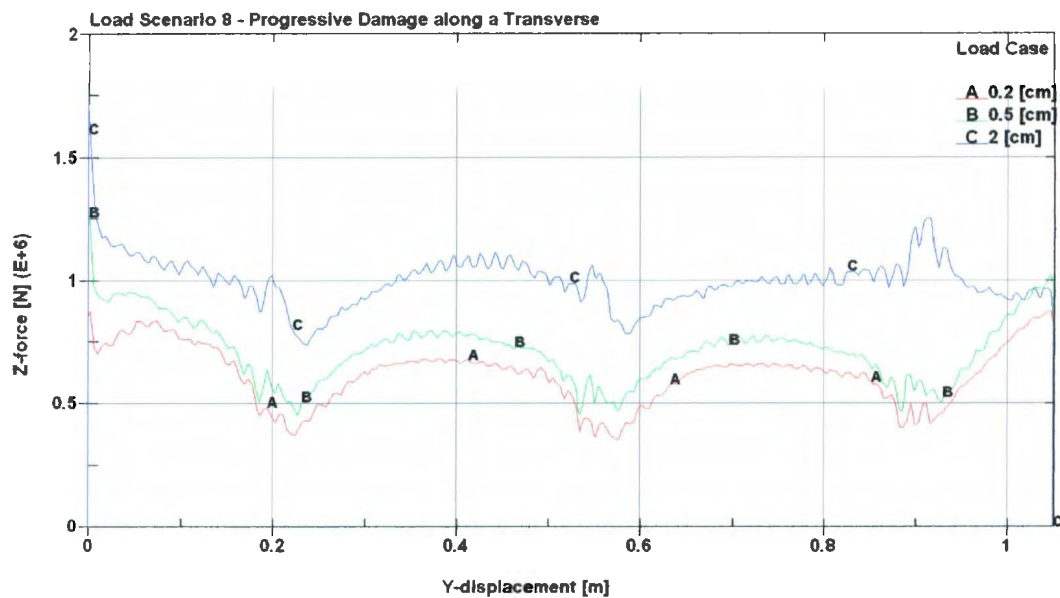


Figure 4-67: Load scenario 8: load-displacement curves for 0.2, 0.5, and 2 cm load cases.

It should be noted that all three of these load cases exhibited large magnitude plastic damage. The 0.2 cm load case showed a maximum plastic elongation of approximately 26.2%, which while confined to the transverse stiffener and the immediately adjacent structure, was significant in extent (see Figure 4-68). The 0.5 cm load case exhibited a 30.7% plastic elongation, and the 2 cm load case showed a 145.5% plastic elongation.

Because of the extreme magnitude of the plastic damage for the 2cm load case, it will not be discussed further, as it is obvious that the results are not realistic.

The plastic damage for this load scenario is significantly higher than for any of the other load scenarios. This is because of the relative stiffness of the transverse stiffener compared with the rest of the structure simulated. The transverse stiffeners are extremely stiff due to their thickness, length, height, and the fact that all other structure is tied to them. This extreme stiffness implies that even small displacement-loads induce large structural reaction loads.

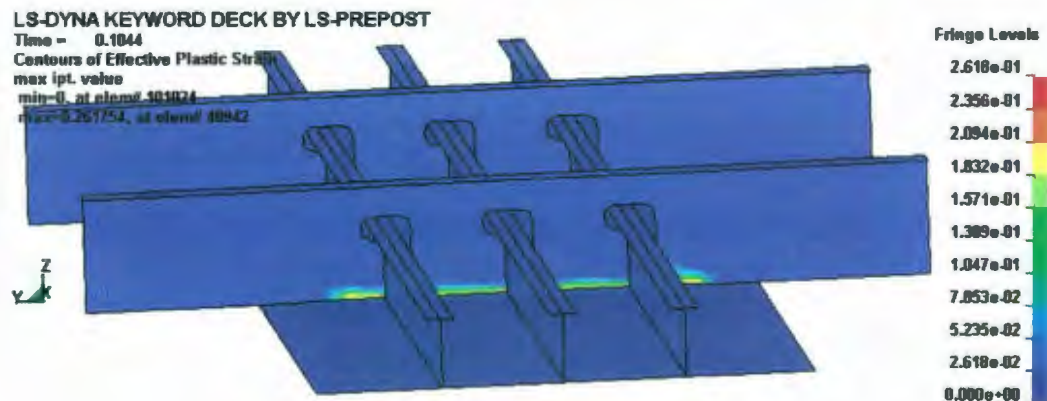


Figure 4-68: Load scenario 8: extent of plastic damage for the 0.2 cm load case.

The 0.2 and 0.5 cm load cases exhibit very similar load-displacement curves and will be discussed jointly. At the commencement of the dynamic load, there is a significant drop in structural capacity for both load cases. Hull plate bending, membrane stretching, and through-thickness shear are not significant for most of the structural response for these

load cases, as the levels of indentation are small. Their relative contributions to the overall structural reaction rise briefly at the points where the centre of the indenter is at the centre of a cut-out (i.e. the hollows in the load-displacement curves). This is because the indenter is contacting very little of transverse frame at this time.

The majority of the structural stiffness is provided by the transverse stiffener itself. It is thick compared with the other structural components (almost twice as thick as most of the other steel in the structure), and therefore is very stiff, and does not tend to share load with adjacent structure. The overall structural response is mostly provided by compression of the transverse stiffener's web, and slight bending of its flange. Figure 4-69 shows the normal force reaction of the transverse stiffener to the static (top) and dynamic (bottom) loads. The normal force distribution is relatively symmetric for the static load, but upon commencement of the dynamic load, the extent of distribution dramatically decreases. This is the cause of the initial drop in load observed at the start of the load-displacement curves for these cases. The load continues to drop towards the "hollow" because the indenter is nearing the cut-out. As the indenter moves away from the cut-out, the structural reaction increases in magnitude again. These phenomena repeat for the subsequent two cut-outs.

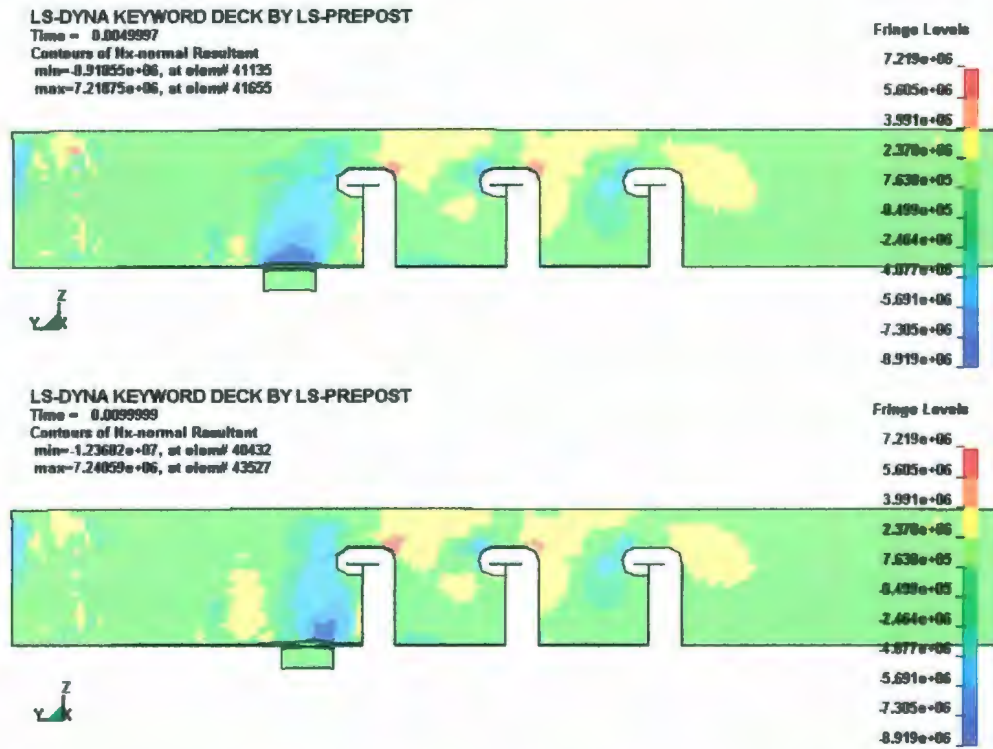


Figure 4-69: Load scenario 8: plot of normal force reaction to static load (top) and dynamic load (bottom).

Comparisons between static and dynamic structural capacities were made for locations 6 and 8, and are given in Table 4-5. Separate static simulations were conducted for these locations, and their load curves were given previously in Figure 4-48 and Figure 4-58 respectively.

Table 4-5: Structural capacities for load scenario 8.

Location	6			8		
	Load Case	Static [kN]	Dynamic [kN]	% Decrease	Static [kN]	Dynamic [kN]
0.2	500	675	-34.9%	428	529	-23.6%
0.5	762	779	-2.3%	748	599	19.9%

It is interesting to note that in all cases except one, there is a dynamic *increase* in structural capacity associated with progressive damage along a transverse stiffener. The one exception is the 0.5 cm load case at location 8 (i.e. at the transverse centre of the transverse stiffener). At location 6 (i.e. between two longitudinal stiffeners), the dynamic capacity is greater than the static capacity in both cases. These results are unexpected and are contrary to the findings from all other load scenarios. Observation of Figure 4-67 shows that all load-displacement curves exhibit an oscillation throughout their entirety. Investigation of their load time-histories reveal that this oscillation occurs at approximately 625 Hz; which is well outside the range of damping employed in this numerical model (i.e. 120-150 Hz from chapter 3.9). Further, this behaviour was not present at this magnitude or duration for any of the other simulations presented in this thesis. This type of behaviour was, however, observed in some of the 5 and 10 cm load cases that were omitted in other load cases. Further simulations are required to determine if the results of this load scenario are valid.

4.5 Summary of Progressive Damage Load Scenario Results

A table showing the change in structural capacity based on location and load scenario is given in Table 4-6. For brevity, any load cases that have equivalent static and dynamic structural capacities (e.g. for the 0.2 cm load case), or are not realistic (e.g. the 10 cm load cases and some of the 5 cm load cases), are excluded from the table. Following this table is a brief discussion of each load scenario.

Table 4-6: Dynamic decrease in structural capacity results.

Location		1	2	3	4	5	6	7	8	9	10
Load Scenario	Load Case										
1	0.5	9.0%	-	-	-	-	-	-	-	-	-
	2	28.0%	-	-	-	-	-	-	-	-	-
	5	60.0%	-	-	-	-	-	-	-	-	-
2	0.5	-	10.5%	6.5%	-	-	-	-	-	-	-
	2	-	37.0%	13.5%	-	-	-	-	-	-	-
	5	-	60.0%	57.0%	-	-	-	-	-	-	-
3	0.2	-	-	17.0%	0.0%	-	-	-	-	-	-
	0.5	-	-	7.5%	9.0%	-	-	-	-	-	-
	2	-	-	14.5%	33.5%	-	-	-	-	-	-
	5	-	-	40.5%	28.5%	-	-	-	-	-	-
4	0.2	20.0%	-	-	-	0.0%	-27.0%	-	-	-	-
	0.5	22.0%	-	-	-	11.0%	4.0%	-	-	-	-
	2	42.0%	-	-	-	30.0%	38.0%	-	-	-	-
5	0.2	-	39.5%	28.8%	-	-	-	13.1%	-31.1%	-	-
	0.5	-	35.0%	26.5%	-	-	-	13.4%	7.0%	-	-
	2	-	30.6%	20.5%	-	-	-	42.0%	12.1%	-	-
6	0.2	-	-	35.1%	-	-	-	-	-	24.1%	-
	0.5	-	-	27.2%	-	-	-	-	-	25.6%	-
	2	-	-	21.1%	-	-	-	-	-	42.7%	-
7	0.2	-	-	14.9%	-	-	-	-	-	-	0.0%
	0.5	-	-	9.0%	-	-	-	-	-	-	14.2%
	2	-	-	12.3%	-	-	-	-	-	-	47.7%
8	0.2	-	-	-	-	-	-34.9%	-	-23.6%	-	-
	0.5	-	-	-	-	-	-2.3%	-	19.9%	-	-

Load scenario 1 explored progressive damage between longitudinal stiffeners without directly loading the transverse frames. A decrease between static and dynamic structural capacities was observed for this load scenario. Investigation into the structural mechanisms causing the dynamic decrease in structural capacity revealed that the membrane and bending reactions of the plate were significant. It was determined that progressive plastic damage caused asymmetric bending around the indenter during the dynamic load. As well, it extended the membrane stress field to include two areas of

high-stress concentration near the “behind” corners of the indenter, which carried very little through-plane shear force. Overall, the level of dynamic structural decrease in capacity increased with each load case.

Load scenario 2 explored progressive damage between transverse frames and along the central longitudinal stiffener. A decrease between static and dynamic structural capacities was observed for this load scenario. The structural mechanisms involved in the decreased dynamic structural capacity were stiffener buckling, plate bending, and membrane stretching. It was observed that the longitudinal stiffeners buckled under the dynamic load for the 2 and 5 cm load cases, but similar buckling under a static load was not observed until an indentation of at least 7 cm occurred. Further, the magnitude of the asymmetric plate bending reaction increased as stiffener buckling increased – as did membrane stretching. For the 2 cm load case, areas of high-stress concentration similar to those observed in load scenario 1 appeared when the stiffener buckling became large. These highly-stressed areas were present during the entire dynamic load for the 5 cm load case. Overall, the level of dynamic structural decrease in capacity increased with each load case.

Load scenario 3 explored progressive damage between transverse frames and diagonally across the longitudinal stiffeners. The load-displacement curves exhibited humps that corresponded to the indenter encountering the longitudinal stiffeners during its lateral motion. A decrease between static and dynamic structural capacities was observed for this load scenario. Investigation into the cause of the decrease revealed an alternating

combination of the mechanisms identified in load scenarios 1 and 2, as the indenter passed from “between longitudinals” to “on longitudinal” locations, respectively. In addition, it was observed that hull plating failure was probable for the 5 cm load case. This hull plate failure would result in collision between the indenter and the longitudinal stiffeners upon continued loading. As in load scenario 2, longitudinal stiffener buckling occurred for the 2 and 5 cm load cases. Based on the large grillage experiments, stiffener buckling would not occur under these loading conditions if the loads were statically applied. Overall, the level of dynamic structural decrease in capacity increased with each load case.

Load scenario 4 is an extension of load scenario 1 to include direct loading of the transverse stiffeners. A collision mechanism was observed for the indenter-transverse stiffener encounters for the 5 and 10 cm load cases. A decrease between static and dynamic structural capacities was observed for this load scenario. Structural mechanisms similar to load scenario were present, with the addition of transverse stiffener buckling. As with other load scenarios, the transverse stiffener buckled at a dynamic load that was lower than that required to buckle the stiffener statically. Further, the plastic damage to the transverse stiffeners caused a further decrease in structural capacity to the adjacent structure – even for the 0.2 and 0.5 cm load cases. Overall, the level of dynamic structural decrease in capacity increased with each load case. A dynamic *increase* in structural capacity was observed for the 0.2 cm load case at location 6. It is suspected that this is not a legitimate increase, but is, instead, an artefact of an inertial effect associated with the loading method.

Load scenario 5 is an extension of load scenario 2 to include direct loading of the transverse stiffeners. A collision mechanism was observed for the indenter-transverse stiffener encounters for the 5 and 10 cm load cases. A decrease between static and dynamic structural capacities was observed for this load scenario. Structural mechanisms similar to load scenario 2 are present, with the addition of transverse stiffener buckling. Again, the transverse stiffener buckled at a dynamic load that was lower than that required to buckle the stiffener statically. The transverse stiffener buckling was affected by a “cut-out” that allows the longitudinal stiffener to pass through the transverse stiffener. Despite the presence of this cut-out, the dynamic structural capacity of the transverse stiffeners is approximately equal to that of load scenario 4 (i.e. without the cut-out). As with load scenario 4, plastic damage to the transverse stiffeners caused a further decrease in structural capacity to the adjacent structure. Overall, the level of dynamic structural decrease in capacity increased with each load case for locations 7 and 8, and decreased for locations 2 and 3.

Load scenario 6 is an extension of load scenario 3 to include direct loading of the transverse stiffeners. A decrease between static and dynamic structural capacities was observed for this load scenario. Structural mechanisms are similar to load scenario 3, with the addition of a collision mechanism for both the longitudinal and transverse stiffeners for the 5 and 10 cm load cases. Similar to load scenario 5, the longitudinal stiffeners buckle as the indenter nears the transverse frame (for the 2 cm load case). Like load scenario 5, the indenter encounters the first transverse frame at a cut-out, but this time the contact is concentrated on the side that is not supported by a longitudinal

stiffener. The dynamic structural capacity of the transverse frame, however, is still approximately equivalent in magnitude to load scenarios 4 and 5. The second indenter-transverse frame encounter occurs between cut-outs. The initial structural reaction is larger, but the overall (i.e. buckled) load is equivalent to the first encounter. Both transverse stiffeners buckle for the 2 cm load case. Again, plastic damage to the transverse stiffeners reduces the structural capacity of their adjacent structure. Overall, the level of dynamic structural decrease in capacity increased with each load case for location 9, and decreased for location 3.

Load scenario 7 explores progressive damage between transverse stiffeners at the longitudinal centre of the structure. Again, the 5 and 10 cm load cases are omitted due to excessive strain from the collision mechanism between the indenter and the longitudinal stiffeners. A decrease between static and dynamic structural capacities was observed for this load scenario. The structural mechanisms involved in the decreased dynamic structural capacity are similar to load scenario 3. In addition, slight indenter-longitudinal stiffener collision was observed, coupled with longitudinal stiffener web buckling for the 2 cm load case. Further plastic damage to a longitudinal stiffener decreased the structural capacity of the adjacent structure. Overall, the level of dynamic structural decrease in capacity increased with each load case for location 10, and remained about constant for location 3.

Load scenario 8 explores progressive damage along a transverse. Results from this load scenario are in question because they are contradictory to results from all other load

scenarios; that is, progressive damage generally causes a dynamic *increase* in structural capacity for the longitudinal stiffeners. Collision mechanisms were observed for the 5 and 10 cm load cases. Further excessive plastic deformation was observed for the 2, 5, and 10 cm load cases. The 0.2 and 0.5 cm load cases were also highly plastically deformed.

5 CONCLUSIONS AND RECOMMENDATIONS

5.1 Conclusions

From results of the load scenarios presented in Chapter 4, it is evident that there is a general decrease in the structural capacity of the “IACS polar class” large grillage structure to carry progressive ice loads, versus static ice loads. The level of decrease in structural capacity depends on the level of indentation into the structure, the location of the progressive damage, and the extent of the progressive damage. The structural mechanisms associated with this decrease arise from the transition from a static to a dynamic load (i.e. an impact to a scoring/raking load). Static loads were shown to create a symmetric response throughout the structure adjacent to the load (where permitted by the geometry of the structure). Upon commencement of the dynamic load, this symmetry vanished. The magnitude of the bending moment, membrane stress, and through-thickness shear reactions were all generally smaller on the trailing side of the progressive load. Further, previous plastic damage to large structural members (such as the transverse frames) was shown to have a definite weakening effect on the capacity of the structure adjacent to them.

In conclusion, it was determined that an “IACS polar class” ship structure demonstrates a decreased structural capacity to withstand progressive damage ice loads, as compared to static ice loads.

5.2 Recommendations

Several questions arose during this research that prompt further research. Some arise directly from problems encountered during this research, and others are recommendations for extending this research.

During the creation of the numerical model, it was desired to incorporate element/material failure. This would have enabled simulation of the hull plate fracture that occurred during the large grillage experiments (Chapter 2); as well, it would have enabled the inclusion of the 5 and 10 cm load cases that were generally omitted above – because failed structure would react more realistically than over-stretched structure. Element/material failure was incorporated into this numerical model for a time, and the failure associated with the large grillage experiments was modeled accurately. However, it was found that there is a relationship between mesh density and element failure-strain. That is, the denser the mesh, the larger the elemental strain for a given load. For example, a low density mesh may predict structural (i.e. element/material) failure accurately with a 25% failure-strain, while a high density mesh might produce similar results with a 45% failure-strain. Because the relationship between failure-strain and mesh density was not fully understood, element/material failure was removed from the numerical model. It is recommended that this relationship be studied in detail, and that element/material failure be incorporated in all future numerical simulations. Further, the 5 and 10 cm load cases that were omitted above should be solved including element/material failure.

The second recommendation is that the results of load scenario 8 be investigated. This load scenario predicted an *increase* in structural capacity for a progressive load along a transverse stiffener. These results are contrary to the findings of the other seven load scenarios.

Another recommendation is that an attempt be made to ascertain the reason why the elastic reaction for the numerical model was larger than the experimental elastic response. Much effort was put into testing various inputs for the numerical model in order to obtain better agreement for the low displacement-load levels. All attempts were only marginally successful, and served to undermine the accuracy of the predictions at the higher displacement-load levels. It is recommended that further investigation into both the numerical model and the large grillage experimental data be made.

The next two recommendations are regarding the method used to load the numerical large grillage structure. The first is regarding the indenter model, and the second is regarding the method of loading the large grillage numerical model (i.e. the motion of the indenter). The response of the ship's structure is of primary importance for this research. For this reason, the indenter used to cause the progressive damage to the structure was modeled as a rigid body, while the structure was modeled as a deformable body. In a real world scenario, an indenter composed of sea ice or glacial ice would react very differently, and load release mechanisms (i.e. failure mechanisms) within the ice would relieve some of the load imposed on the ship structure. It is recommended that the indenter be numerically modeled as a deformable body of ice, and that these simulations be solved

again. The second recommendation is that a more realistic method of loading be employed. An objective of this thesis was to identify the structural reactions associated with progressive damage due to ice. This was partially accomplished by completely separating the indentation and the scoring (i.e. lateral) motions of the indenter. This loading situation would rarely occur in practice with real ship-ice interactions. Instead, some combination of indentation and scoring would occur simultaneously. It is recommended that a new, more realistic method of loading incorporating some combination of simultaneous indentation and scoring be employed, and the numerical simulations be solved again.

Finally, it is recommended that this research be extended, and that a relationship between progressive damage indentation level, location, and extent of damage be developed. This relationship could then predict the dynamic decrease in structural capacity associated with a given progressive load. It is then recommended that the effect of this relationship on the design scenario for the IACS polar rules be investigated.

6 REFERENCES

- Abraham, J. 2008. Plastic response of ship structure subjected to ice loading. M. Eng., Memorial University of Newfoundland.
- ANSYS Inc. 2007a. ANSYS LS-DYNA user's guide. In Release 11.0 documentation for ANSYS. Version 11.0 ed. USA: ANSYS Inc.
- _____. 2007b. Release 11.0 documentation for ANSYS. Vol. Version 11.0. USA: ANSYS Inc.
- Belytschko, T., W-K Liu, and B. Moran. 2000. Nonlinear finite elements for continua and structures. Chichester, England: John Wiley & Sons, Ltd.
- Brown, A. J. 2002a. Collision scenarios and probabilistic collision damage. *Marine Structures* 15, (4) (July): 335–364.
- _____. 2002b. Modeling structural damage in ship collisions. Washington, D.C.: Ship Structure Committee, SSC - 1400 Draft Report.
- Daley, C. G. 2001. Oblique ice collision loads on ships based on energy methods. *Oceanic Engineering International* 5, (2).
- Daley, C. G., and G. Hermanski. 2008a. Ship frame research program - an experimental study of ship frames and grillages subjected to patch loads, volume 2 - theory and analysis reports. Ship Structure Committee, SSC Project SR 1442 - Final Report; OERC Report 2008-001; NRC-IOT Report TR-2008-11.
- _____. 2008b. Ship frame research program - an experimental study of ship frames and grillages subjected to patch loads, volume 1 - data report. Ship Structure Committee, SSC Project SR 1442 - Final Report; OERC Report 2008-001; NRC-IOT Report TR-2008-11.
- Dixon, K. 2007. Arctic sea ice changes in GFDL climate change scenario experiment. *GFDL Climate Modeling Research Highlights* 1, (1) (02-02).

- European Space Agency. Satellites witness lowest arctic ice coverage in history. In European Space Agency [database online]. Paris, 2007 [cited November 4 2008]. Available from http://www.esa.int/esaCP/SEMYTC13J6F_index_2.html (accessed November 4, 2008).
- FMA-SMA. 2008. The structural design and engine output required of ships for navigation in ice - "Finnish-Swedish ice class rules". Finland-Sweden: Finnish Maritime Administration - Swedish Maritime Administration.
- Hallquist, J. O. 2006. LS-DYNA theory manual. Livermore, California: Livermore Software Technology Corporation, http://www.lstc.com/pdf/ls-dyna_theory_manual_2006.pdf (accessed September 9, 2008).
- _____. 1978. A numerical treatment of sliding interfaces and impact. In Computational techniques for interface problems., eds. K. C. Park, D. K. Gartling. Vol. 30, 117-133. New York: ASME-AMD.
- _____. 1976. A procedure for the solution of finite deformation contact-impact problems by the finite element method. University of California: Lawrence Livermore National Laboratory, UCRL-52066.
- Hill, R. 1962. Acceleration waves in solids. Journal of the Mechanics and Physics of Solids 10, (1) (January-March 1962): 1-16.
- Hughes, O. 1988. Ship structural design: A rationally-based, computer-aided, optimization approach. New Jersey, NY: The Society of Naval Architects and Marine Engineers.
- IACS. 2007. Requirements concerning polar class. London: International Association of Classification Societies.
- _____. 2006. UR I 1, 2 and 3. London: International Association of Classification Societies, .
- Imaoka, S. Implicit vs. explicit dynamics. in ansys.net [database online]. 2001 [cited 12/3 2008]. Available from http://ansys.net/?mycat=tnt_sheldon13 (accessed December 3, 2008).

- IMO. 2002. Guidelines for ships operating in arctic ice-covered water. London: International Maritime Organization, MSC/Circ.1056, MEPC/Circ.399.
- Jones, Norman, and Tomasz Wierzbicki. 1983. Structural crashworthiness. London; Boston: Butterworths.
- Kitamura, O. 2002. FEM approach to the simulation of collision and grounding damage. *Marine Structures* 15, .
- _____. 1997. Comparative study on collision resistance of side structure. *Marine Technology* 34, (4) (October): 293-308.
- Kozarski, N. 2005. Importance of strain hardening in plastic response of rectangular beams subjected to bending loads. M. Eng., Memorial University of Newfoundland.
- LSTC. 2007a. LS-dyna keyword user's manual. Vol. I. Livermore, California: Livermore Software Technology Corporation.
- _____. 2007b. LS-dyna keyword user's manual. Vol. II. Livermore, California: Livermore Software Technology Corporation.
- Olovsson, L., K. Simonsson, and M. Unoosson. 2006. Shear locking reduction in eight-noded tri-linear solid finite elements. *Computers & Structures* 84, (7) (February).
- Paik, J. K. 2007a. Practical techniques for finite element modeling to simulate structural crashworthiness in ship collisions and grounding (part I: Theory). *Ship and Offshore Structures* 2, (1): 69.
- _____. 2007b. Practical techniques for finite element modelling to simulate structural crashworthiness in ship collisions and grounding (part II: Verification). *Ship and Offshore Structures* 2, (1): 81.
- Paik, J. K., J. Amdahl, N. Barltrop, E. R. Donner, Y. Gu, H. Ito, H. Ludolphy, P. T. Pedersen, U. Rohr, and G. Wang. 2003. Committee V.3: Collision and grounding. Paper presented at 15th International Ship and Offshore Structures Congress (ISSC), San Diego, USA.
- Paik, J. K., and T. K. Lee. 1995. Damage and residual strength of double-hull tankers in grounding. *International Journal of Offshore and Polar Engineering* 5, (4) (December).

- Paik, J. K., and P. T. Pedersen. 1996. Modelling of the internal mechanics in ship collisions. *Ocean Engineering* 23, (2): 107.
- Paik, J. K., and A. K. Thayamballi. 2003. Ultimate limit state design of steel-plated structures. West Sussex, England: John Wiley & Sons, Ltd.
- Pedersen, P. T. 1995. Collision and grounding mechanics. Paper presented at Proceedings of the West European Confederation of Maritime Technology Societies (WEMT) Vol. 1, Copenhagen.
- Pedersen, P. T., and S. Zhang. 2000. Effect of ship structure and size on grounding and collision damage distributions. *Ocean Engineering* 27, : 1161.
- Revkin, A. C. 2007. Arctic melt unnerves the experts. *New York Times*, October 2, 2007, sec Science: Environment.
- Sajdak, J. A. W., and A. J. Brown. 2004. Modeling longitudinal damage in ship collisions. Washington, D.C.: Ship Structure Committee, SR-1426.
- Servis, D. P., and M. Samuelides. 1999. Ship collision analysis using finite elements. Paper presented at Safer EuRORO, Spring Meeting, Nantes.
- Simonsen, B. C. 1997a. Ship grounding on rock - I. theory. *Marine Structures* 10, : 519.
- _____. 1997b. Ship grounding on rock - II. validation and application. *Marine Structures* 10, : 563.
- Simonsen, B. C., and P. F. Hansen. 2000. Theoretical and statistical analysis of ship grounding accidents. *Transactions of the American Society of Mechanical Engineers* 122, (August): 200.
- Transport Canada. 1998. User assistance package for the implementation of Canada's arctic ice regime shipping system (AIRSS). Ottawa: Transport Canada, TP 12819.
- Wang, G., C. Ji, P. Kujala, S. -Gab Lee, A. Marino, J. Sirkar, K. Suzuki, P. T. Pedersen, A. W. Vredeveldt, and V. Yuryi. 2006. Committee V.I: Collision and grounding. Paper presented at 16th International Ship and Offshore Structures Congress (ISSC), Southampton, U.K.

Wang, G., J. Spencer, and Y. Chen. 2002. Assessment of a ship's performance in accidents. *Marine Structures* 15, (4-5) (July-October): 313-333.

WMO/IOC. 2004. JCOMM expert team on sea ice (ETSI), second session, steering group for the global digital sea ice data bank (GDSIDB), tenth session. Hamburg: World Meteorological Organization & Intergovernmental Oceanographic Commission (of UNESCO). JCOMM Meeting Report No. 28, <http://www.wmo.int/pages/prog/amp/mmop/documents/Jcomm-MR/JCOMM-MR-28-SI-2/JCOMM-MR-28-si2-gdsidb10.doc>.

Zhang, S. 2002. Plate tearing and bottom damage in ship grounding. *Marine Structures* 15, (2) (March).

APPENDICES

APPENDIX A: BEOWULF CLUSTER SPECIFICATIONS

The Beowulf clusters used in this research have specifications as follows:

Cluster 1		Cluster 2	
Master Node Info		Master Node Info	
Name:	nereid64	Name:	nereid65
# processors:	2	# processors:	2
Processor type:	AMD Opteron 246	Processor type:	AMD Opteron 246
# cores per processor:	1	# cores per processor:	1
Processor Speed:	2.0 GHz	Processor Speed:	2.0 GHz
L2 cache:	1024 KB	L2 cache:	1024 KB
RAM:	12 GB	RAM:	16 GB
Storage:	800 GB	Storage:	800 GB
Slave Node Info		Slave Node Info	
# of slave nodes:	14	# of slave nodes:	14
All nodes homogeneous?	Yes	All nodes homogeneous?	No*
Processor type:	AMD Opteron 246	Specs for slave nodes 0-8	
RAM:	6 GB (each)	Processor type:	AMD Opteron 246
Network:	1 Gbit LAN	RAM:	6 GB (each)
Cluster Software Environment		Network:	
OS:	Redhat Linux Enterprise 3	Specs for slave nodes 9-13	
LAM/MPI:	Version 6.5.9	Processor type:	AMD Opteron 248
		# cores per processor:	1
		Processor Speed:	2.2 GHz
		L2 cache:	1024 KB
		RAM:	6 GB (each)
		Network:	1 Gbit LAN
Cluster Software Environment		OS:	
		OS:	Redhat Linux Enterprise 3
		LAM/MPI:	Version 6.5.9

APPENDIX B: LARGE GRILLAGE DATA COLLECTION EQUIPMENT AND SPECIFICATIONS

Hardware:

- (A) NI SCXI 1521 B 120 Ohm Quarter-Bridge Strain Gage Input Module:**
 - Measurement of Strains
 - 24 Analog Input Channels
 - Programmable Excitation (0 V to 5 V) per channel
 - Low-pass filter (10 Hz) per channel
 - 120 Ohm $\frac{1}{4}$ bridge completion resistor per channel
 - Used in conjunction with the SCXI-1317 terminal block
 - Max Voltage -11 to +11 V
- (B) NI SCXI 1102C 32 Channel Amplifier module, 10 KHz Bandwidth:**
 - 32 analog input channels
 - 333 KS/s maximum sampling rate
 - NI-DAQmx Measurement Services software to simplify configuration & measurement
 - Max Voltage -42 to +42 V
 - 2 Hz Low-pass filtering channel
 - Programmable Gain settings
- (C) SCXI-1000 Chassis:**
 - Low-noise SCXI Chassis
 - Power SCXI modules
 - Controls SCXI modules and conditioned signals
 - Architecture includes SCXI bus, which routes analog and digital signals and act as the communication conduit between modules
 - Chassis control circuitry manages this bus, synchronizing the timing between each module and the DAQ device. With this architecture, you can input channels from several modules in several chassis at rates up to 333 KS/s for every DAQ device
 - The NI SCXI is a 4-slot chassis available with a number of standard AC power options. It is ideal for single-chassis or low-channel-count applications. If the application grows, we can daisy-chain two or more SCXI-1000 chassis



(D) SCXI-1300 (Front Mounting):

- SCXI 1300 is used to connect input signals to 1102C
- General purpose terminal block with an onboard temperature sensor for cold-junction compensation
- Recommended for general purpose voltage applications
- Mount to the front of SCXI module

(E) SCXI-1317 (Front Mounting):

- Front-Mounting Terminal Block for SCXI -1521 and SCXI 1521B Quarter Bridge Strain Gage Modules
- Auto-detectable through software
- Shielded for accurate signal connections
- Screw terminal connectivity
- 24-Channel terminal block provides three terminals for each quarter-bridge strain gage channel, comprised of excitation +, analog and quarter-bridge

(F) NI 6220:

- This is the DAQ (Date Acquisition Card) in use
- Installed within the CPU
- NI PCI-6220 16-Bit, 250 KS/s, 16Analog Inputs
- 24 digital input/output, 32 bit counters; digital triggering
- NI-MCal calibration technology for increased measurement accuracy

- Includes NI-DAQmx, VI Logger Lite data-logging software, and other measurement services
- Correlated DIO (8 clocked lines, 1 Mhz)
- NIST- traceable calibration certificate and more than 70 signal conditioning options
- Select higher-speed M Series for 5X faster sampling rates or high accuracy M Series for 4X resolution

APPENDIX C: MATERIAL INSTABILITY TEST

Material Formulation:	Mat_24
	Density: 7850 kg/m ³
	Young's modulus: 200 GPa
	Poisson's ratio: 0.3
	Stress-strain curve: see Figure C-0-1
	Strain-rate effects: none
Boundary Conditions:	Pinned edges
Load:	Impulse Load of 1 kPa over 2 ms on shell element "S 12" (see Figure C-0-2)
Shell Parameters:	
Element formulation:	Belytschko-Tsay (default)
SHRF:	5/6 (recommended)
Integration rule:	Gaussian Quadrature
NIPS:	5 (recommended)
Shell thickness:	5 mm
Damping:	none
Results:	Infinite rebound displacement (see Figure C-0-3 and Figure C-0-4) with infinite shell element growth in all directions

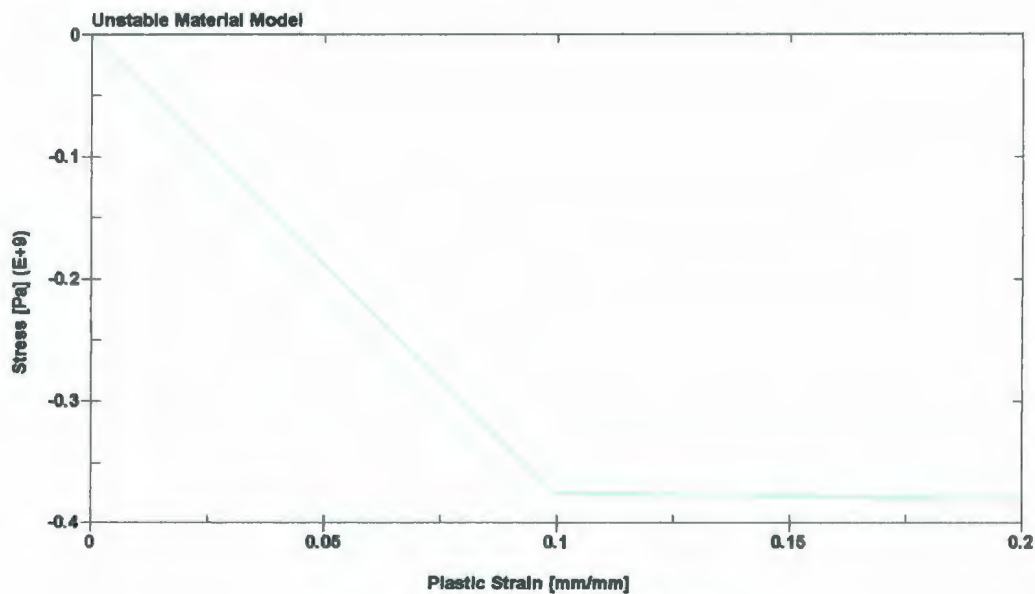


Figure C-0-1: Unstable Material Model.

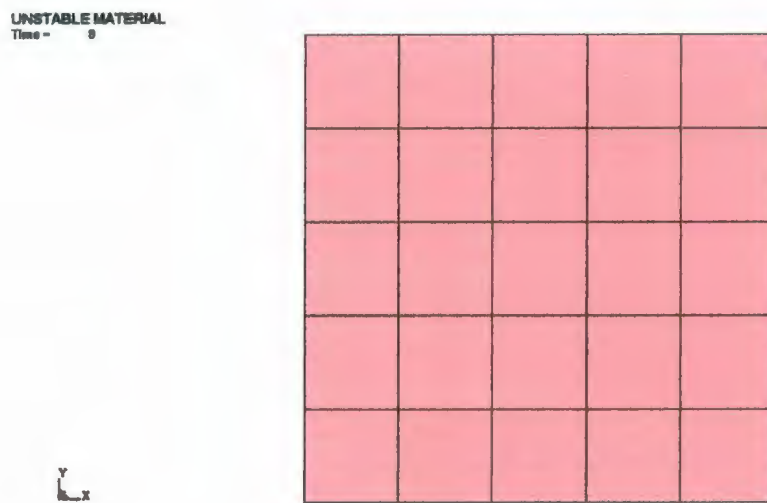


Figure C-0-2: Mesh showing loaded shell element.

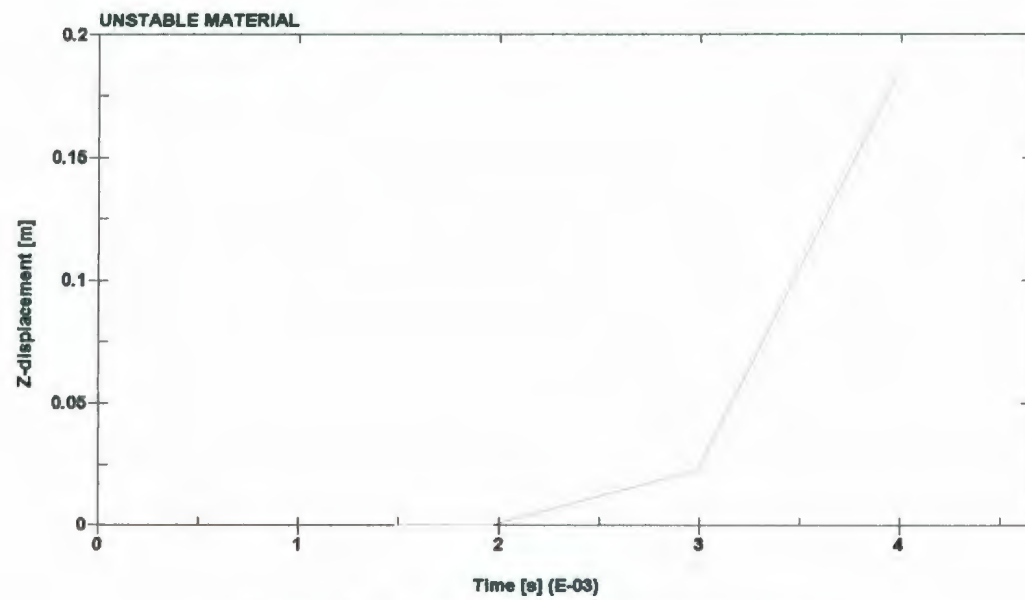


Figure C-0-3: Near centre nodal displacement plot.

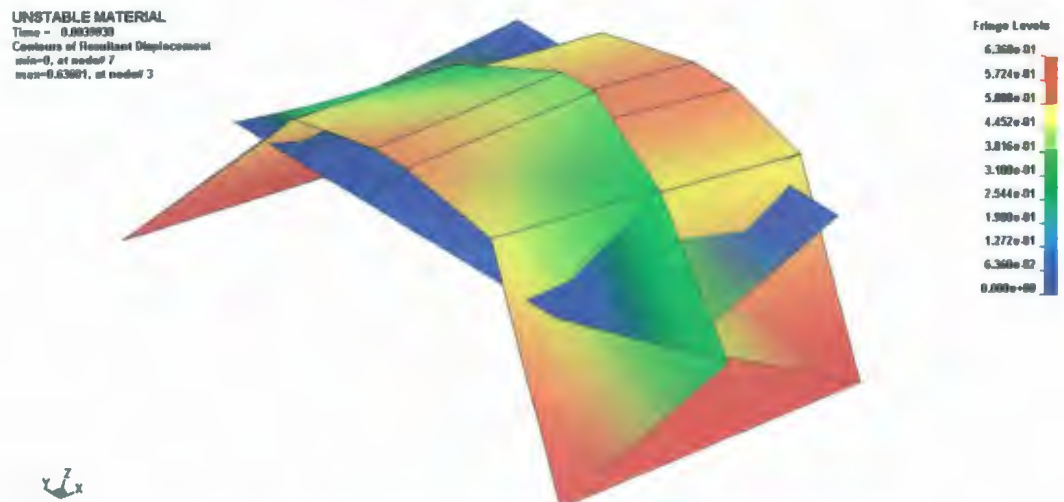


Figure C-0-4: Shell rebound deformation just before infinite expansion.



